

DEPARTMENT OF PHYSICS, UNIVERSITY OF JYVÄSKYLÄ

**JET TRANSVERSE MOMENTUM DISTRIBUTIONS
MEASURED BY ALICE**

**BY
TOMAS SNELLMAN**

PHD thesis

Supervisors: Jan Rak, Dong Jo Kim

Jyväskylä, Finland
December, 2018

3 Contents

| | | | |
|----------|----------|---|-----------|
| 4 | 1 | Introduction | 7 |
| 5 | 1.1 | Quantum chromodynamics | 8 |
| 6 | 1.1.1 | Foundation of QCD | 8 |
| 7 | 1.1.2 | Asymptotic Freedom | 9 |
| 8 | 1.2 | Heavy ion physics | 13 |
| 9 | 1.2.1 | History | 13 |
| 10 | 1.3 | Features of Heavy-Ion Collisions | 15 |
| 11 | 1.3.1 | Collision Geometry | 15 |
| 12 | 1.3.2 | Nuclear Geometry | 16 |
| 13 | 1.3.3 | Hydrodynamical Modelling | 19 |
| 14 | 1.4 | Flow | 22 |
| 15 | 1.4.1 | Anisotropic Flow | 23 |
| 16 | 1.4.2 | High p_T Phenomena | 24 |
| 17 | 1.5 | Hard processes | 25 |
| 18 | 1.5.1 | pQCD factorization | 25 |
| 19 | 1.5.2 | Jet hadronisation | 27 |
| 20 | 1.5.3 | Jet energy loss | 31 |
| 21 | 1.5.4 | New paradigm of jet Quenching | 36 |
| 22 | 1.6 | QGP in Small systems | 38 |
| 23 | 1.6.1 | Collective phenomena | 38 |
| 24 | 1.6.2 | Absence of jet quenching | 39 |
| 25 | 1.6.3 | Centrality determination in small systems | 40 |
| 26 | 2 | Experimental Details | 48 |
| 27 | 2.1 | CERN | 48 |
| 28 | 2.2 | Large Hadron Collider | 48 |
| 29 | 2.2.1 | LHC experiments | 50 |
| 30 | 2.3 | ALICE | 51 |
| 31 | 2.3.1 | Tracking | 52 |
| 32 | 2.3.2 | TPC | 53 |
| 33 | 2.3.3 | TPC upgrade | 54 |
| 34 | 2.3.4 | Optical scanning | 56 |
| 35 | 2.3.5 | Particle identification | 58 |
| 36 | 2.3.6 | Electromagnetic Calorimeter | 59 |
| 37 | 2.3.7 | Forward detectors | 59 |

| | | |
|----|--|-----------|
| 38 | 2.3.8 Muon spectrometer | 61 |
| 39 | 2.3.9 Trigger | 61 |
| 40 | 3 Event and track selection | 63 |
| 41 | 3.1 statistics | 64 |
| 42 | 4 Analysis method | 65 |
| 43 | 4.1 Jet Finding | 65 |
| 44 | 4.1.1 Anti k_T algorithm | 65 |
| 45 | 4.2 j_T | 66 |
| 46 | 4.3 Unfolding | 68 |
| 47 | 4.3.1 Bayesian unfolding | 68 |
| 48 | 4.3.2 Toy Monte Carlo | 70 |
| 49 | 4.3.3 Pythia Response matrices | 71 |
| 50 | 4.3.4 Unfolding algorithm | 72 |
| 51 | 4.3.5 Unfolding closure test | 72 |
| 52 | 4.4 Background | 73 |
| 53 | 4.4.1 Perpendicular cone background | 74 |
| 54 | 4.4.2 Random background | 74 |
| 55 | 4.4.3 Auto-correlations | 77 |
| 56 | 4.4.4 Background methods | 77 |
| 57 | 4.5 Fitting | 78 |
| 58 | 5 Systematic errors | 80 |
| 59 | 5.1 Background | 80 |
| 60 | 5.2 Unfolding | 82 |
| 61 | 5.2.1 Effect of number of iterations | 82 |
| 62 | 5.2.2 Effect of different prior | 82 |
| 63 | 5.2.3 Effect of p_T truncation | 84 |
| 64 | 5.3 Tracking | 84 |
| 65 | 5.4 EMCAL | 84 |
| 66 | 5.5 Summary | 85 |
| 67 | 5.6 Comparison between A and C side | 86 |
| 68 | 5.7 Subtracted signal | 86 |
| 69 | 5.8 Combining systematics | 86 |
| 70 | 6 Results | 89 |
| 71 | 6.1 Fitting | 89 |
| 72 | 6.1.1 RMS values from fitted distributions | 89 |
| 73 | 6.2 High multiplicity | 89 |

| | | | |
|---------------|----------|---|-----------|
| ⁷⁴ | 7 | Discussion | 92 |
| ⁷⁵ | 7.1 | Dihadron j_T | 92 |
| ⁷⁶ | 7.2 | Comparing to dihadron and jet j_T results | 93 |
| ⁷⁷ | 7.2.1 | Different R parameters | 94 |
| ⁷⁸ | 7.2.2 | Leading tracks versus jet | 95 |
| ⁷⁹ | 8 | Summary | 97 |

⁸⁰ List of Figures

| | | | |
|----------------|----|--|----|
| ⁸¹ | 1 | QCD phase diagram | 11 |
| ⁸² | 2 | η/s vs $(T - T_c)/T_c$ | 12 |
| ⁸³ | 3 | The definitions of the Reaction Plane and Participant Plane coordinate systems | 15 |
| ⁸⁴ | 4 | Interaction between partons in central and peripheral collisions. | 16 |
| ⁸⁵ | 5 | An illustration of the multiplicity distribution in ALICE measurement with centrality classes. | 17 |
| ⁸⁶ | 6 | The results of one Glauber Monte Carlo simulation. | 20 |
| ⁸⁷ | 7 | Schematic representation of a heavy-ion collision | 21 |
| ⁸⁸ | 8 | Charged particle spectra | 22 |
| ⁸⁹ | 9 | Illustration of flow in momentum space in central and peripheral collisions. | 23 |
| ⁹⁰ | 10 | QCD Leading Order | 25 |
| ⁹¹ | 11 | Hard scattering | 25 |
| ⁹² | 12 | Jet showering | 26 |
| ⁹³ | 15 | Measurements of the nuclear modification factor R_{AA} in central heavy-ion collisions | 32 |
| ⁹⁴ | 16 | A comparison between observed $R_{AA}(\Delta\phi, p_T)$ and R_{AA} using v_2 | 33 |
| ⁹⁵ | 17 | Elliptic flow, v_2 from $p_T = 1$ to 60 GeV/c | 42 |
| ⁹⁶ | 18 | Photon spectrum | 43 |
| ⁹⁷ | 20 | Calculations of the intial energy density in small collision systems at RHIC and the resulting hydrodynamic evolution. | 45 |
| ⁹⁸ | 21 | Two-particle correlation results in PbPb, pPb, and pp collisions at the LHC []. | 45 |
| ⁹⁹ | 22 | RpA in proton-lead collisions | 45 |
| ¹⁰⁰ | 23 | Distribution of the sum of amplitudes in the V0A hodoscopes (Pb-going), as well as the NBD-Glauber fit (explained in the text). Centrality classes are indicated by vertical lines. The inset shows a zoom-in on the most peripheral events. [1] | 46 |

| | | | |
|-----|----|---|----|
| 110 | 24 | Top: Scatter plot of number of participating nucleons versus impact parameter; Bottom: Scatter plot of multiplicity versus the number of participating nucleons from the Glauber fit for V0A. The quantities are calculated with a Glauber Monte Carlo of p-Pb (left) and Pb-Pb (right) collisions. [1] | 47 |
| 111 | 25 | CERN collider complex | 49 |
| 112 | 26 | ALICE | 51 |
| 113 | 27 | ITS | 52 |
| 114 | 28 | TPC | 54 |
| 115 | 29 | An example image taken of a GEM foil with false colors. | 57 |
| 116 | 30 | Illustration of \vec{j}_T . The jet fragmentation transverse momentum, \vec{j}_T , is defined as the transverse momentum component of the track momentum, \vec{p}_{track} , with respect to the jet momentum, \vec{p}_{jet} | 66 |
| 117 | 31 | Inclusive j_T with background | 67 |
| 118 | 32 | Results from unfolding in Toy Monte Carlo | 71 |
| 119 | 33 | Jet p_T in unfolding closure test | 73 |
| 120 | 34 | j_T Response matrices in single jet p_T bins | 74 |
| 121 | 35 | Pythia closure test results. Fake tracks include also tracks that do exist in the true dataset, but for one reason or another were not given j_T values. j_T is only calculated for tracks that are associated with jets | 75 |
| 122 | 36 | Background estimation | 76 |
| 123 | 37 | Flowchart representation of the perpendicular cone background procedure | 76 |
| 124 | 38 | j_T background with two different methods | 78 |
| 125 | 39 | j_T signal with random bacgkround subtraction fits in different jet p_T bins | 81 |
| 126 | 40 | Differences between perpendicular cone and random background subtraction in the resulting RMS values. | 81 |
| 127 | 41 | Differences between Bayesian and SVD unfolding in the resulting RMS values | 82 |
| 128 | 42 | Unfolding with different number of iterations | 83 |
| 129 | 43 | Effect of changing minimum jet p_T used in unfolding from 5 to 10 GeV | 83 |
| 130 | 44 | Effect of changing minimum jet p_T used in unfolding from 5 to 10 GeV | 84 |
| 131 | 45 | Results from PYTHIA simulations with Cluster energies scale up/down by 2 %. Additionally jet momenta were scaled by 2 % when determining the jet p_T bin. | 85 |
| 132 | 46 | Relative systematic errors resulting from cluster energy uncertainty. | 85 |

| | | | |
|-----|----|--|----|
| 150 | 47 | Comparison of inclusive j_T distributions between A and C side for minimum bias and EMCAL triggered data. | 87 |
| 151 | 48 | j_T signal with background subtracted | 88 |
| 152 | 49 | Comparison of the effect of background method on j_T signal. | 88 |
| 153 | 50 | j_T signal fits in different jet p_T bins | 89 |
| 154 | 51 | RMS values extracted from the fits for the gaussian (narrow) and inverse gamma (wide) components | 90 |
| 155 | 52 | RMS values extracted from the fits for the gaussian (narrow) and inverse gamma (wide) components | 90 |
| 156 | 53 | j_T distributions for high multiplicity p-Pb events | 91 |
| 157 | 54 | Dihadron j_T results | 92 |
| 158 | 55 | RMS values of the narrow and wide j_T components in the dihadron correlation analysis. Results from pp collisions at $\sqrt{s} = 7$ TeV (circular symbols) and from p-Pb collisions at $\sqrt{s_{NN}} = 5.02$ TeV (square symbols) are compared to PYTHIA 8 tune 4C simulations at $\sqrt{s} = 7$ TeV (short dashed line) and at $\sqrt{s} = 5.02$ TeV (long dashed line). Different panels correspond to different x_{\parallel} bins with $0.2 < x_{\parallel} < 0.4$ on the left, $0.4 < x_{\parallel} < 0.6$ in the middle, and $0.6 < x_{\parallel} < 1.0$ on the right. The statistical errors are represented by bars and the systematic errors by boxes. [2] | 93 |
| 159 | 56 | Jet j_T results are compared to results obtained in the dihadron analysis. Dihadron trigger p_T bins are converted to jet p_T bins using observed mean $p_{T,jet}$ values in $p_{T,trigger}$ bins. Dihadron results are for $0.2 < x_{\parallel} < 0.4$ | 94 |
| 160 | 57 | Pythia R parameters j_T | 95 |
| 161 | 58 | Pythia R parameters RMS | 96 |
| 162 | 59 | Results of calculating j_T with respect to the jet axis or the leading hadron. The assumption is that because the leading hadron is an imperfect estimate of the jet axis, low j_T tracks should on average be shifted to higher j_T | 96 |

180 1 Introduction

181 REWRITE At sufficiently high energies quarks and gluons are no longer bound to
182 hadrons, but they form a deconfined state known as Quark-Gluon plasma (QGP).
183 The main goal of heavy ion physics is the study of QGP and its properties. One
184 of the experimental observables that is sensitive to the properties of QGP is the
185 azimuthal distribution of particles in the plane perpendicular to the beam direc-
186 tion.

187 When nuclei collide at non-zero impact parameter (non-central collisions), their
188 overlap region is asymmetric. This initial spatial asymmetry is converted via multi-
189 ple collisions into an anisotropic momentum distribution of the produced particles.
190 For low momentum particles ($p_T \lesssim 3$ GeV/c), this anisotropy is understood to
191 result from hydrodynamically driven flow of the QGP [3–7].

192 One way to characterize this anisotropy is with coefficients from a Fourier se-
193 ries parametrization of the azimuthal angle distribution of emitted hadrons. The
194 second order coefficient, v_2 which is also known as elliptic flow, shows clear depen-
195 dence on centrality. The collision geometry is mainly responsible for the elliptic
196 flow. Higher harmonics don't depend that much on centrality. These higher har-
197 monics carry information about the fluctuations in collisions. The event-by-event
198 fluctuations have an increasing importance in measurements and it has been ob-
199 served that measurements of elliptic flow in central collisions and measurements
200 of higher order harmonics are consistent with the assumption that flow in these
201 cases is mainly due to fluctuations [8].

202 At LHC energies $\sqrt{s_{NN}} = 2.76\text{GeV}$ it has been observed that in general there
203 is little difference to flow at RHIC energies. The v_2 coefficient is about 20% greater
204 at LHC than at RHIC, depending on the centrality bin. The particle identified
205 v_2 for kaons and pions follows the same trend. However it was observed that for
206 proton v_2 the quark number scaling does not work [9]. So far there is no agreement
207 of why this scaling breaks down at LHC or why it works so well at RHIC energies.

208

209 **1.1 Quantum chromodynamics**

210 **1.1.1 Foundation of QCD**

211 There are four known basic interactions in the universe: gravity, electromagnetic,
212 weak and strong interactions. The standard model of particle physics includes
213 three of these, excluding the gravitational interaction. The theory of strong inter-
214 actions is known as Quantum Chromodynamics (QCD).

215 The development of QCD began after the introduction of new powerful particle
216 accelerators that were capable of particle physics research in the 1950s. Before this
217 particles were mainly discovered from cosmic rays. Positrons, neutrons and muons
218 were discovered in the 1930s and charged pions were discovered in 1947 []. The
219 neutral pion was discovered in 1950 [10].

220 The Lawrence Berkeley National Laboratory started the Bevalac accelerator in
221 1954, Super Proton Synchrotron (SPS) in CERN began operating in 1959 and the
222 Alternating Gradient Synchrotron (AGS) at Brookhaven started in 1960. With
223 an energy of 33 GeV AGS was the most powerful accelerator of that time. By
224 the beginning of 1960s several new particles had been discovered. These included
225 antiprotons, antineutrons, Δ -particles and the six hyperons (Ξ^0 , Ξ^- , Σ^\pm , Σ^0 and
226 Λ).

227 Facing this avalanche of new particles, physicists started the search for symme-
228 tries within them. Already in 1932 Heisenberg [11] had proposed an isospin model
229 to explain similarities between the proton and the neutron. In 1962 Gell-Mann
230 and Ne'eman presented that particles sharing the same quantum numbers (spin,
231 parity) could be organised using the symmetry of SU(3). [12] Heisenberg's Isospin
232 model followed the symmetry of SU(2). Using the SU(3) model known baryons
233 and mesons could be presented as octets. This also lead to the discovery of the
234 Ω^- particle since this was missing from the SU(3) decouplet that included heavier
235 baryons.

236 The most simple representation of SU(3) was a triplet. Inside this triplet parti-
237 cles would have electric charges $2/3$ or $-1/3$. However, these had not been detected.
238 In 1964 Gell-Mann [13] and Zweig proposed that baryons and mesons would be
239 bound states of these three hypothetical triplet particles that Gell-Mann called
240 quarks. Now we know that these are the u , d and s quarks. This original quark
241 model without colour was violating the Pauli exclusion principle. For example
242 the Ω^- particle is comprised of three s quarks which would have exactly the same
243 quantum states.

244 The first one to present the idea of colour was Greenberg already in 1964 [14].
245 In 1971 Gell-Mann and Fritsch presented their model, which solved the antisym-
246 metry problem. They added a colour quantum number to quarks, which separated
247 quarks of the same species. In the new colour model the baryonic wave function

248 became

$$(qqq) \rightarrow (q_r q_g q_b - q_g q_r q_b + q_b q_r q_g - q_r q_b q_g + q_g q_b q_r - q_b q_g q_r), \quad (1)$$

249 The colour model was also supported by experimental evidence. The decay
250 rate of a neutral pion with the addition of colours is

$$\Lambda(\pi^0 \rightarrow \gamma\gamma) = \frac{\alpha^2}{2\pi} \frac{N_c^2}{3^2} \frac{m_\pi^3}{f_\pi^2}. \quad (2)$$

251 For $N_c = 3$ this gives 7.75 eV and the measured value is (7.86 ± 0.54) eV [15].

252 Another observable that combines the colour information also to the number
253 of quark flavours is The Drell-Ratio R [16]

$$R = \frac{\sigma(e^+ + e^- \rightarrow \text{hadrons})}{\sigma(e^+ + e^- \rightarrow \mu^+ + \mu^-)} = N_c \sum_f Q_f^2. \quad (3)$$

254 This ratio has the numerical value 2 when including the three light quarks u , d
255 and s . When the collision energy reaches the threshold of heavy quark (c and
256 b) production processes this increases to $^{10}/_3$ (for $f = u, d, s, c$) and $^{11}/_3$ (for $f =$
257 u, d, s, c, b). The threshold of $t\bar{t}$ production, $\sqrt{s} \approx 350$ GeV has not been reached
258 so far by any e^+e^- colliders.

259 The colour model explained why no free quarks had been observed as only
260 colour neutral states are possible. The simplest ways of producing a colour neu-
261 tral object are the combination of three quarks, and the combination of a quark-
262 antiquark pair. These are known as baryons and mesons.

263 After the addition of colour the main ingredients of QCD had been established.
264 The final quantum field theory of Quantum Chromodynamics formed quickly be-
265 tween 1972 and 1974. Main part of this was the work Gross, Wilczek, Politzer
266 and George did for non-abelian gauge field theories [17–21]. Gross, Wilczek and
267 Politzer received the Nobel Prize in Physics for their work. The role of gluons as
268 a colour octet was presented by Fritzsch, Gell-Mann and Leutwyler in 1973 [22].
269 The theory had now 8 massless gluons to mediate the strong interaction.

270 However, these gluons had not been discovered. Indirect evidence of the ex-
271 istence had been seen as it was observed that only about half of the momentum
272 of protons was transported by the quarks [23]. Direct evidence should be seen in
273 electron-electron collisions as a third, gluonic, jet in addition to two quark jets.
274 Three jet events were first seen in 1979 at the PETRA accelerator at DESY [24–26].

275 1.1.2 Asymptotic Freedom

276 In Quantum Electrodynamics (QED) the electric charge is screened. In the vicinity
277 of a charge, the vacuum becomes polarized. Virtual charged particle-antiparticle

278 pairs around the charge are arranged so that opposing charges face each other.
279 Since the pairs also include an equal amount opposite charge compared to the
280 original charge the average charge seen by an observer at a distance is smaller.
281 When the distance to the charge increases the effective charge decreases until the
282 coupling constant of QED reaches the fine-structure constant $\alpha = \frac{1}{137}$.

283 Contrary to QED, QCD is a non-abelian theory. In other words the generators
284 of the symmetry group of QCD, SU(3), do not commute. This has the practical
285 consequence that gluons interact also with other gluons, whereas in QED the
286 neutral carrier particles, photons, only interact with charged particles. There is
287 screening also in QCD because of the colour charges, but in addition to that there
288 is antiscreening because of the gluon interactions. In QCD the antiscreening effect
289 dominates over screening. For larger distances to the colour charge the coupling
290 constant is larger. This explains why no free colour charges can be observed. When
291 the distance between charges increases the interaction strengthens until it is strong
292 enough to produce a new quark-antiquark pair.

293 On the other hand, at very small distances the coupling constant approaches
294 0. This is called asymptotic freedom. For large energies and small distances
295 the coupling constant is negligible. In 1975 Collins [27] predicted a state where
296 individual quarks and gluons are no longer confined into bound hadronic states.
297 Instead they form a bulk QCD matter that Edward Shuryak called Quark-Gluon
298 plasma in his 1980 review of QCD and the theory of superdense matter [28]. QGP
299 can be seen as a separate state of matter. A schematic view of a phase diagram
300 for QCD matter is shown in Fig. 1.

301 In the early universe at the age of 10^{-6} s after the Big Bang the conditions
302 preferred the existence of QGP instead of hadronic matter. Nowadays bulk QCD
303 matter, its properties and its phase transitions between hadronic matter and the
304 quark-gluon plasma (QGP) can be explored in the laboratory, through collisions
305 of heavy atomic nuclei at ultra-relativistic energies. The study of QCD matter at
306 high temperature is of fundamental and broad interest. The phase transition in
307 QCD is the only phase transition in a quantum field theory that can be probed by
308 any present or foreseeable technology.

309 One important property of the QGP is the shear viscosity to entropy ratio,
310 η/s . It is believed that this ratio has an universal minimum value of $1/4\pi \approx 0.8$,
311 which holds for all substances. This limit would be reached in the strong coupling
312 limit of certain gauge theories [30]. The temperature dependance of the ratio is
313 shown in Fig. 2. The minimum value of η/s is found in the vicinity of the critical
314 temperature, T_c [31]. Finding the η/s values in QGP matter would therefore also
315 provide a way of determining the critical point of QCD matter.

316 The η/s value for the matter created in Au-Au collisions at RHIC ($\sqrt{s_{NN}}$) has
317 been estimated to be 0.09 ± 0.015 [31], which is very close to the lowest value for a

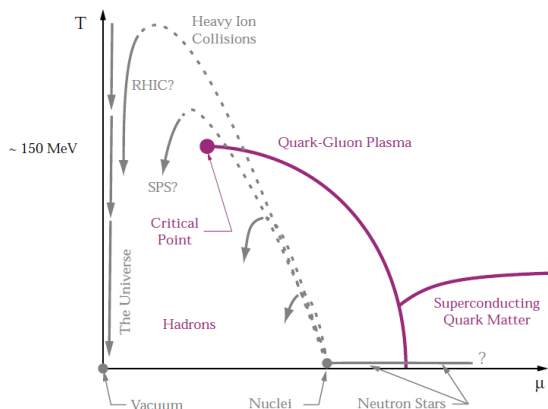


Figure 1: A schematic outline for the phase diagram of QCD matter at ultra-high density and temperature. The quark chemical potential μ that is on the x-axis represents the imbalance between quarks and antiquarks. At zero temperature this corresponds to the number of quarks but at higher temperatures there are also additional pairs of quarks and antiquarks. Along the horizontal axis the temperature is zero, and the density is zero up to the onset transition where it jumps to nuclear density, and then rises with increasing μ . Neutron stars are in this region of the phase diagram, although it is not known whether their cores are dense enough to reach the quark matter phase. Along the vertical axis the temperature rises, taking us through the crossover from a hadronic gas to the quark-gluon plasma. This is the regime explored by high-energy heavy-ion colliders. [29]

wide class of thermal quantum field theories [30] for all relativistic quantum field theories at finite temperature and zero chemical potential. This suggests that the matter created goes through a phase where it is close to the critical point of QCD.

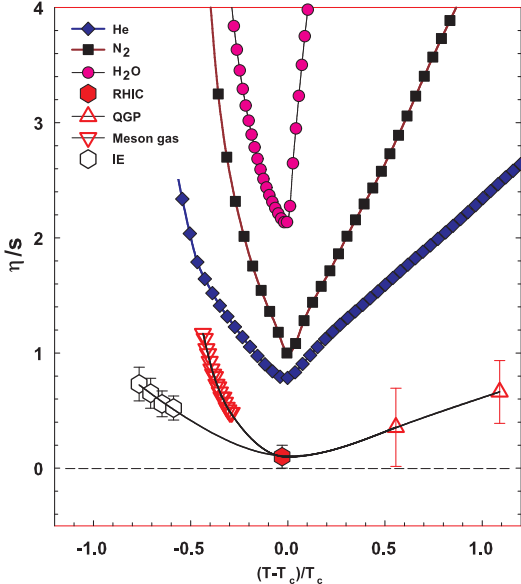


Figure 2: η/s as a function of $(T - T_c)/T_c$ for several substances as indicated. The calculated values for the meson-gas have an associated error of $\sim 50\%$. The lattice QCD value $T_c = 170$ MeV is assumed for nuclear matter. The lines are drawn to guide the eye. [31]

322 1.2 Heavy ion physics

323 The Quark Gluon Plasma (QGP) is experimentally accessible by colliding heavy
324 ions at high energies. Nowadays research of Heavy-Collisions is mainly performed
325 at two particle colliders; the The Relativistic Heavy Ion Collider (RHIC) at BNL
326 in New York, USA and he Large Hadron Collider (LHC) at CERN in Switzer-
327 land. Energy densities at these colliders should be enough to produce QGP and
328 convincing evidence of the creation has been seen at both colliders.

329 The development of heavy ion physics is strongly connected to the development
330 of particle colliders. Experimental study of relativistic heavy ion collisions has been
331 carried out for three decades, beginning with the Bevalac at Lawrence Berkeley
332 National Laboratory (LBNL) [32], and continuing with the AGS at Brookhaven
333 National Laboratory (BNL) [33], CERN SPS [34], RHIC at BNL and LHC at
334 CERN. The first colliders could not produce enough energy to create QGP matter
335 so they could only probe the hadronic state.

336 The collective motion of matter in a heavy-ion collision has been modeled using
337 several models e.g. the Blast wave Model [35] has been used successfully. Another
338 model growing in popularity is the hydrodynamical approach which is further
339 discussed in section 1.3.3.

340 1.2.1 History

341 The first heavy-ion collisions were done at the Bevalac experiment at the Lawrence
342 Berkeley National Laboratory [32] and at the Joint Institute for Nuclear Research
343 in Dubna [36] at energies up to 1GeV per nucleon. In 1986 the Super Pro-
344 ton Synchrotron (SPS) at CERN started to look for QGP signatures in O+Pb
345 collisions. The center-of-mass energy per colliding nucleon pair ($\sqrt{s_{NN}}$) was
346 19.4 GeV [34]. These experiments did not find any decisive evidence of the existence
347 of QGP. In 1994 a heavier lead (Pb) beam was introduced for new experiments at
348 $\sqrt{s_{NN}} \approx 17$ GeV. At the same time the Alternating Gradient Synchrotron (AGS)
349 at BNL, Brookhaven collided ions up to ^{32}S with a fixed target at energies up
350 to 28 GeV [33]. Although the discovery of a new state of matter was reported at
351 CERN, these experiments provided no conclusive evidence of QGP. Now SPS is
352 used with 400 GeV proton beams for fixed-target experiments, such as the SPS
353 Heavy Ion and Neutrino Experiment (SHINE) [37], which tries to search for the
354 critical point of strongly interacting matter.

355 The Relativistic Heavy Ion Collider (RHIC) at BNL in New York, USA started
356 its operation in 2000. The top center-of-mass energy per nucleon pair at RHIC, 200
357 GeV, was reached in the following years. The results from the experiments at RHIC
358 have provided a lot of convincing evidences that QGP was created [3,4,38,39]. The
359 newest addition to the group of accelerators capable of heavy-ion physics is the

³⁶⁰ Large Hadron Collider (LHC) at CERN, Switzerland. LHC started operating in
³⁶¹ November 2009 with proton-proton collisions. First Pb-Pb heavy ion runs started
³⁶² in November 2010 with $\sqrt{s_{NN}} = 2.76$ TeV, over ten times higher than at RHIC.
³⁶³ Among the six experiments at LHC, the Large Ion Collider Experiment (ALICE)
³⁶⁴ is dedicated to heavy ion physics. Also CMS and ATLAS have active heavy ion
³⁶⁵ programs.

366 **1.3 Features of Heavy-Ion Collisions**

367 **1.3.1 Collision Geometry**

368 In contrast to protons atomic nuclei are objects with considerable transverse size.
369 The properties of a heavy-ion collision depend strongly on the impact parameter
370 b which is the vector connecting the centers of the two colliding nuclei at their
371 closest approach. One illustration of a heavy-ion collision is shown in Fig. 3.

372 Impact parameter defines the reaction plane which is the plane spanned by b
373 and the beam direction. Ψ_{RP} gives the angle between the reaction plane and some
374 reference frame angle. Experimentally the reference frame is fixed by the detector
375 setup. Reaction plane angle cannot be directly measured in high energy nuclear
 collisions, but it can be estimated with the event plane method [40].

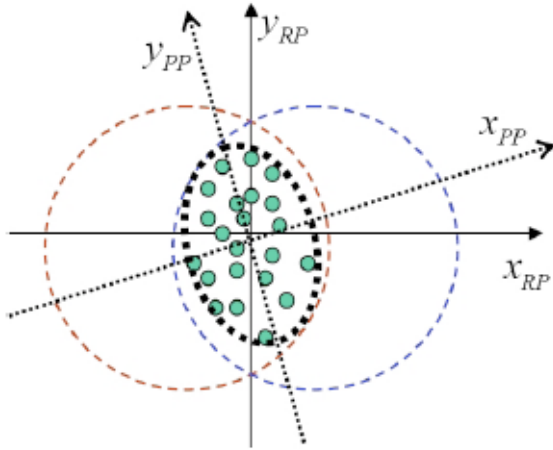


Figure 3: The definitions of the Reaction Plane and Participant Plane coordinate systems [41]. The dashed circles represent the two colliding nuclei and the green dots are partons that take part in the collision. x_{PP} and x_{RP} are the participant and reaction planes. The angle between x_{RP} and x_{PP} is given by Eq. (4). y_{PP} and y_{RP} are lines perpendicular to the participant and reaction planes.

376
377 Participant zone is the area containing the participants. The distribution of
378 nucleons in the nucleus exhibits time-dependent fluctuations. Because the nucleon
379 distribution at the time of the collision defines the participant zone, the axis of
380 the participant zone fluctuates and can deviate from the reaction plane. The angle
381 between the participant plane and the reaction plane is defined by [42]

$$\psi_{PP} = \arctan \frac{-2\sigma_{xy}}{\sigma_y^2 - \sigma_x^2 + \sqrt{(\sigma_y^2 - \sigma_x^2)^2 + 4\sigma_{xy}^2}}, \quad (4)$$

382 where the σ -terms are averaged over the energy density.

$$\sigma_y^2 = \langle y^2 \rangle - \langle y \rangle^2, \sigma_x^2 = \langle x^2 \rangle - \langle x \rangle^2, \sigma_{xy} = \langle xy \rangle - \langle x \rangle \langle y \rangle \quad (5)$$

383 The impact parameter is one way to quantize the centrality of a heavy-ion
 384 collision but it is impossible to measure in a collision. It can be estimated from
 385 observed data using theoretical models, but this is always model-dependent and
 386 to compare results from different experiments one needs an universal definition for
 387 centrality. The difference between central and peripheral collisions is illustrated
 388 in Fig. 4. In a central collision the overlap region is larger than in a peripheral
 389 collision. Larger overlap region translates into a larger number of nucleons partici-
 390 pating in the collision, which in turn leads to a larger number of particles produced
 391 in the event.

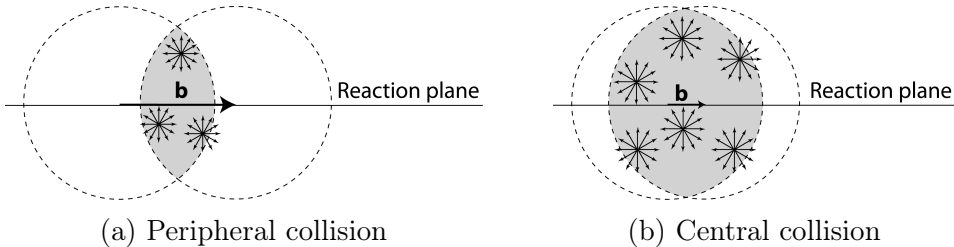


Figure 4: Interaction between partons in central and peripheral collisions. The snowflakes represent elementary parton-parton collisions. When the impact parameter b is large the number of elementary collisions is small. Particle production is small. Smaller impact parameter increases the number of elementary collisions. This increases particle production.

392 Usually centrality is defined by dividing collision events into percentile bins by
 393 the number participants or experimentally by the observed multiplicity. Centrality
 394 bin 0-5% corresponds to the most central collisions with the highest multiplicity
 395 and higher centrality percentages correspond to more peripheral collisions with
 396 lower multiplicities. A multiplicity distribution from ALICE measurements [43]
 397 illustrating the centrality division is shown in Fig. 5. The distribution is fitted
 398 using a phenomenological approach based on a Glauber Monte Carlo [44] plus a
 399 convolution of a model for the particle production and a negative binomial distri-
 400 bution.

401 1.3.2 Nuclear Geometry

402 To model heavy-ion collisions one must first have a description as good as possible
 403 of the colliding objects. Atomic nuclei are complex ensembles of nucleons. The
 404 nuclei used in heavy-ion physics have in the order of 200 nucleons. Mostly used

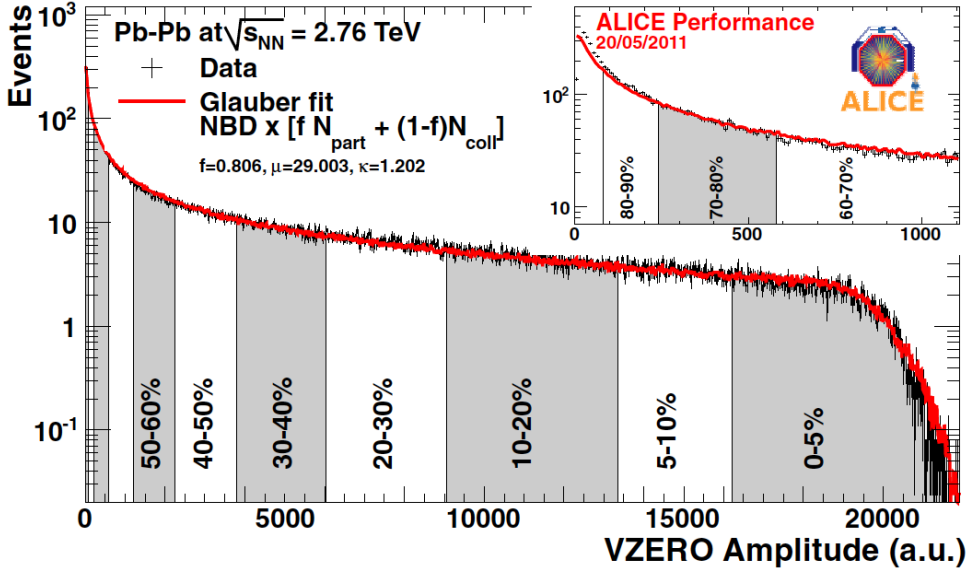


Figure 5: An illustration of the multiplicity distribution in ALICE measurements. The red line shows the fit of the Glauber calculation to the measurement. The data is divided into centrality bins [43]. The size of the bins corresponds to the indicated percentile.

405 nuclei are ^{208}Pb at LHC and ^{197}Au at RHIC. The distribution of these nucleons
 406 within a nucleus is not uniform and is subject to fluctuations in time.

407 Nuclear geometry in heavy-ion collisions is often modelled with the Glauber
 408 Model. The model was originally developed to address the problem of high energy
 409 scattering with composite particles. Glauber presented his first collection of papers
 410 and unpublished work in his 1958 lectures [45]. In the 1970's Glauber's work
 411 started to have utility in describing total cross sections. Maximon and Czyz applied
 412 it to proton-nucleus and nucleus-nucleus collisions in 1969 [46].

413 In 1976 [47] Białas, Bleszyński, and Czyz applied Glauber's approach to
 414 inelastic nuclear collisions. Their approach introduced the basic functions used in
 415 modern language including the thickness function and the nuclear overlap function.
 416 Thickness function is the integral of the nuclear density over a line going through
 417 the nucleus with minimum distance s from its center

$$T_A(s) = \int_{-\infty}^{\infty} dz \rho \left(\sqrt{s^2 + z^2} \right). \quad (6)$$

418 This function gives the thickness of the nucleus, i.e. the amount material seen by
 419 a particle passing through it.

⁴²⁰ Overlap function is an integral of the thickness functions of two colliding nuclei
⁴²¹ over the overlap area. This can be seen as the material that takes part in the
⁴²² collision. It is given as a function of the impact parameter b

$$T_{AB}(b) = \int ds^2 T_A(\bar{s}) T_B(\bar{s} - \bar{b}) \quad (7)$$

⁴²³ The average overlap function, $\langle T_{AA} \rangle$, in an A-A collisions is given by [48]

$$\langle T_{AA} \rangle = \frac{\int T_{AA}(b) db}{\int (1 - e^{-\sigma_{pp}^{inel} T_{AA}(b)}) db}. \quad (8)$$

⁴²⁴ Using $\langle T_{AA} \rangle$ one can calculate the mean number of binary collisions

$$\langle N_{coll} \rangle = \sigma_{pp}^{inel} \langle T_{AA} \rangle, \quad (9)$$

⁴²⁵ where the total inelastic cross-section, σ_{pp}^{inel} , gives the probability of two nucleons
⁴²⁶ interacting. The number of binary collisions is related to the hard processes in a
⁴²⁷ heavy-ion collision. Each binary collision has equal probability for direct produc-
⁴²⁸ tion of high-momentum partons. Thus the number of high momentum particles is
⁴²⁹ proportional to $\langle N_{coll} \rangle$.

⁴³⁰ Soft production on the other hand is related to the number of participants.
⁴³¹ It is assumed that in the binary interactions participants get excited and further
⁴³² interactions are not affected by previous interactions because the time scales are
⁴³³ too short for any reaction to happen in the nucleons. After the interactions ex-
⁴³⁴ cited nucleons are transformed into soft particle production. Production does not
⁴³⁵ depend on the number of interactions a nucleon has gone through. The average
⁴³⁶ number of participants, $\langle N_{part} \rangle$ can also be calculated from the Glauber model

$$\begin{aligned} \langle N_{part}^{AB}(b) \rangle &= \int ds^2 T_A(\bar{s}) \left[1 - \left[1 - \sigma_{NN} \frac{T_B(\bar{s} - \bar{b})}{B} \right]^B \right] \\ &+ \int ds^2 T_B(\bar{s}) \left[1 - \left[1 - \sigma_{NN} \frac{T_A(\bar{s} - \bar{b})}{A} \right]^A \right]. \end{aligned} \quad (10)$$

⁴³⁷ Glauber calculations require some knowledge of the properties of the nuclei.
⁴³⁸ One requirement is the nucleon density distribution, which can be experimen-
⁴³⁹ tally determined by studying the nuclear charge distribution in low-energy elec-
⁴⁴⁰ tron scattering experiments [44]. The nucleon density is usually parametrized by
⁴⁴¹ a Woods-Saxon distribution

$$\rho(r) = \frac{\rho_0}{1 + \exp\left(\frac{r-R}{a}\right)}, \quad (11)$$

where ρ_0 is the nucleon density in center of the nucleus, R is the nuclear radius and a parametrizes the depth of the skin. The density stays relatively constant as a function of r until around R where it drops to almost 0 within a distance given by a .

Another observable required in the calculations is the total inelastic nucleon-nucleon cross-section $\sigma_{\text{inel}}^{\text{NN}}$. This can be measured in proton-proton collisions at different energies.

There are two often used approaches to Glauber calculations. The optical approximation is one way to get simple analytical expressions for the nucleus-nucleus interaction cross-section, the number of interacting nucleons and the number of nucleon-nucleon collisions. In the optical Glauber it is assumed that during the crossing of the nuclei the nucleons move independently and they will be essentially undeflected.

With the increase of computational power at hand the Glauber Monte Carlo (GMC) approach has emerged as a method to get a more realistic description of the collisions. In GMC the nucleons are distributed randomly in three-dimensional coordinate system according to the nuclear density distributions. Also nuclear parameters, like the radius R can be sampled from a distribution. A heavy-ion collision is then treated as a series of independent nucleon-nucleon collisions, where in the simplest model nucleons interact if their distance in the plane orthogonal to the beam axis, d , satisfies

$$d < \sqrt{\sigma_{\text{inel}}^{\text{NN}}} \quad (12)$$

The average number of participants and binary collisions can then be determined by simulating many nucleus-nucleus collisions. The results of one GMC Pb-Pb event with impact parameter $b = 9.8$ fm is shown in Fig. 6

1.3.3 Hydrodynamical Modelling

The relativistic version of hydrodynamics has been used to model the deconfined phase of a heavy-ion collision with success. Heavy-ion collisions produce many hadrons going into all directions. It is expected that tools from statistical physics would be applicable to this complexity [49]. The power of relativistic hydrodynamics lies in its simplicity and generality. Hydrodynamics only requires that there is local thermal equilibrium in the system. In order to reach thermal equilibrium the system must be strongly coupled so that the mean free path is shorter than the length scales of interest [50].

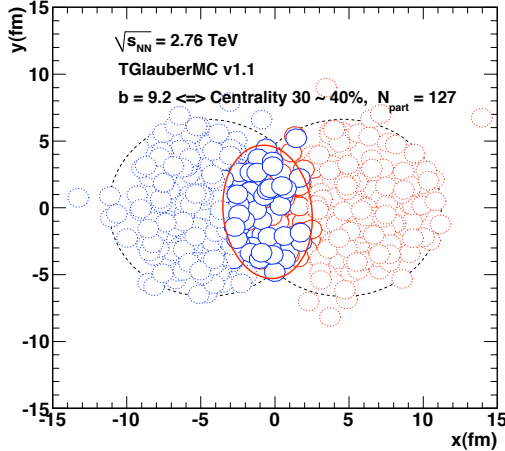


Figure 6: The results of one Glauber Monte Carlo simulation. Big circles with black dotted boundaries represent the two colliding nuclei. The participant zone is highlighted with the solid red line. Small red and blue circles represent nucleons. Circles with thick boundaries are participants i.e. they interact with at least one nucleon from the other nucleus. Small circles with dotted boundaries are spectators which do not take part in the collision.

475 The use of relativistic hydrodynamics in high-energy physics dates back to
 476 Landau [51] and the 1950's, before QCD was discovered. Back then it was used
 477 in proton-proton collisions. Development of hydrodynamics for the use of heavy-
 478 ion physics has been active since the 1980's, including Bjorken's study of boost-
 479 invariant longitudinal expansion and infinite transverse flow [?]. Major steps were
 480 taken later with the inclusion of finite size and and dynamically generated trans-
 481 verse size [?, ?], a part of which was done at the University of Jyväskylä. The role
 482 of hydrodynamics in heavy-ion physics was strengthened when QGP was observed
 483 to behave like a liquid by RHIC [3].

484 The evolution of a heavy-ion event can be divided into four stages. A schematic
 485 representation of the evolution of the collisions is shown in Fig. 7. Stage 1 follows
 486 immediately the collision. This is known as the pre-equilibrium stage. Hydrody-
 487 namic description is not applicable to this regime because thermal equilibrium is
 488 not yet reached. The length of this stage is not known but it is assumed to last
 489 about $1 \text{ fm}/c$ in proper time τ .

490 The second stage is the regime where thermal equilibrium or at least near-
 491 equilibrium is reached. In this stage hydrodynamics should be applicable if the
 492 temperature is above the deconfinement temperature [50]. This lasts about $5 -$
 493 $10 \text{ fm}/c$ until the temperature of the system sinks low enough for hadronization to

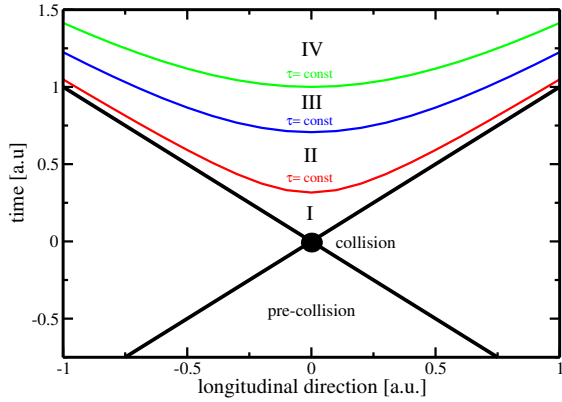


Figure 7: Schematic representation [50] of a heavy-ion collision as the function of time and longitudinal coordinates z . The various stages of the evolution correspond to proper time $\tau = \sqrt{t^2 - z^2}$ which is shown as hyperbolic curves separating the different stages.

494 occur. Now the system loses its deconfined, strongly coupled, state and hydrodynamics
 495 can no longer be used. The third stage is the hadron gas stage where the
 496 hadrons still interact. This ends when hadron scattering becomes rare and they
 497 no longer interact. In the final stage hadrons are free streaming and they fly in
 498 straight lines until they reach the detector.

499 The hydrodynamical approach treats the ensemble of particles as a fluid. It
 500 uses basic equations from hydrodynamics and thermodynamics but with a few
 501 modifications to account for the relativistic energies. The calculation is based
 502 on a collection of differential equations connecting the local thermal variables like
 503 temperature, pressure etc. to local velocities of the fluid. One also needs equations
 504 of state that connect the properties of the matter, e.g. temperature and pressure
 505 to density. Given initial conditions and equations of state the calculation gives the
 506 time-evolution of the system.

507 At first only ideal hydrodynamics was used. Ideal hydrodynamics does not
 508 include viscosity but it is a relatively good approximation and it could predict
 509 phenomena like elliptic flow. For more detailed calculations also viscosity must be
 510 considered and viscosity itself is an interesting property of QGP.

511 1.4 Flow

512 In a heavy-ion collision the bulk particle production is known as flow. The pro-
 513 duction is mainly isotropic but a lot of studies including my thesis focus on the
 514 small anisotropies. After the formation of the QGP, the matter begins to expand
 515 as it is driven outwards by the strong pressure difference between the center of the
 516 collision zone and the vacuum outside the collision volume. The pressure-driven
 517 expansion is transformed into flow of low-momentum particles in the hadroniza-
 518 tion phase. Since the expansion is mainly isotropic the resulting particle flow is
 519 isotropic with small anisotropic corrections that are of the order of 10% at most.
 520 The isotropic part of flow is referred to as radial flow.

521 The transverse momentum spectra dN/dp_T in heavy-ion collisions is shown

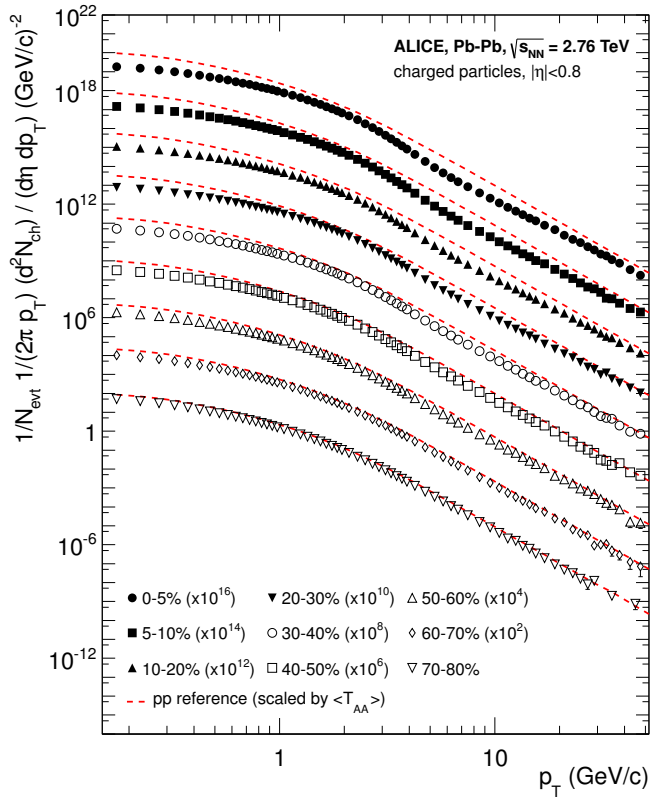


Figure 8: Charged particle spectra measured by ALICE [54] for the 9 centrality classes given in the legend. The distributions are offset by arbitrary factors given in the legend for clarity. The distributions are offset by arbitrary factors given in the legend for clarity. The dashed lines show the proton-proton reference spectra scaled by the nuclear overlap function determined for each centrality class and by the Pb-Pb spectra scaling factors [54].

522 in Fig. 8. The vast majority of produced particles have small p_T . The difference
 523 between the yield of 1 GeV/c and 4 GeV/c particles is already 2-3 orders of mag-
 524 nitude. Any observables that are integrated over p_T are therefore dominated by
 525 the small momentum particles.

526 1.4.1 Anisotropic Flow

527 In a non-central heavy-ion collision the shape of the impact zone is almond-like.
 528 In peripheral collisions the impact parameter is large which means a strongly
 529 asymmetric overlap region. In a central collision the overlap region is almost
 530 symmetric in the transverse plane. In this case the impact parameter is small.
 531 Collisions with different impact parameters are shown in Fig. 4.

532 The pressure gradient is largest in-plane, in the direction of the impact pa-
 533 rameter b , where the distance from high pressure, at the collision center, to low
 534 pressure, outside the overlap zone, is smallest. This leads to stronger collective
 535 flow into in-plane direction, which in turn results in enhanced thermal emission
 536 through a larger effective temperature into this direction, as compared to out-of-
 537 plane [5, 6, 55]. The resulting flow is illustrated in Fig. 9. Flow with two maxima
 538 in the direction of the reaction plane is called elliptic flow. This is the dominant

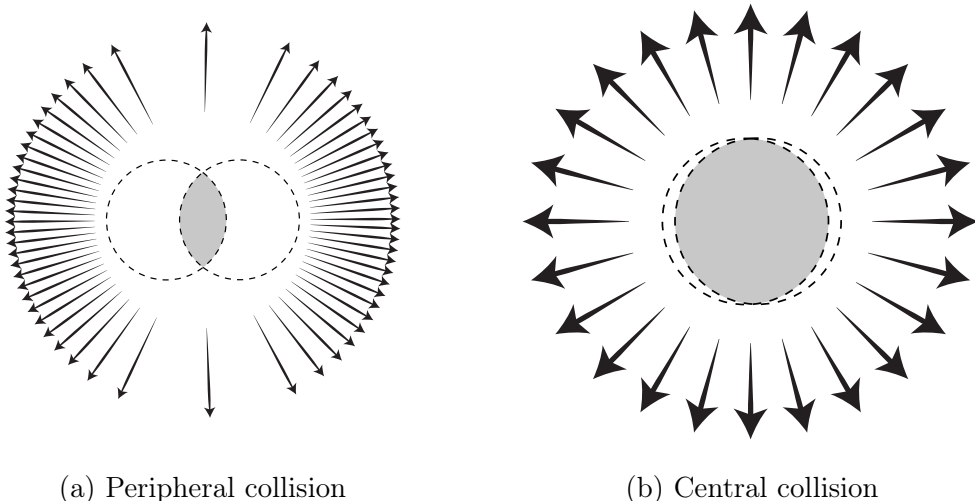


Figure 9: Illustration of flow in momentum space in central and peripheral collisions. The density of the arrows represent the magnitude of flow seen at a large distance from the collision in the corresponding azimuthal direction. In a peripheral collision momentum flow into in-plane direction is strong and flow into out-of-plane direction is weak. In a central collision anisotropy in flow is smaller, but the total yield of particles is larger.

part of anisotropic flow. Also more complex flow patterns can be identified. The most notable of these is the triangular flow, which is mainly due to fluctuations in the initial conditions.

Flow is nowadays usually quantified in the form of a Fourier composition

$$E \frac{d^3N}{dp^3} = \frac{1}{2\pi p_T} \frac{d^2N}{dp_T d\eta} \left(1 + \sum_{n=1}^{\infty} 2v_n(p_T, \eta) \cos(n(\phi - \Psi_n)) \right), \quad (13)$$

where the coefficients v_n give the relative strengths of different anisotropic flow components and the overall normalisation gives the strength of radial flow. Elliptic flow is represented by v_2 and v_3 represents triangular flow. The first coefficient, v_1 , is connected to directed flow. This will however in total be zero because of momentum conservation. It can be nonzero in some rapidity or momentum regions but it must be canceled by other regions.

The first approaches to quantifying the anisotropy of flow did not use the Fourier composition. Instead they approached the problem with a classic event shape analysis using directivity [56] or sphericity [5, 57] to quantify the flow.

The first experimental studies of anisotropy were performed at the AGS [58] in 1993. They noted that the anisotropy of particle production in one region correlates with the reaction plane angle defined in another region.

The first ones to present the Fourier decomposition were Voloshin and Zhang in 1996 [59]. This new approach was useful for detecting different types of anisotropy in flow, since the different Fourier coefficients give different harmonics in flow. They also show the relative magnitude of each harmonic compared to radial flow.

Some parts of the Fourier composition approach were used for Au-Au collisions at $\sqrt{s_{NN}} = 11.4\text{GeV}$ at AGS in 1994 [60]. This analysis still focused on event shapes but they constructed these shapes using Fourier composition from different rapidity windows.

1.4.2 High p_T Phenomena

The measurement of anisotropic flow coefficients can be extended to very high transverse momenta p_T . High p_T measurements of v_2 from CMS [61] are shown in Fig. 17. For high transverse momenta v_2 values are positive and they decrease slowly as a function of p_T . At high transverse momentum the v_2 values don't, however, represent flow.

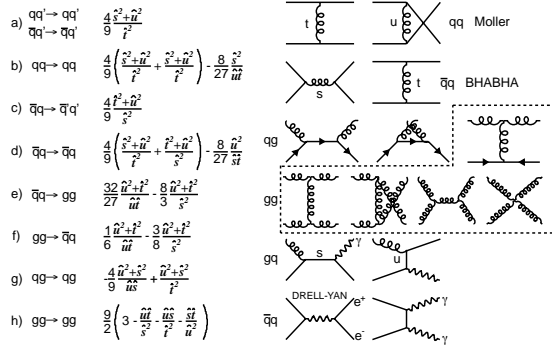


Figure 10: The basic pQCD processes and their quadratic matrix elements

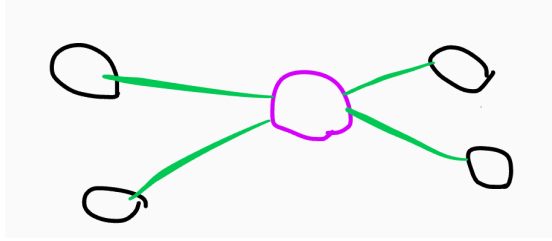


Figure 11: Schematic view of hard scattering process of $p + p \rightarrow 2 \text{jets}$

569 1.5 Hard processes

570 1.5.1 pQCD factorization

571 The term Hard Scattering is used in connection with the scattering of two point-like constituents (partons) of colliding nucleons, when the momentum transfer Q^2
 572 is large ($Q \gg \Lambda_{\text{QCD}}$). Figure ?? shows the incoming partons, quarks or gluons, as
 573 they exchange a space-like virtual gluon and produce two highly virtual outgoing
 574 partons. The outgoing partons will eventually fragment into collimated showers of
 575 partons, referred to as jets

577 Jet fragmentation can be factorised into three components; the parton distribution functions f_a, f_b that give the probability of getting a parton with momentum fraction x of the proton, the cross section of the elementary scattering $ab \rightarrow cd$ (Fig. 10) and the fragmentation functions that give the probability of getting hadron h from the parton.

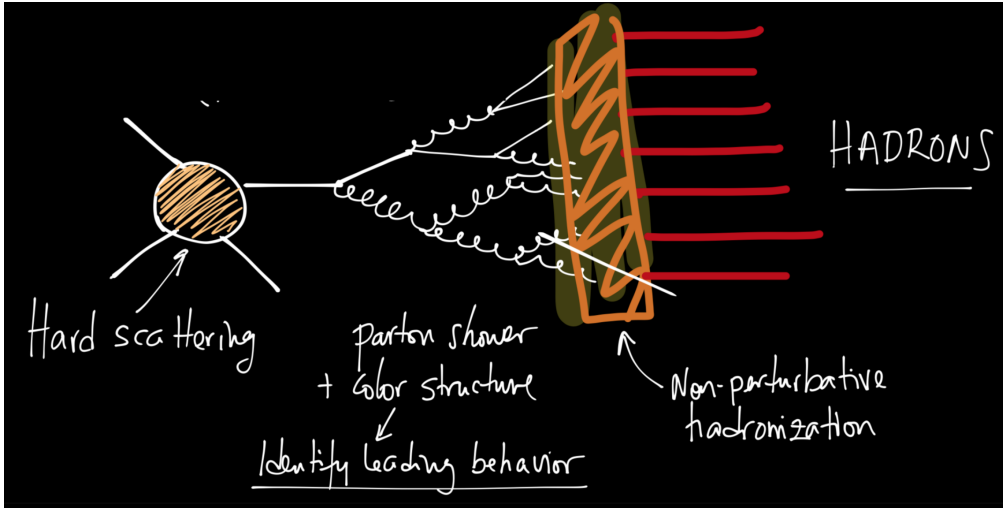


Figure 12: REPLACE FIGURE An illustration of jet showering. The highly virtual parton from the hard scattering will produce a shower of softer partons. When the virtuality is low enough the shower will go through a hadronisation process that produces the hadrons, which will be eventually observed in the detector.

$$\frac{d\sigma_{pp}^h}{dy d^2 p_T} = K \sum_{abcd} \int dx_a dx_b f_a(x_a, Q^2) f_b(x_b, Q^2) \frac{d\sigma}{dt} (ab \rightarrow cd) \frac{D_{h/c}^0}{\pi z_c}$$

$$x_a = \frac{|p_a|}{|p_{proton}|}$$

582 Parton Distribution Function

583 Parton Distribution Functions (PDFs) are essential to calculate the scattering cross
584 section. They are extracted from comprehensive global analysis of experimental
585 results from a variety of fixed-target and collider experiments. PDFs $f_a(x)$ give the
586 differential probability for parton a to carry momentum fraction x of the proton
587 momentum.

588 PDFs cannot be calculated from first principles. In practice the PDFs are
589 measured in Deeply Inelastic Scattering (DIS) experiments and are extrapolated
590 to the relevant momentum scales at LHC using the Dokshitzer-Gribov-Lipatov-
591 Altarelli-Parisi (DGLAP) evolution scheme [?] 14.

$$\mu_F^2 \frac{\partial f_i(x, \mu_F^2)}{\partial \mu_F^2} = \sum_j \frac{\alpha_s(\mu_F)}{2\pi i} \int_x^1 \frac{dz}{z} P_{ij}(z) f_j\left(\frac{x}{z}, \mu_F^2\right), \quad (14)$$

592 where μ_F is a factorization scale. The splitting functions P_{ij} describe a probability to radiate parton i from parton j as a function of the momentum fraction z carried away by the offspring parton.

595 The final component in the factorization, fragmentation functions, describe
596 the distribution of the fractional momenta of particles radiated from the outgoing
597 parton. Fragmentation function are given with respect to the momentum fraction
598 z which is defined as the longitudinal momentum fraction of jet momentum p_{jet}
599 carried away by the jet fragment p_{part}

$$z = \frac{\bar{p}_{\text{part}} \cdot \bar{p}_{\text{jet}}}{\bar{p}_{\text{jet}}^2} = \frac{p_{\text{part}}}{p_{\text{jet}}} \Big|_{\bar{p}_{\text{part}} \times \bar{p}_{\text{jet}} = 0} \quad (15)$$

600 Fragmentation function $D(z)$ then gives the average multiplicity m of jet fragments having $z > z_0$ [].

$$m(z_0) = \int_{z_0}^1 D(z) dz \Rightarrow m(0) \equiv \langle m \rangle = \int_0^1 D(z) dz \quad (16)$$

602 Because of momentum conservation the sum of all jet fragments must be equal
603 to the jet momentum, i.e.

$$\sum p_{i,\text{part}} = p_{\text{jet}} \Rightarrow \sum z_i = 1 \Rightarrow \int_0^1 z D(z) dz = 1 \quad (17)$$

604 A natural consequence is that the average momentum fraction is the inverse of
605 the average multiplicity

$$\langle z \rangle = \frac{\int_0^1 z D(z)}{\int_0^1 D(z)} = \frac{1}{\langle m \rangle} \quad (18)$$

606 1.5.2 Jet hadronisation

607 When the parton shower reaches a scale close to Λ_{QCD} , the perturbative description
608 is no longer valid. Thus the hadronisation stage must be described in a
609 non-perturbative manner. One simple scenario that is used in several theory calculations
610 is the so-called local parton-hadron duality [62]. In the local parton-hadron
611 duality hypothesis it is assumed that there exists a low virtuality scale Q_0 in which
612 the hadronisation happens, that is independent of the scale of the primary hard
613 process. At this scale the partons are transformed into hadrons, assuming that the
614 flow of momentum and quantum numbers for the hadrons can be directly obtained
615 from those of partons introducing only small normalising constants.

616 Hadronisation is assumed to be universal, i.e. it shouldn't depend on the
617 collision energy or system.

618 **Lund string model**

619 One common implementation in MC generators is the Lund string fragmentation
 620 algorithm [63]. The string model is based on the fact that in QCD linear confine-
 621 ment is expected over large distances [64]. This can be modelled by imagining a
 622 colour flux tube being stretched between the outgoing partons. The left side of
 623 Fig. 14 illustrates this point for a $q\bar{q}$ -pair. The tube is assumed to have a uniform
 624 fixed transverse size of about 1 fm along its length, which leads to a linearly rising
 625 potential $V(r) = \kappa r$, where the string constant κ describes the amount of energy
 626 per unit length. A value of $\kappa \approx 1\text{GeV}/\text{fm} \approx 0.2\text{GeV}^2$ can be obtained from hadron
 627 mass spectroscopy.

628 The evolution of string fragmentation is illustrated schematically on the right
 629 side of Fig. 14. This figure is drawn in a light cone presentation, so the initial
 630 quark and antiquark are going to separate directions at the speed of light, which
 631 assumes them as massless. The string between them, illustrated in the figure by
 632 the red line, stretches until its potential energy becomes high enough that it can
 633 break, forming a new quark-antiquark pair. If the original pair was $q\bar{q}$ and the
 634 new pair $q'\bar{q}'$, now two new pairs $q\bar{q}'$ and $q'\bar{q}$ have formed. As these particles
 635 are also moving away from each other, the strings between them can stretch and
 636 break, creating yet more pairs. The process continues until the invariant mass of
 637 the system connected by the string becomes small enough and a final state meson
 638 is formed.

639 To mathematically model the string one can use a massless relativistic string
 640 with no transverse degrees of freedom. The gluons are represented as energy and
 641 momentum carrying kinks on the string with incoherent sums of one colour charge
 642 and one anticolour charge. When this string breaks, it is classically required that
 643 the created quark and antiquark are produced at a certain distance if they are to
 644 have any mass or transverse momentum. However, taking into account quantum
 645 mechanics, the pair must be created at one point and then tunnel out to the
 646 classically allowed region. Thus the probability to create a new quark-antiquark
 647 pair becomes proportional to the tunnelling probability [63].

$$P_{\text{tunnelling}} \propto \exp\left(\frac{-\pi m_\perp^2}{\kappa}\right) = \exp\left(\frac{-\pi m^2}{\kappa}\right) \left(\frac{-\pi p_\perp^2}{\kappa}\right), \quad (19)$$

648 where the transverse mass m_\perp is defined as $m_\perp^2 = m^2 + p_\perp^2$. The transverse
 649 momentum is now defined to be transverse to the string axis. This formula gives
 650 flavour-independent Gaussian p_\perp -distribution for the created $q\bar{q}$ pairs.

651 As explained above the string fragmentation would only produce mesons in
 652 the final state, but we know that also baryons are created in the process. In the
 653 string fragmentation model baryon production is included by adding a probability
 654 that a diquark-antidiquark pair is created instead of a quark-antiquark pair when

655 a string breaks.

656 The kinematics of each string breaking are determined iteratively. Since there
657 is no natural ordering, the string breaking can be considered in any order and
658 the answer obtained must be the same. One can start from the q leg and work
659 one's way to the \bar{q} leg, or vice versa. This give a left-right symmetry of the
660 string fragmentation. In the Lund model this is taken into account by defining a
661 symmetric fragmentation function

$$f(z) \propto \frac{1}{z} (1-z)^a \exp\left(-\frac{bm_{\perp}^2}{z}\right) \quad (20)$$

662 to break the string into a hadron and a remainder system. In the function z is
663 the fraction of light-cone momentum p^+ given to the hadron in the string breaking,
664 m_{\perp} is the transverse mass of the hadron and a and b are tuneable parameters of
665 the model. For heavy quarks this has to be modified as

$$f(z) \propto \frac{1}{z^{1+bm_Q^2}} (1-z)^a \exp\left(-\frac{bm_{\perp}^2}{z}\right) \quad (21)$$

666 The process can be thought as follows: first start from the q-leg of a $q\bar{q}$ system
667 and choose to consider the breaking to new $q'\bar{q}'$ pair closest to this leg. Now the
668 breaking will produce a hadron $q\bar{q}'$ and a remainder system spanning from $q'\bar{q}$.
669 Then the process is continued until the \bar{q} -leg is reached. A small detail here is
670 that in equation (20) it is assumed that the mass of the remainder system is large.
671 Thus some patching up is needed for the last two hadrons coming from a string.
672 The patching up is done such that the place where it happens looks as closely like
673 any other string break as possible.

674 One additional possibility one must consider is that a string can have such a
675 low mass that it cannot break at all. In this case a single hadron is generated out
676 of the string and if necessary energy and momentum are exchanged with other
677 partons in the event.

678 After all the hadrons are produced, the short-lived ones can still decay before
679 the set of final state particles in the simulation is obtained []

680 Cluster model

681 Instead of a string model HERWIG [] uses a cluster model [65] for hadronisation.
682 The advantage of cluster models is that they require a smaller number of param-
683 eters than string models. The model is based on the preconfinement property of
684 parton showers, i.e. the colour structure of the shower at any evolution scale Q_0 is
685 such that colour singlet combinations of partons can be formed with an asymptot-
686 ically universal invariant mass distribution. The invariant mass does not depend

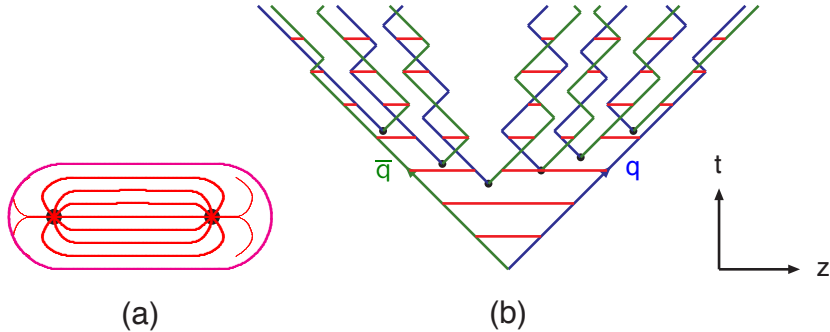


Figure 13: (a) A flux tube spanned between a quark and an antiquark. (b) The motion and breakup of a string system, with the two transverse degrees of freedom suppressed (diagonal lines are (anti)quarks, horizontal ones snapshots of the string field). [64]

on the initial hard process scale Q , but only on Q_0 and the QCD scale Λ_{QCD} , when $Q \gg Q_0$.

The cluster model starts from transforming all gluons non-perturbatively into $q\bar{q}$ pairs, which requires that the gluons get a mass, which must be at least twice the lightest quark mass. After the gluons are transformed into quarks, the adjacent colour lines can be clustered together to colour singlet states with mesonic quantum numbers. The momentum of these clusters is defined to be the sum of the momenta of the clustering partons. According to preconfinement, the mass distribution of these clusters is independent of the details of the hard scattering. Additionally the clusters can be regarded as highly excited hadron resonances and decayed into the final state hadrons.

Some of these initial clusters are too heavy to reasonably describe an excited state of a hadron. These must be split before they are allowed to decay. The cluster C is split if its mass fulfills the condition []

$$M_C^p \geq M_{\max}^p + (m_1 + m_2)^p, \quad (22)$$

where $m_{1,2}$ are the masses of the constituents partons of the cluster and M_{\max} and p are the main parameters of the model. These have to be chosen separately for clusters containing light, charmed and bottom quarks. When a cluster is split, a pair of light quarks is generated from the vacuum and two new clusters are made, both containing one quark from the original cluster and one from the newly generated pair. The splitting is continued until no clusters with masses M_C fulfilling the equation 22 remains.

When the clusters are light enough, they decay into final state hadrons. If the mass of the cluster is high enough for decaying into a baryon-antibaryon pair,

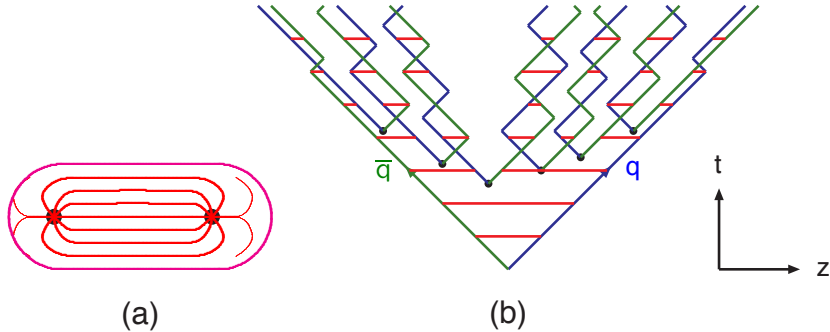


Figure 14: Colour structure of a parton shower to leading order in N_c . [64]

there is a parameter deciding whether the cluster undergoes mesonic or baryonic decay. For a mesonic decay a quark-antiquark pair is created from the vacuum and for the baryonic decay a diquark-antidiquark pair is made. Then the exact decay products are chosen and the cluster decays isotropically in the rest frame of the cluster. If there are partons produced in the perturbative phase involved in the decay, they retain their original direction in the cluster rest frame, up to some Gaussian smearing. If the cluster mass is too low to decay into a pair of mesons, it decays into the lightest possible hadron and some energy and momentum is exchanged with the adjacent clusters. At the end we are left with the final state hadrons, some of which might still decay until the end of the simulation if they are very short-lived. []

1.5.3 Jet energy loss

Discovery of jet quenching via leading hadron suppression

First evidence of jet quenching comes from observing high p_T tracks, i.e. the leading hadrons.

Jet quenching in heavy-ion collisions is usually quantized with the nuclear modification factor R_{AA} , which is defined as

$$R_{AA}(p_T) = \frac{(1/N_{AA}^{evt}) dN^{AA}/dp_T}{\langle N_{coll} \rangle (1/N_{pp}^{evt}) dN^{pp}/dp_T} \quad (23)$$

where dN^{AA}/dp_T and dN^{pp}/dp_T are the yields in heavy-ion and proton-proton collisions, respectively and $\langle N_{coll} \rangle$ is the average number of binary nucleon-nucleon collisions in one heavy-ion event. The number of binary collisions can be calculated from the Glauber model as shown in Sec. 1.3.2. From the point of view of direct production a heavy-ion collision can be estimated relatively well to be only a series of proton-proton collisions.

If the medium has no effect on high p_T particles the nuclear modification factor should be 1. At RHIC and LHC this has been observed to be as low as 0.2 because of jet quenching. Measurements of R_{AA} from different sources are shown in Fig. 15

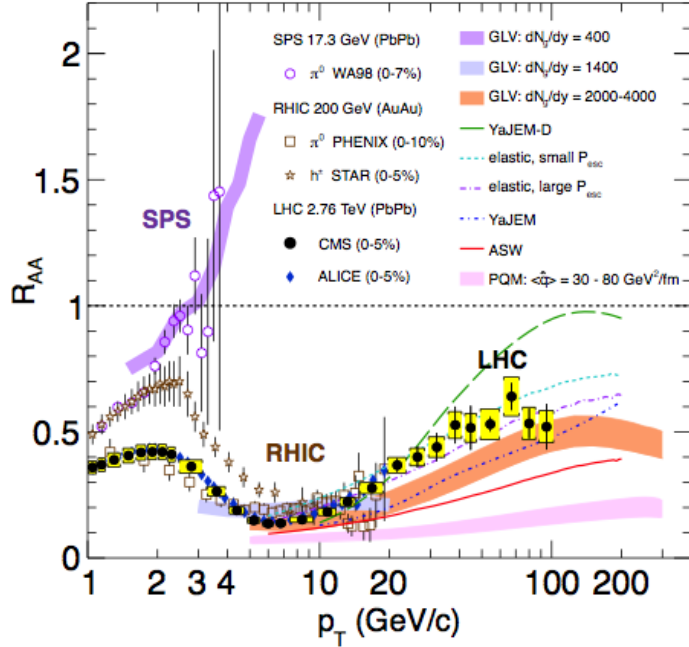


Figure 15: Measurements of the nuclear modification factor R_{AA} in central heavy-ion collisions at three different center-of-mass energies, as a function of p_T , for neutral pions (π^0), charged hadrons (h^\pm), and charged particles [66–70], compared to several theoretical predictions [34, 71–75]. The error bars on the points are the statistical uncertainties, and the yellow boxes around the CMS points are the systematic uncertainties. The bands for several of the theoretical calculations represent their uncertainties [76].

The nuclear modification factor can also be used to quantify anisotropy. In the study of anisotropy R_{AA} in-plane and out-of-plane can be compared. The distance traveled through medium is largest out-of-plane which leads to stronger suppression in this direction. The nuclear modification factor as a function of $\Delta\phi = \phi - \psi_n$ is given by

$$\begin{aligned}
 R_{AA}(\Delta\phi, p_T) &= \frac{(1/N_{AA}^{evt}) d^2 N^{AA}/d\Delta\phi dp_T}{\langle N_{coll} \rangle (1/N_{pp}^{evt}) dN^{pp}/dp_T} \approx \frac{dN^{AA}/dp_T (1 + 2 \cdot v_2 \cos(2\Delta\phi))}{\langle N_{coll} \rangle dN^{pp}/dp_T} \\
 &= R_{AA}^{incl}(p_T) (1 + 2 \cdot v_2 \cos(2\Delta\phi)). \tag{24}
 \end{aligned}$$

741 The yield of proton-proton collisions is independent of the reaction plane and
 742 the yield in heavy-ion collisions is modulated by the second harmonics. In Eq. (24)
 743 R_{AA} is approximated only up to the second harmonics. From Eq. (24) it follows
 744 that

$$\frac{R_{AA}(0, p_T) - R_{AA}(\pi/2, p_T)}{R_{AA}^{incl}(p_T)} \approx \frac{R_{AA}^{incl}(p_T) (1 + 2 \cdot v_2 - (1 - 2 \cdot v_2))}{R_{AA}^{incl}(p_T)} = 4 \cdot v_2 \quad (25)$$

745 The observed $R_{AA}(\Delta\phi, p_T)$ from PHENIX measurements in Au-Au collisions at
 746 $\sqrt{s} = 200\text{GeV}$ [77] is compared to R_{AA} using v_2 via Eq. (24) in Fig. 16. They
 agree very well within the statistical errors for all centrality and p_T bins.

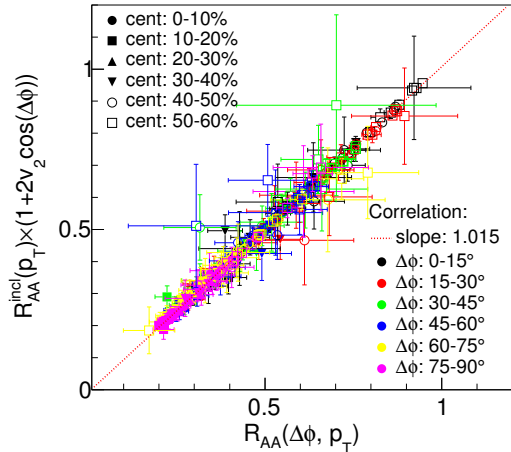


Figure 16: A comparison between observed $R_{AA}(\Delta\phi, p_T)$ and R_{AA} using v_2 from PHENIX measurements of Au-Au collisions at $\sqrt{s} = 200\text{GeV}$. On the X-axis is the measured $R_{AA}(\Delta\phi, p_T)$. On the y-axis is the inclusive R_{AA} multiplied by $1 + 2v_2 \cos(\Delta\phi)$ [77].

747
 748 At high- p_T , the pQCD processes are dominant, hence the v_n (or $R_{AA}(\Delta\phi, p_T)$)
 749 characterize the pathlength-dependence of the energy loss process.

750 Jet quenching is not the only high p_T phenomenon studied in heavy-ion colli-
 751 sions. Another property is jet fragmentation. The high momentum parton created
 752 in the initial collision fragments into a number of partons with smaller p_T . Jet
 753 fragmentation occurs also in proton-proton collisions in the vacuum, but it can
 754 be modified due to the presence of the medium. In order to study the jet frag-
 755 mentation function ($D(z)$, where $z = p_T^h/p_T^{part}$) modification due the medium, we
 756 use the two-particle correlations. The particle yield can be extracted from the

correlation function. The background from the flow processes is correlated and needs to be subtracted to get the particle yield associated only with the jet. The ratio of the jet yields in Au-Au and p-p collision $I_{AA} = Y^{Au+Au}/Y^{p+p}$ characterizes the jet fragmentation modification [78]. I_{AA} probes the interplay between the parton production spectrum, the relative importance of quark-quark, gluon-gluon and quark-gluon final states, and energy loss in the medium.

Theory of jet quenching

High momentum particles are very rare and they are only produced in the initial collisions. After they are created they escape the medium before a thermal equilibrium is reached. Thus they are not part of the pressure-driven collective expansion. Instead high momentum yield is suppressed because of energy loss in the medium. When propagating through the medium these partons lose energy as they pass through the medium. This is referred to as jet quenching. Jet quenching depends on the path lengths through the medium. Thus anisotropy in this region is mainly dependent on the collision geometry and density of medium.

The energy loss of partons in medium is mainly due to QCD bremsstrahlung and to elastic scatterings between the parton and the medium.

The radiative energy loss mechanism is given in terms of the transport coefficient $\langle \hat{q} \rangle$, which describes the average momentum transfer between the medium and parton [79]. The exact definition of this depends on the theoretical formalism used to describe the energy loss mechanism.

Many of the energy loss models exploit the analogy between the QCD interaction of parton propagating through the colored medium and the QED energy loss of electron propagating through material. An electron propagating through matter loses its energy by photon Bremsstrahlung radiation. In the simplest case, each individual scattering center results in a single emission of a photon. This is known as the Bethe-Heitler regime [80]. The energy spectrum of radiated photons dN/dE is, in this case, proportional to $1/E$. However, the Bremsstrahlung photon, can be radiated only when the distance between the scattering centers is larger than the formation length. In the limit, when the scattering centers are closer than the formation length, the Bremsstrahlung process is suppressed. This phenomenon is known as the Landau-Pomeranchuk-Migdal (LPM) [81, 82] suppression. The radiated spectrum in this regime is proportional to $1/\sqrt{E}$.

Lower energy photons are further suppressed by the destructive interference leading to the suppression of Bremsstrahlung photons of $E < \gamma\omega_p$, where ω_p is the plasma frequency of the radiator. This is known as Dielectric suppression. The photon energy distribution in this regime is proportional to the energy of the photon. A schematic view of the effect of these three regimes is shown in Fig. 18.

The simplest energy loss process is elastic QCD scattering off the medium par-

⁷⁹⁶ tons. In elastic scatterings the recoil energy of the scattered partons are absorbed
⁷⁹⁷ by the thermal medium, which reduces the energy of the initial parton. The mean
⁷⁹⁸ energy loss from elastic scatterings can be estimated by

$$\langle \Delta E \rangle_{\text{el}} = \sigma \rho L \langle E \rangle_{\text{scatt}} \propto L, \quad (26)$$

⁷⁹⁹ where σ is the interaction cross section and $\langle E \rangle_{\text{scatt}}$ is the mean energy transfer
⁸⁰⁰ of one individual scattering [84]. This assumption holds if the mean energy is
⁸⁰¹ independent of the total energy of the parton (E). The transport coefficient of
⁸⁰² elastic scattering, $\langle \hat{q}_{\text{el}} \rangle = \langle \Delta E \rangle / L$, is defined as the mean energy los per unit path
⁸⁰³ length.

⁸⁰⁴ Another energy loss mechanism is medium-induced radiation. In QCD this
⁸⁰⁵ radiation is mainly due to the elementary splitting processes, $q \rightarrow qg_r$ and $g \rightarrow gg_r$.
⁸⁰⁶ Assuming that the parton is moving with the speed of light radiation energy loss
⁸⁰⁷ can be estimated by

$$\langle \Delta E \rangle_{\text{rad}} \propto T^3 L^2, \quad (27)$$

⁸⁰⁸ where L is the length of the medium and T is its temperature [85]. The differ-
⁸⁰⁹ ent exponents of L in equations 26 and 27 indicate that radiative energy loss is
⁸¹⁰ dominant over elastic energy loss.

⁸¹¹ There are several models that attempt to describe the nature of the energy loss
⁸¹² mechanism. The most used models can be divided into four formalisms.

⁸¹³ In the Gyulassy-Levai-Vitev (GLV) [86] opacity expansion model the radiative
⁸¹⁴ energy loss is consiered on a few scattering centers N_{scatt} . The radiated gluon
⁸¹⁵ is constructed by pQCD calculation as summing up the relevant scattering am-
⁸¹⁶ plitudes in terms of the number of scatterings. Another approach into opacity
⁸¹⁷ expansion is the ASW model by Armesto, Salgado and Wiedermann [87].

⁸¹⁸ Thermal effective theory formulation by Arnold, Moore and Yaffe (AMY) [88]
⁸¹⁹ uses dynamical scattering centers. It is based on leading order pQCD hard thermal
⁸²⁰ loop effective field theory. This model assumes that because of the high temper-
⁸²¹ ature of the plasma the strong coupling constant can be treated as small. The
⁸²² parton propagating through the medium will lose energy from soft scatterings and
⁸²³ hard scatterings.

⁸²⁴ The above models calculate the energy loss while the parton propagates through
⁸²⁵ the medium, focusing on the pQCD part. The higher twist (HT) approach by Wang
⁸²⁶ and Guo [89] implements the energy loss mechanism in the energy scale evolution
⁸²⁷ of the fragmentation functions.

⁸²⁸ The last category is formed by the Monte Carlo methods. The PYTHIA event
⁸²⁹ generator [90] is widely used in high-energy particle physics. Two Monte Carlo
⁸³⁰ models based on PYTHIA describing the energy loss mechanism are PYQUEN [91]

831 and Q-Pythia [92]. Other Monte Carlo models include JEWEL [93] and Ya-
832 JEM [94].

833 1.5.4 New paradigm of jet Quenching

834 As described in the previous section there have been many experimental evi-
835 dences of jet energy loss, such as the suppression of inclusive hadron spectra at
836 high transverse momentum [?, ?, ?, ?, ?], the modification of back-to-back hadron-
837 hadron [?, 78] and direct photon-jet correlations [?], and the modification of recon-
838 structed jet spectra [?] and jet substructure [?, ?, ?], as compared to the expecta-
839 tions from elementary proton-proton collisions.

840 The first indications of jet quenching, such as R_{AA} , looked essentially at the
841 leading hadrons of jets, the hard part, ignoring the soft scale part of jet phenomena.
842 However, experimental methods have since improved; jet reconstruction algorithms
843 have become reliable in the LHC era. Instead of the leading hadron we can study
844 the entire jet shower.

845 -Jet RAA -Jetscape

846 Thus the new paradigm in jet quenching in heavy-ion collisions involves multi-
847 scale problems [?, 95]. The elementary scattering and the subsequent branching
848 process down to non-perturbative scales are dominated by hard scales in the vac-
849 uum as well as in the medium. Soft scales, of the order of the temperature of
850 the medium, characterise the interactions of soft partons produced in the shower
851 with the QGP. Soft scales also rule hadronisation, which is expected to take place
852 in vacuum for sufficiently energetic probes, even though some modifications can
853 persist from modifications of color flow [?, ?, ?]. Understanding the contributions
854 from the different processes to the jet shower evolution in medium and their scale
855 dependence is crucial to constrain the dynamics of jet energy loss in the expend-
856 ing medium, the role of colour coherence [?], and fundamental medium properties
857 like temperature dependent transport coefficient [?, ?].

858 Lund diagram

859 The different momentum and angular scales are subject to different physical phe-
860 nomena. Figure 19 shows the relevant medium modification phenomena for differ-
861 ent regions of the phase space at time t , when a jet propagates through a thermal
862 cloud of temperature T . As in practice jets propagate over a finite path-length
863 L in QCD matter, Fig. 19 can be taken as a representation of the distribution of
864 partonic jet fragments at moment $t \approx L$, when the jet escapes the medium.

865 The region marked as DGLAP is dominated by the primary vacuum splittings.
866 This region is determined by $\theta > \theta_{\text{vac}}$ with

$$\theta_{\text{vac}} \propto 1/\sqrt{pt}. \quad (28)$$

867 Medium-induced parton branching fills the log p -log- θ -plane from the bottom
 868 up (in p) and from the inside out (in θ). This is because transverse momentum is
 869 acquired by Brownian motion in the medium, $k_\perp^2 \propto \hat{q}t$. Then the formation time
 870 constraint $t \geq p/k_\perp^2 \approx p/\hat{q}t$ implies that medium-induced quanta can be formed in
 871 the region $p \leq k_{\text{form}}$ where

$$k_{\text{form}}(t) = \hat{q}t^2$$

872 .
 873 The probability of finding a splittee with a momentum p with $p < k_{\text{form}}$ is

$$\frac{dP_{\text{find}}(t)}{d \log p} \propto \alpha_s t/t_{\text{form}}(p) \propto \alpha_s \hat{q}^{nicefrac{1}{2}} p^{-1/2} t \quad (29)$$

874 Not all quanta will stay where they were created. Those modes that have time
 875 to lose a significant fraction of their energy will cascade to a significantly lower
 876 scale p . For LPM-type radiation, the splitting that degrades energy the most is
 877 the hardest splitting.

878 The $\log p$ distribution has the same $\frac{1}{\sqrt{p}}$ dependence as in the LPM region

$$\frac{dn}{d \log p} = \frac{1}{p} \frac{d\epsilon}{d \log p} \approx \alpha_s \frac{\sqrt{\hat{q}t}}{\sqrt{p}} \quad (30)$$

879 Also the quanta originating from the DGLAP region will undergo medium
 880 interactions that will make the quanta radiate and split. The distribution of radi-
 881 ation is the same as from any other mode. Above a certain momentum scale k_{split}
 882 the distribution of originating daughters is

$$\frac{dP_{\text{find}}}{d \log p d \log \theta} \approx \alpha_s \frac{t}{t_{\text{split}}(p)}, \quad (31)$$

883 Note that the ratio t/t_{split} is smaller than 1 for nodes above k_{split} and therefore
 884 the number of daughters is smaller than the number of vacuum splitted quanta.
 885 Below k_{split} the cascade is similar to the medium cascade and the number of quanta
 886 become

$$\frac{dn}{d \log p d \log \theta} \approx \alpha_s \frac{t}{t_{\text{split}}(p)}, \text{ for } p < k_{\text{split}}(p) \quad (32)$$

887 The angular distribution is driven by two mechanisms; Multiple soft scatterings
 888 give rise to transverse Brownian motion, which determines the distribution at small
 889 angles. The typical angle reached in the LPM region is

$$\theta_{\text{BR}}(p) \approx \frac{\sqrt{\hat{q}t}}{p}, \text{ for } k_{\text{form}} > p > k_{\text{split}}, \quad (33)$$

890 while in the medium cascade region of the phase space this becomes

$$\theta_{\text{BR}}(p) \approx \left(\frac{T}{p}\right)^{\frac{3}{4}} \quad (34)$$

891 Large angular scales cannot be reached by Brownian motion, but can arise from
892 rare large angle scatterings, described by Molière [].

893 1.6 QGP in Small systems

894 After the existence of QGP in heavy ion collisions has been established, attention
895 has been turned to small systems. Proton-proton (pp) and proton-Lead (pPb)
896 collisions have been studied at LHC and RHIC has studied a host of different
897 collision systems; namely proton-Gold (pAu), deuteron-Gold (dAu) and Helium³-
898 Gold (He³Au) collisions starting in 2000.

899 Already before the era of modern colliders, collective behaviour in proton-
900 proton collisions was considered by names like Heisenberg, Fermi and Bjorken. [96]
901 Eventually there were some experimental searches of QGP in pp and $p\bar{p}$ collisions
902 in E735 at Tevatron [97] and MiniMAX [98]. However no conclusive evidence was
903 found.

904 In the early years of RHIC these small systems were mostly considered as con-
905 trol measurement, for example in constraining nuclear modified parton distribution
906 functions (nPDFs) that determine the initial gluon distributions that determine
907 the first epoch of heavy ion collisions [99, 100].

908 In 2010 ultrahigh-multiplicity pp collisions were studied at CMS. The study
909 found that particles had a weak but clear preference to be emitted along a com-
910 mon transverse ϕ angle across all rapidities [101]. This seemed like behaviour
911 were similar to AA collisions, but it was argued that it could as well come from
912 momentum correlations present in the earliest moments of the collision.

913 In 2012 LHC ran its first pPb data taking period. Around the same time
914 dAu data was reexamined at RHIC. Now it was revealed that most of the flow
915 signatures attributed to hydrodynamic expansion in AA collisions also existed in
916 smaller systems.

917 -Sub nucleonic structure needed to describe intial conditions in pA, pp

918 1.6.1 Collective phenomena

919 The most rugged analysis of collective behaviour concerns the two (or more) parti-
920 cle correlations, often parametrised via the relative azimuthal angle and pseudora-

pidity differences, $\Delta\phi$ and $\Delta\eta$ respectively. Figure 21 shows two-particle correlations measurements in PbPb, pPb and pp collisions at the LHC. In PbPb collisions long-range correlations dominate over short-range phenomena. This shows in the two ridges at $\Delta\phi = 0$ and $\Delta\phi = \pi$. At $\Delta\phi \approx \Delta\eta \approx 0$, there is a peak coming from single jet fragmentation. Since the away-side jet can be spread out in $\Delta\eta$, this contribution disappears when compared to the flow contribution at the away side ridge. In pPb, and pp the near side peak is more distinguished and the away-side jet contribution starts to show. Still, one can see long-range correlations that seem like flow-like collective behaviour in both systems.

In addition to the two particle correlations, correlations have been observed in the form of v_n coefficients both at LHC and at RHIC. The results have also been described with hydrodynamical models, although the applicability of said models is questionable, because of the large Reynolds numbers in small systems. Figure 20 shows results for v_2 in different collisions systems at RHIC as measured by PHENIX. These different systems provide also different initial geometries. dAu collisions naturally have an ellipsoidal form, while a He3 collision has a triangular form and thus produces larger triangular flow, v_3 components.

Other observations that produce flow-like results include mass ordered v_2 coefficients and higher order harmonics coming from fluctuations in the initial geometry. Thus all the major collective flow phenomena observed in heavy-ion collisions have been also identified in small systems.

One open question is identifying the point where flow-like correlations end. The question has proved challenging since low multiplicity events are dominated by non-flow phenomena. This makes observations in low multiplicity events model/method dependant. Different methods assess non-flow contributions differently. Thus some methods fail to observe a signal in cases, where others do and it is unclear whether this is true collective motion or it comes from non-flow contributions.

1.6.2 Absence of jet quenching

In A+A collisions, an important confirmation of the standard model comes from the energy loss of high p_T partons traversing the medium, referred to as jet quenching [102–104]. In 2003 the jet quenching effect was observed to disappear in d+Au collisions. This was taken as an indication that no QGP was created. Similarly at LHC no jet modification has been observed in pPb collisions. Fig. 22 shows the nuclear modification factor R_{pA} in pPb collisions as measured at the LHC.

The lack of jet modification seems surprising considering the multitude of flow observations supporting the existence of QGP in small systems. One possible explanation is simply the size of medium. In PbPb collision partons traversing through the medium lose energy to the medium. If the medium is very small there

960 is limited time for interaction with the medium.

961 Calculations indicate that there should be modification in the most central
962 pPb collisions, but selecting these in the analysis is complicated. In PbPb colli-
963 sions most of the particle production comes from the medium and thus the total
964 multiplicity is a good indicator of centrality. In pPb collisions, however the total
965 multiplicity is smaller and is more strongly influenced by jet phenomena. Events
966 with jets have naturally larger multiplicities and are more likely to be classified as
967 central events.

968 So far the only observable indicative of jet quenching in pPb collisions is the
969 high $p_T v_2$. In heavy-ion collisions this is not explained by hydrodynamics. Instead
970 it is assumed to come from jet quenching with different path lengths through the
971 medium in different directions. In Fig.22 ATLAS and CMS measurements of v_2 in
972 pPb and PbPb collisions are shown. The pPb results seem to follow a very similar
973 pattern. But

Table 1: Summary of observations in small system

| Observable | PbPb | pPb | pp |
|---------------------------|------------|-----------------|----------|
| Jet RpA/RAA | Modified | No modification | - |
| Hadron RpA/RAA | Modified | No modification | - |
| Heavy flavors | | | |
| Jet shape | Broadening | No observations | - |
| Two-particle correlations | Ridge | Ridge | Ridge |
| v_2 | Observed | Observed | Observed |
| Mass ordered flow | | | |
| Higher ordered harmonics | | | |
| High $p_T v_2$ | Observed | Maybe | - |

974 1.6.3 Centrality determination in small systems

975 In lead-lead collisions the total multiplicity of the event is a good indicator of the
976 centrality of the collision. In proton-lead collisions the connection of multiplicity
977 and centrality is less clear. In p–Pb collisions the impact parameter is only
978 loosely correlated to N_{part} or N_{coll} . Hence, although one uses traditionally the
979 term centrality to refer to these measurements, the relevant parameters are N_{part}
980 and N_{coll} [1].

981 The Glauber model [?] is generally used to calculate geometrical quantities of
982 nuclear collisions (A–A or p–A). In this model, the impact parameter b controls the
983 average number of participating nucleons N_{part} and the corresponding number of
984 collisions N_{coll} . It is expected that variations of the amount of matter overlapping

985 in the collision region will change the number of produced particles, and parameters
986 such as N_{part} and N_{coll} have traditionally been used to describe those changes
987 quantitatively, and to relate them to ppcollisions.

988 The problem in p–Pb collisions, is that fluctuations in multiplicity coming from
989 for example hard scatterings are of the same order as the differences in multiplicity
990 between centrality classes. In Pb–Pb collisions these multiplicity fluctuations have
991 little influence on the centrality determination, the range of N_{part} or N_{coll} is large
992 and $P(M|v)$ converges quickly to a Gaussian with a small width relative to the
993 range of v .

994 Thus in practice selecting high multiplicity one chooses not only large average
995 N_{part} , but also positive multiplicity fluctuations leading to deviations from the
996 binary scaling of hard processes. These fluctuations are partly related to qualita-
997 tively different types of collisions. High multiplicity nucleon-nucleon collisions
998 show a significantly higher particle mean transverse momentum. They can be
999 understood as harder collisions with larger momentum transfer Q^2 or as nucleon-
1000 nucleon collisions where multiple parton-parton interactions (MPI) take place.
1001 This is illustrated in Fig. 24.

1002 Of particular interest are estimators from kinematic regions that are causally
1003 disconnected after the collision. The measurement of a finite correlation between
1004 them unambiguously establishes their connection to the common collision ge-
1005 ometry. Typically these studies are performed with observables from well sep-
1006 arated pseudorapidity (η) intervals, e.g. at zero-degree (spectators, slow-nucleons,
1007 deuteron break-up probability) and multiplicity in the rapidity plateau.

1008 One centrality selection that is argued not to induce a bias on the binary scaling
1009 of hard processes is provided by the energy measurement with the Zero Degree
1010 Calorimeters (ZDC) in ALICE, due to their large η -separation from the central
1011 barrel detectors. They detect the "slow" nucleons produced in the interaction by
1012 nuclear de-excitation processes or knocked out by wounded nucleons.

1013 Additional kinematic biases exist for events containing high- p_{T} particles, which
1014 arise from the fragmentation of partons produced in parton-parton scattering with
1015 large momentum transfer. Their contribution to the overall multiplicity increases
1016 with increasing parton energy and thus can introduce a trivial correlation between
1017 the centrality estimator and the presence of a high- p_{T} particle in the event. For the
1018 very peripheral collisions, the multiplicity range that governs the centrality for the
1019 bulk of soft collisions can represent an effective veto on hard processes. For the
1020 nuclear modification factor this would lead to $R_{\text{pPb}} < 1$.

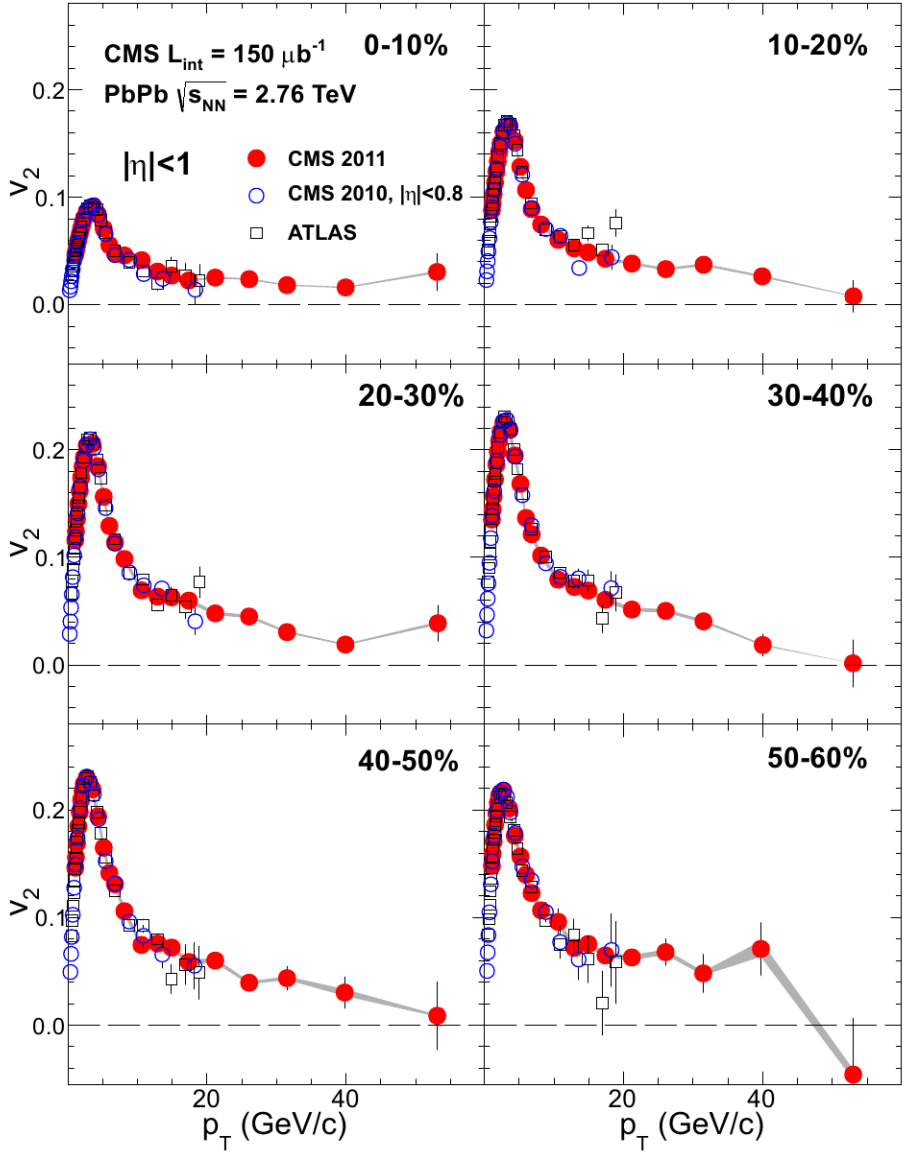


Figure 17: Elliptic flow, v_2 , as a function of the charged particle transverse momentum from 1 to 60 GeV/c with $|\eta| < 1$ for six centrality ranges in Pb-Pb collisions at $\sqrt{s_{NN}} = 2.76 \text{ TeV}$, measured by the CMS experiment. [61].

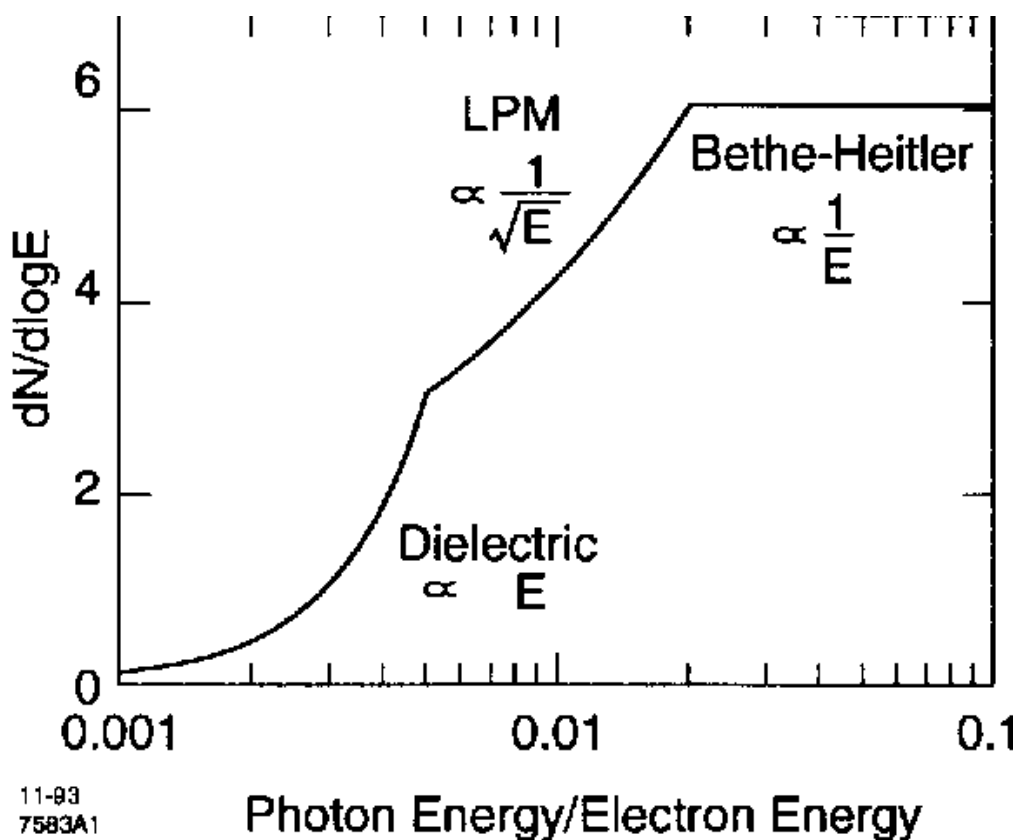


Figure 18: The expected bremsstrahlung spectrum for a electron propagating through material. [83].

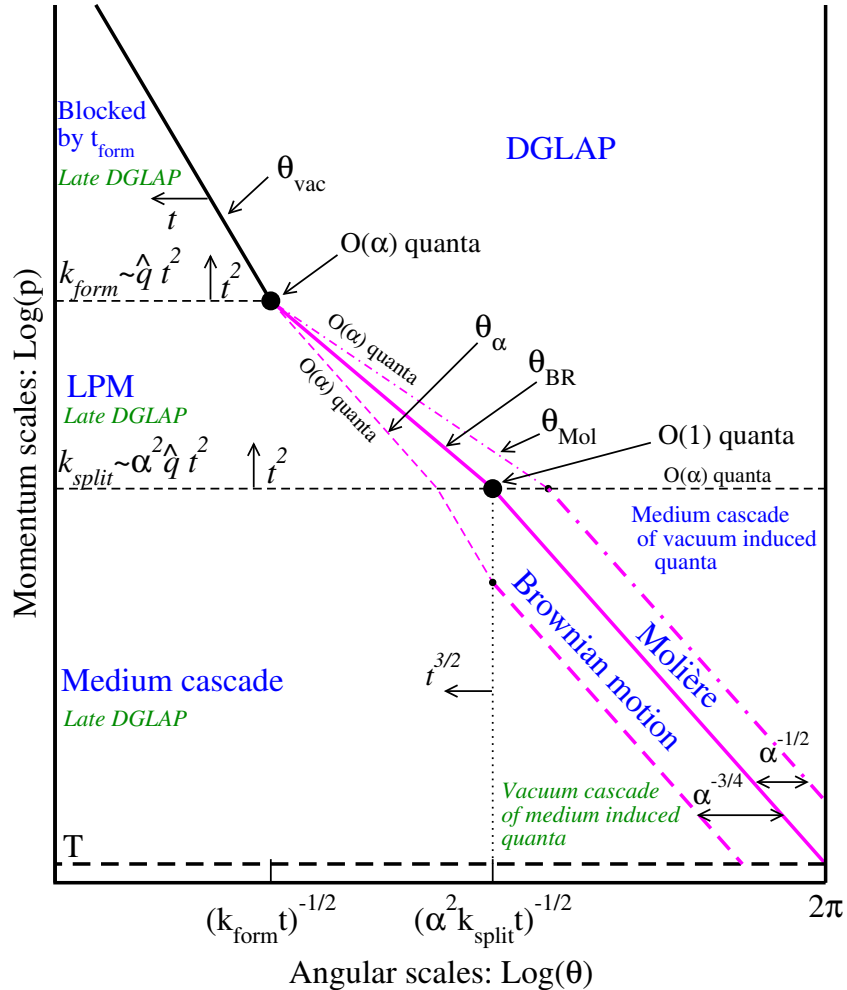


Figure 19: Parametrically accurate picture of how a medium-modified parton cascade fills the phase space. At time t , quanta can be formed up to momentum scale k_{form} and they are formed with $O(1)$ probability per $\log p$ at lower scale k_{split} . Quanta below k_{split} split further and their energy cascades to the thermal scale T in less than an epoch t . Transverse Brownian motion moves quanta up to the angle $\theta_{\text{BR}}(p)$ denoted by the thick purple line. The Molière region at larger θ is dominated by rare large angle scattering. At even larger angle, there are $O(\alpha_s)$ quanta per double logarithmic phase space from DGLAP ‘vacuum’ radiation, and for momenta below k_{split} these cascade within time t to T . After the jet escapes the medium, the jet and the emitted fragments will undergo vacuum radiation. This late time vacuum radiation emitted by the original parton dominates at sufficiently small $\log \theta$ (regions marked “late DGLAP” and bounded by θ_{vac} and θ_α), whereas the late time radiation of the fragments dominates in the region denoted by “Vacuum cascade of the medium induced quanta”. [95].

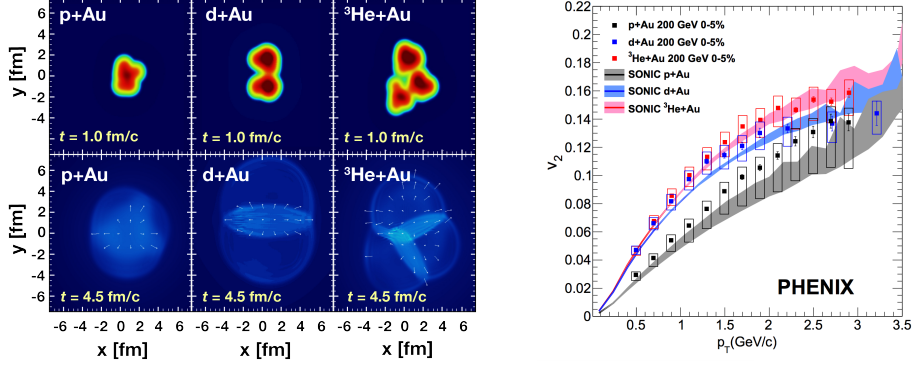


Figure 20: Calculations of the intial energy density in small collision systems at RHIC and the resulting hydrodynamic evolution.

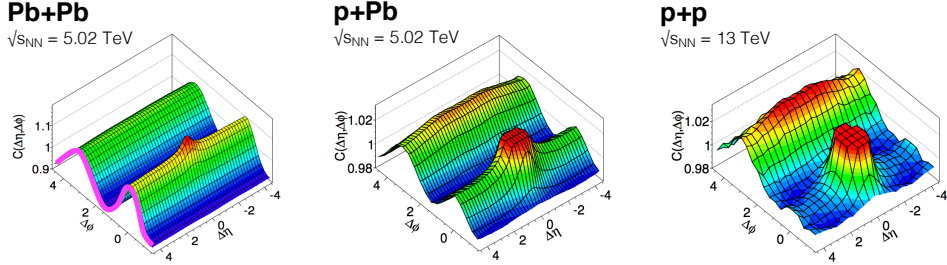


Figure 21: Two-particle correlation results in PbPb , pPb , and pp collisions at the LHC [1].

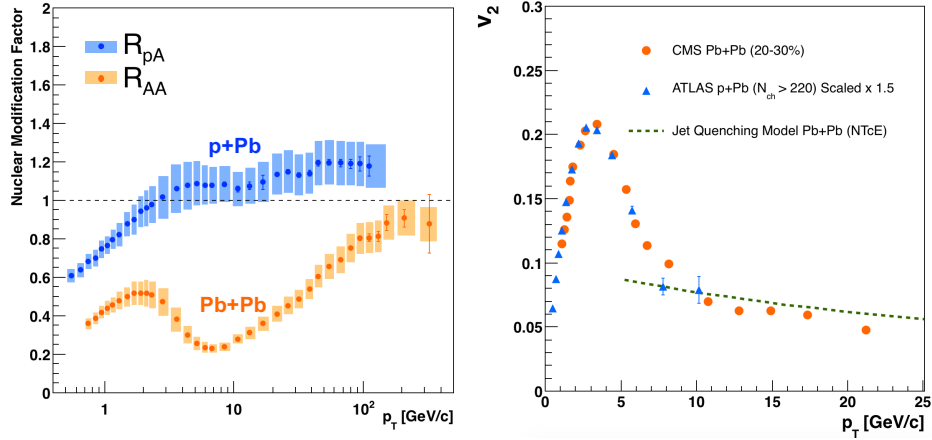


Figure 22: R_{pA} in proton-lead collisions

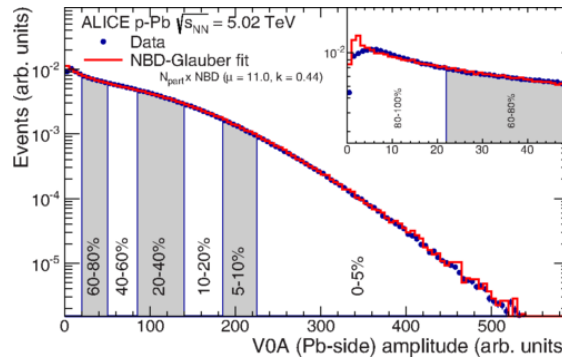


Figure 23: Distribution of the sum of amplitudes in the V0A hodoscopes (Pb-going), as well as the NBD-Glauber fit (explained in the text). Centrality classes are indicated by vertical lines. The inset shows a zoom-in on the most peripheral events. [1]

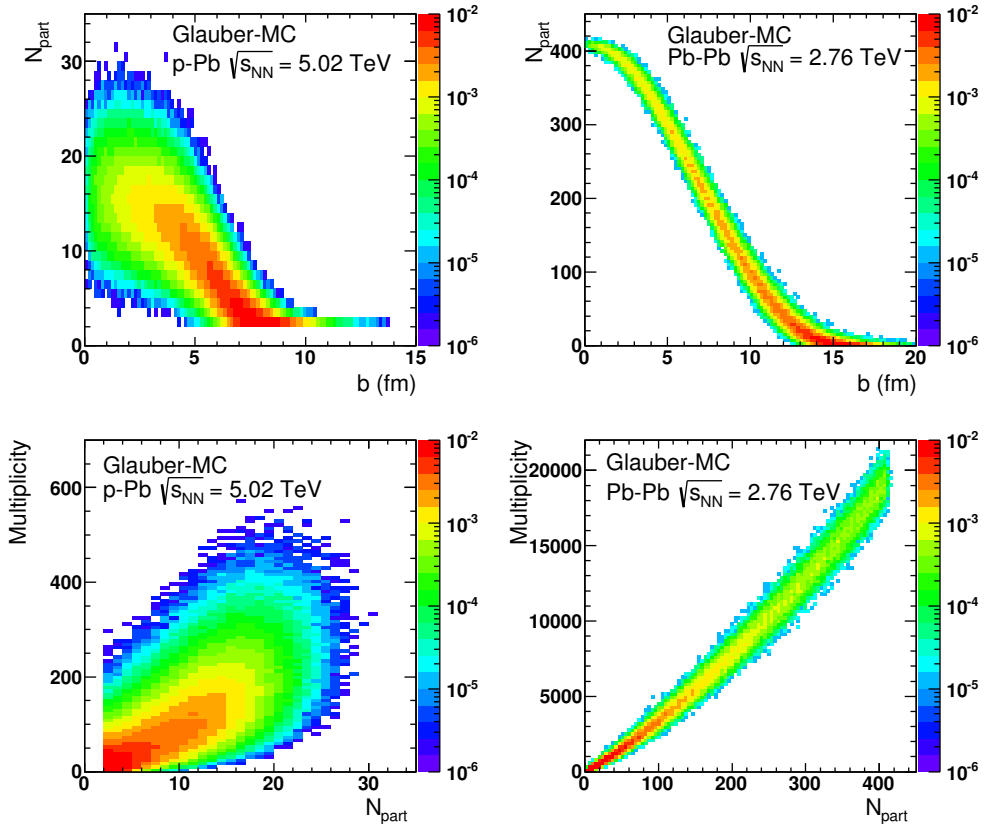


Figure 24: Top: Scatter plot of number of participating nucleons versus impact parameter; Bottom: Scatter plot of multiplicity versus the number of participating nucleons from the Glauber fit for V0A. The quantities are calculated with a Glauber Monte Carlo of p-Pb (left) and Pb-Pb (right) collisions. [1]

1021 2 Experimental Details

1022 2.1 CERN

1023 The European Organization for Nuclear Research (CERN) is the largest particle
1024 physics laboratory in the world. CERN was founded in 1954. In 2019 CERN
1025 consists of 22 member states. Additionally CERN has contacts with a number
1026 of associate member states and various individual institutions. Some 12000 vis-
1027 iting scientists from over 600 institutions in over 70 countries come to CERN for
1028 their research. CERN itself is located near Geneva at the border of France and
1029 Switzerland and itself employs about 2500 people.

1030 The laboratory includes a series of accelerators, which are used to accelerate
1031 the particle beams used. A schematic view of the complex as of 2019 is shown
1032 in Figure ???. In the framework of this thesis the main component is the Large
1033 Hadron Collider (LHC), the largest collider at CERN. LHC will be discussed in
1034 the chapter in more detail. Other accelerators in the series are used to inject the
1035 particle beam into LHC, but they are also used in itself for various experimental
1036 studies.

1037 The second largest accelerator is the super proton synchrotron (SPS). It is final
1038 step before the particle beam is injected into LHC. Commissioned in 1976, it was
1039 the largest accelerator at CERN until the the Large Electron-Positron Collider
1040 (LEP) was finished in 1989. Originally it was used as a proton-antiproton collider
1041 and as such provided the data for the UA1 and UA2 experiments, which resulted in
1042 the discovery of the W and Z bosons. At the moment there are several fixed target
1043 experiments utilising the beam from SPS. These study the structure (COMPASS)
1044 and properties (NA61/SHINE) of hadrons, rare decays of kaons (NA62) and radi-
1045 ation processes in strong electromagnetic fields (NA63). Additionally the AWAKE
1046 and UA9 experiments are used for accelerator research and development.

1047 -PS

1048 2.2 Large Hadron Collider

1049 The Large Hadron Collider (LHC) is the largest accelerator at CERN and the
1050 largest particle collider ever built. The LHC is designed to accelerate protons
1051 up to an energy of 8 TeV and lead ions up to 2.76 TeV per nucleon [?]. The design
1052 luminosity of the LHC is $10^{34} \text{ cm}^{-2} \text{s}^{-1}$. In 20xx it achieved a record peak luminosity
1053 of xxx. For lead beams the design luminosity is xxx. All this is achieved with a
1054 ring of 26.7 km, that consists of 1232 superconducting dipole magnets that keep
1055 particles in orbit.

1056 The particles are accelerated through the use of radio-frequency (RF) cavities.
1057 The RF are build such that the electromagnetic waves become resonant and build

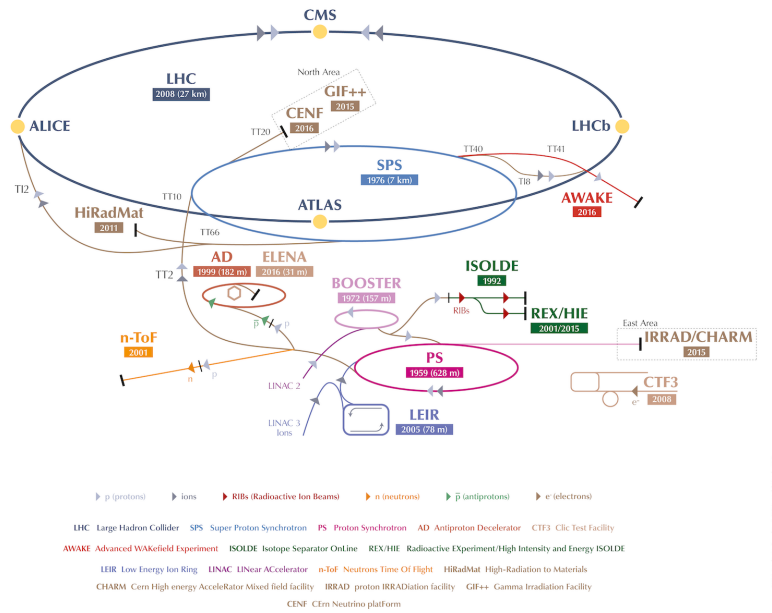


Figure 25: A schematic view of the accelerator complex at CERN. Before particles can be injected into the LHC they require a series of preliminary? acceletarors. Until 2018 protons start their journey in LINAC2 (Linear Accelerator) and continue through the Booster, Proton Synchrotron (PS) and Super Proton Synchrotron (SPS). Between 2019 and 2020 LINAC2 will be replaced by LINAC4 [105]

1058 up inside the cavity. Charges passing through the cavity feel the overall force
1059 and are pushed forward along the accelerator. As they consist of electromagnetic
1060 waves, the field in the RF cavity oscillates. Thus particles must enter the cavity at
1061 the correct phase of oscillation to receive a forward push. When timed correctly,
1062 the particles will feel zero accelerating voltage when they have exactly the correct
1063 energy. Particles with higher energies will be decelerated and particles with lower
1064 energies will be accelerated. This focuses particles in distinct bunches. The RF
1065 oscillation frequency at the LHC is 400.8 MHz. Thus RF "buckets" are separated
1066 by 2.5 ns. However only 10 % are actually filled with particles, so the bunch
1067 spacing in the LHC is 25 ns, at a bunch frequency of 40 MHz.

1068 With 7 TeV proton beams the dipole magnets used to bend the beam must
1069 produce a magnetic field of 8.33 T. This can be only achieved through making
1070 the magnets superconducting, which requires cooling them down with helium to a
1071 temperature of 1.9 K. The 1232 dipole magnets make up roughly 2/3 of the LHC
1072 circumference. The remaining part is made up of RF cavities, various sensors and
1073 higher multipole magnets used to keep the beam focused. The most notable of
1074 these are the 392 quadrupole magnets.

1075 The LHC is divided into octants, where each octant has a distinct function.
1076 Octants 2 and 8 are used to inject beam into the LHC from SPS. The 2 beams
1077 are crossed in octants 1,2,5 and 8. The main experiments are built around these
1078 crossing points. Octants 3 and 7 are used for beam cleansing. This is achieved
1079 through collimators that scatter particles with too high momentum or position
1080 offsets off from the beam. The RF cavities used for acceleration are located in
1081 octant 4 and octant 6 is used for dumping the beam. The beam dump is made
1082 up of two iron septum magnets, one for each beam, that will kick the beam away
1083 from machine components into an absorber when needed.

1084 2.2.1 LHC experiments

1085 As of 2018 there are four main experiments at the LHC; ALICE, ATLAS, CMS
1086 and LHCb and three smaller ones LHCf, TOTEM and MoEDAL. ALICE will be
1087 covered in section 2.3.

1088 ATLAS (A Toroidal LHC ApparatuS) and CMS (Compact Muon Solenoid) are
1089 the two largest experiments at the LHC. They are both multipurpose experiments
1090 designed to be sensitive to many different possible new physics signals. The biggest
1091 discovery made by these so far is the discovery of the Standard Model Higgs boson,
1092 which was simultaneously published by the experiments in 2012 [?,?].

1093 The LHCb (LHC beauty) experiment [?] is made for studying the bottom
1094 (beauty) quark. Main physics goals include measurement of the parameters of CP
1095 violation with decays of hadron containing the bottom quark. One of the most
1096 important results published by LHCb is the first measurement of $B_s^0 \rightarrow \mu^+ \mu^-$

1097 decay, which was found to be in line with the Standard Model.

1098 In addition to the four large experiments there are three smaller experiments
1099 along the LHC ring. LHCf (LHC forward) is located at interaction point 1 with
1100 ATLAS. It aims to simulate cosmic rays by the particles thrown forwards by the
1101 collisions in ATLAS.

1102 TOTEM (TOTal Elastic and diffractive cross section Measurement) is located
1103 near the CMS experiment at point 5. This allows it to measure particles emerging
1104 from CMS with small angles. The main goals is to measure the total, elastic and
1105 inelastic cross-sections in pp collisions [?].

1106 The MoEDAL (Monopole and Exotics Detector At the LHC) experiment is
1107 located at the interaction point 8 together with the LHCb experiment. MoEDAL
1108 tries to measure signatures of hypothetical particles with magnetic charge, mag-
1109 netic monopoles.

1110 2.3 ALICE

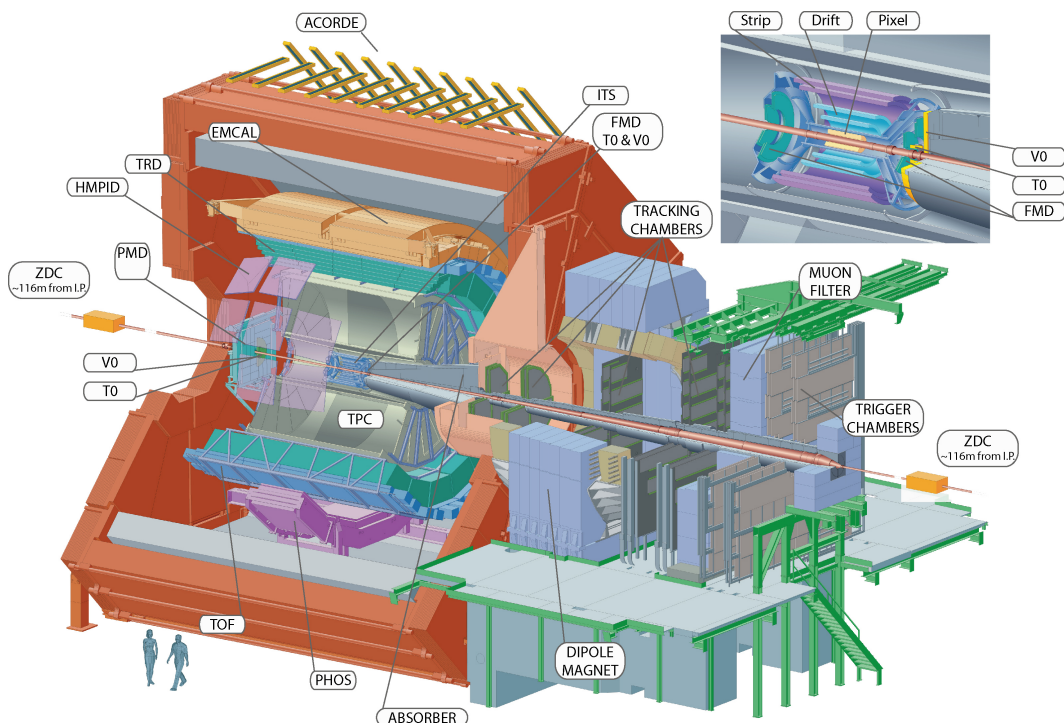


Figure 26: Schematic view of ALICE

1111 ALICE (A Large Ion Collider Experiment) [106] is the dedicated heavy ion
1112 experiment at the LHC. ALICE was designed to cope with the expected very high
1113 multiplicity environment of heavy ion collisions. The design allows measurement

of a large number of low momentum tracks. The different detector subsystems are optimised to provide high momentum resolution and excellent particle identification capabilities over a broad range of momentum.

A schematic view of the ALICE detector in 2018 is presented in Figure 26. This section will go through the composition of ALICE as it has been during run 2 between 2014 and 2018. The detector will go through significant upgrades during Long Shutdown 2 in 2019-2020. As in all the major high energy physics experiments the positioning of the detectors follows a layered structure. Closest to the interaction point are the tracking detectors. The main task of these detectors is to locate the position of the primary interaction vertex accurately and to record the tracks of charged particles. To achieve this they need a very good spatial resolution close to the interaction point. Tracking detectors do not significantly alter the tracks of traversing particles. Thus they can be located in the innermost layers.

Calorimeters are designed to stop any particles hitting them and use the absorption to measure the energy of the particles. Thus they must be located behind the tracking detectors. ALICE has two separate calorimeter systems, the electromagnetic calorimeters measure mainly electrons and photons, while the muon detection system measures muons.

2.3.1 Tracking

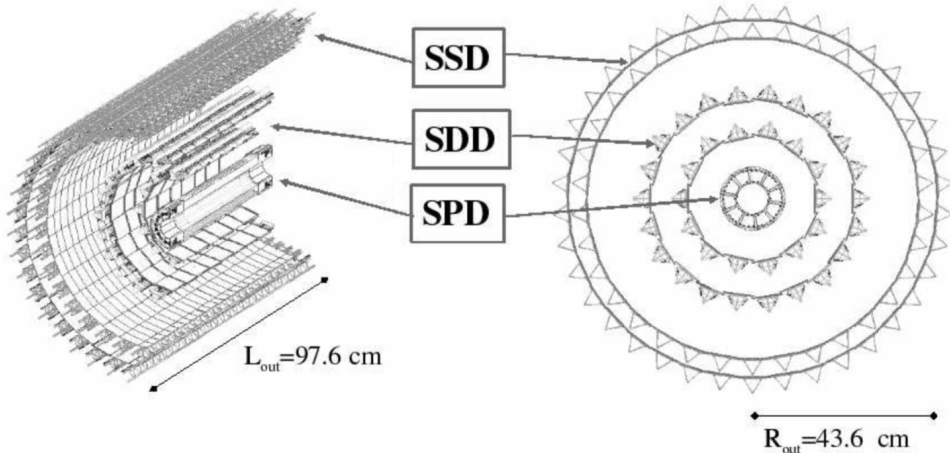


Figure 27: Schematic view of ALICE Inner Tracking System

The main design guideline for the tracking detectors in ALICE was the requirement to have good track separation and high granularity in the high multiplicity environment of heavy ion collisions. Before LHC was built the wildest estimates

1137 put the particle density at 8000 charged particles per unit of rapidity].. In real-
1138 ity the particle density turned out to be significantly smaller, about 1600 charged
1139 particles per rapidity unit.]

1140 The main tracking detector in ALICE is the Time Projection Chamber (TPC),
1141 discussed in more detail in section 2.3.2

1142 Between TPC and the beam pipe there is an array of six layers of silicon detec-
1143 tors, called the inner tracking system (ITS) [?]. The main tasks of the ITS are to
1144 locate the primary vertex with a resolution better than $100\ \mu m$, to reconstruct the
1145 secondary vertices from decaying particles, to track and identify particles with mo-
1146 mента below 200 MeV and to compliment the momentum and angle measurements
1147 of TPC. During long shutdown 2 in 2019-2020 the entire ITS will be replaced [?].
1148 As of 2018 the two innermost layers are made of the silicon pixel detector (SPD).
1149 As it's the closest detector to the interaction point it requires are very high spatial
1150 resolution. Thus the choice of pixel technology is natural. In heavy ion collisions
1151 the particle density is around 50 particles per cm^2 .

1152 The next two layers are the silicon drift detector (SDD), which is made out of
1153 homogeneous neutron transmutation doped silicon. It is ionized when a charged
1154 particle goes through the material. The generated charge then drifts to the col-
1155 lection anodes, where it is measured. The maximum drift time in SDD is about 5
1156 μs This design gives very good multitrack capabilities and provides two out of the
1157 four dE/dx samples in the ITS.

1158 The two remaining layers in the ITS are the silicon strip detector (SSD). The
1159 strips work in a similar way as silicon pixels, but by itself one layer only provides
1160 good resolution in one direction. Combining two crossing grids of strips provides 2
1161 dimensional detection. Each charged particle will hit two intervening strips. The
1162 position of the hit can be deduced from the place where the strips cross each other.

1163 2.3.2 TPC

1164 Time projection chamber (TPC) is a cylindrical detector filled with $88m^3$ of
1165 Ne – CO₂ (90/10 %) gas mixture. The gas is contained in a field cage that provides
1166 an uniform electric field of $400V/cm$ along the z-axis (along the beam direction).
1167 Charged particles traversing through the TPC volume will ionise the gas along
1168 their path. This liberates electors that drift towards the end plates of the cylin-
1169 der.

1170 The field cage is separated into two detection volumes by the central high
1171 voltage electrode. Both sides have a drift length of 2.5 m and inner/outer diameters
1172 of 1.2/5 m. This means the central electrode must provide a maximum potential
1173 of 100 kV to achieve the design field magnitude. The maximum time required for
1174 electrons to drift through the chamber is about 90 μs .

1175 When electrons reach the end of the main cylinder they enter the readout

1176 chambers. The readout section of both sides consists of 18 outer chambers and
1177 18 inner chambers. Each of them are made of multiwire proportional chambers
1178 with cathode pad readout. This design is used in many TPCs before. During
1179 Long Shutdown 2 in 2019-2020, the multiwire chambers will be replaced by Gas
1180 Electron Multipliers (GEMs, see section 2.3.3).

1181 The relatively slow drift time of $90 \mu\text{s}$ is the limiting factor for the luminosity
1182 ALICE can take. The occupancy of the TPC must be kept in a manageable level.

1183 **2.3.3 TPC upgrade**

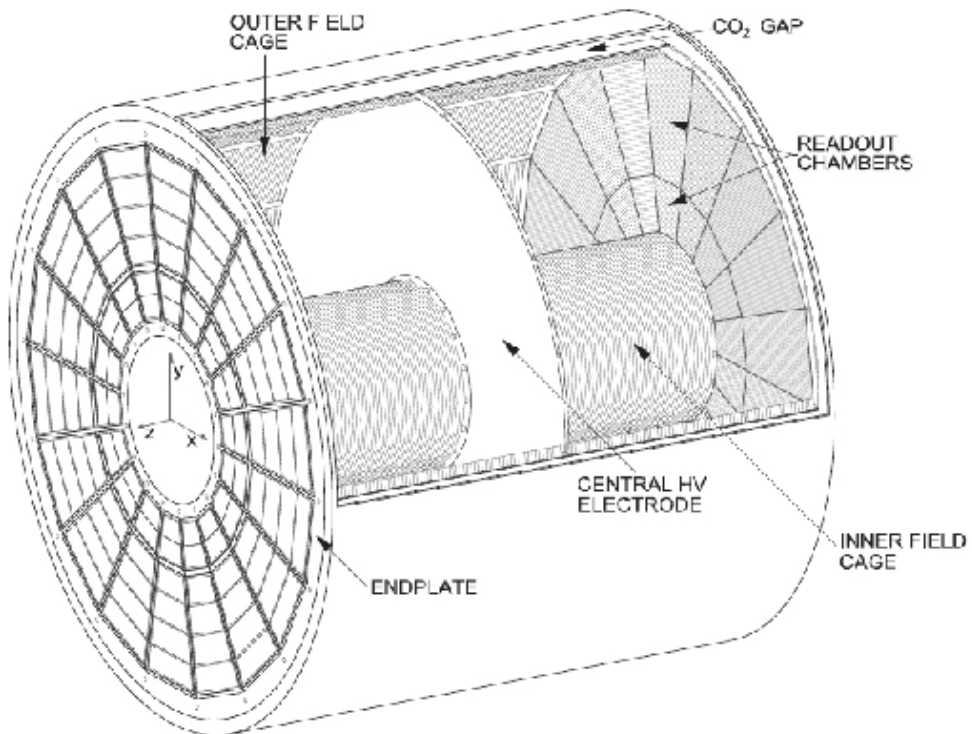


Figure 28: Schematic view of ALICE Time Projection Chamber

1184 During long shutdown 2 in 2019-2020 ALICE will go through significant modi-
1185 fications. The goal is to be able have continuous readout [?] in heavy ion collisions
1186 at an interaction rate of 50 kHz. I have made a personal contribution to the quality
1187 assurance of the new GEM readout of TPC.

1188 ALICE will add a new Forward Interaction trigger (FIT) to replace the V0 and
1189 T0 detectors.

1190 Additionally the current inner tracking system (ITS) will be completely re-
1191 placed. The current layered structure with three different technologies will be
1192 replaced by an all pixel detector with significantly reduced pixel size. Additionally
1193 the first layer will be brought closer to the beam pipe. The new ITS will have
1194 better tracking efficiency and better impact parameter resolution.

1195 The muon detection will be complimented by the Muon Forward Tracker (MFT) [?].
1196 Based on the same technology as the new ITS, MFT will be placed before the
1197 hadron absorber that sits in front of the existing muon spectrometer. MFT should
1198 significantly increase the signal/background ratio in heavy quark measurements.

1199 Many subdetectors will make small improvements to enhance the readout rate.
1200 The central trigger processor will be replaced and ALICE will introduce a new
1201 framework O^2 that combines both online data acquisition and offline analysis.

1202 The detector restricting the readout the most at the moment is the TPC. The
1203 current wire chamber based system limits the readout rate to 3.5 kHz. To achieve
1204 the 50 kHz readout rate goal the wire chambers will be replaced by a Gas Electron
1205 Multiplier (GEM) based system.

1206 TPC has a total of 36 inner and 36 outer readout chambers. Each of these will
1207 consist of 4 layers of GEM foils. The inner chambers will only have one foil for
1208 each layer. The outer chambers are separated into three sections, each with its
1209 own layer of foils. Each gem foil is made up of a 50 μm thick resistive capton layer,
1210 coated on both sides by 5 μm thick layers of copper. Each foils is separated into a
1211 number (20-24) of distinct active areas. The active areas are pierced quite densely,
1212 they have 50-100 holes in the area of a single mm^2 . The density of holes changes
1213 from layer to layer. The two middle layers of foils have a larger (double) pitch
1214 (smaller hole density) while the top and bottom layers have a smaller (normal)
1215 pitch (larger hole density).

1216 The holes have a conical shape which they acquire during a two step chemical
1217 etching process.

1218 The working principle of these foils is based on electrodynamics. **elaborate** There
1219 is a large potential difference (140-400 V) applied to the two sides of the foil, which
1220 results in large field in each hole. This acts both as a lens and an amplifier for
1221 the electrons. The amplification happens inside the holes where the field is the
1222 strongest.

1223 As opposed to wire chambers, which typically have one voltage setting, a GEM-
1224 based detector requires several independent voltage settings: there is a drift voltage
1225 which drives the electrons from the ionisation point to the GEM, an amplification
1226 voltage, and an extraction voltage that brings electrons from the GEM exit to the
1227 readout plane.

1228 The GEMs are designed to minimise ion backflow to allow continuous, ungated
1229 and untriggered readout.

1230 The purpose of the multilayered structure is to reduce the ion backflow []; not
1231 only one layer of GEM foils will be installed, but a 4 layer stack. In the stack there
1232 are 2 standard pitch GEM foils, where the pitch size, i.e. the separation of the
1233 holes inside a foil is around $140 \mu\text{m}$, and 2 large pitch GEM foils, there the hole
1234 spacing is two times larger, $280 \mu\text{m}$. The two outer layers will have standard pitch
1235 and the two middle layers have large pitch. The middle layers with large pitch
1236 serve as extra insulator against the ion backflow. Additionally the setup allows
1237 operating individual GEM foils at lower voltages and still have an increase in the
1238 gain of a few orders of magnitude.

1239 [107]

1240 Quality Assurance of the GEM foils

1241 The GEM foils are produced at CERN, where they will undergo a basic QA (QA-B)
1242 procedure, that includes

- 1243 • Coarse optical inspection to see any major defects, holes, cuts and dis-
1244 coloured regions
- 1245 • Short-term leakage current measurement

1246 Any problems found in the basic inspection are documented for later cross-
1247 checking.

1248 The advanced quality assurance (QA-A) is performed in two centers, one in
1249 the Helsinki Institute of Physics (HIP) and one in the Wigner Research Centre in
1250 Budapest. The QA-A procedure includes the following measurements

- 1251 • Long-term leakage current measurement
- 1252 • High-resolution optical scanning
- 1253 • Gain uniformity check (In Budapest)

1254 In the procedure foils are classified according to a traffic light system. Red
1255 means the foil didn't pass the basic selection criteria and thus cannot be used.
1256 Yellow means it might be usable and green means that the foil passed all evalua-
1257 tions.

1258 2.3.4 Optical scanning

1259 The etching process is a delicate one; many things can go wrong, that are not visible
1260 by eye in the coarse optical inspection. It is expected that the hole parameters are
1261 connected with the foil's electric properties [], so a precise optical measurement

Figure 29: An example image taken of a GEM foil with false colors.

can help in classifying the foils. For example, smaller holes create more intense and focused fields, which would result in larger amplification of their avalanche electrons, i.e. the local gain would be larger.

The foils are scanned with the help of a scanning robot. The setup along with most of the software was developed at the Detector Laboratory of the University of Helsinki []

Each image is a false colour superposition of two images, one with foreground illumination and one with background illumination. In this way one can observe the three relevant diameters of the foil, the top, middle and bottom diameters. The background light highlights the middle holes, while the foreground illumination captures either the top or the bottom depending on the orientation of the foil as the foils are scanned from both sides. Fig. 29

The setup takes images with area about $11.3\text{ mm} \times 8.5\text{ mm}$, corresponding to 2560 by 1920 pixels, resulting in a total of 2000-3500 individual images for both sides of a GEM foil, depending on its type. The images are fed into neural network classifier, which identifies the holes, finds defects and extracts the hole parameters by fitting ellipses to the recognised contours. Thus every individual hole can be measured, which otherwise would be completely unfeasible as even the smallest of foils has about 10 million holes.

Long term HV measurement of the GEM foils

After the optical scanning, the foils are subjected to a long term (5-12 hours) high voltage leakage current measurement. Each segment of the GEM foil is connected to a high voltage and the leakage current is measured separately for each segment, by the connected picoamper-meter (pA-meter) []. The accepted leakage current in each segment is 0.16 nA, foils with larger values are discarded.

Gain scan

A small subset of the foils were put through a gain scan. The gain scan could only be performed in the QA-A centre of Budapest. As the time required to scan 1 foil was several days, the gain scan couldn't be performed even for all foils in Budapest.

The gain scan uses charged particles provided by a ^{55}Fe source, which was placed above the foil. It emits X-ray photons with an energy of 5.9 keV. The photons will convert to electrons in the gain scanner's Ar + CO₂ gas mixture,

either via photoelectric effect or via Compton Scattering. There electrons travel a few microns in the gas, ionising the gas along their path.

Below the GEM frame, there is a multiwire proportional pad, with perpendicular wires with a resolution of 4 mm in x and 3 mm in y . Amplification is measured both with (HV) and without (reference) voltage over the GEM foil. The HV measurement is divided with the reference measurement, which results in the gain map of the GEM.

Gain correlations

2.3.5 Particle identification

One guiding principle in the design of ALICE was to achieve good particle identification (PID) over a large part of phases space and for several different particle types. In ALICE there are several detectors taking part in the identification of particles.

One of the particle identification detectors is the transition radiation detector (TRD) [?]. Its main task is identifying electors with momenta larger than 1 GeV. Transition radiation is produced when highly relativistic particles traverse the boundary between two media having different dielectric constants. The average energy of the emitted photon is approximately proportional to the Lorentz factor γ of the particle, which provides an excellent way of discriminating between electrons and pion. ALICE TRD is made of a composite layer of foam and fibres. The emitted photons are then measured in six layers of Xe/CO₂ filled time expansion wire chambers.

The time of flight (TOF) detector uses a very simple physics principle, i.e. calculating the velocity of the particle using the time of flight between two points. Combining this with the momentum of particle, obtained from the tracking detectors, one can calculate the mass of the particle, which identifies particles. The TOF detector consists of multigap resistive wire chambers. These are stacks of resistive plates spaced equally. They allow time of flight measurements in large acceptance with high efficiency and with a resolution better than 100 ps.

The third specific particle identification detector is the high momentum particle identification (HMPID) detector. The HMPID uses a ring imaging Cherenkov counter to identify particles with momenta larger than 1 GeV. Particles moving through a material faster than the speed of light in the material will produce Cherenkov radiation. The velocity of the particle determines the angle at which the radiation is emitted. Measuring this angle gives the velocity of the particle. This can be again used to calculate the mass of the particle, if the momentum is known. In HMPID the material is a liquid radiator and the photons are measured with multiwire proportional chambers in conjunction with photocathodes.

1333 In addition to the specific particle identification detectors, the general purpose
1334 tracking detectors can be used for identification through the use of specific energy
1335 loss of charged particles traversing through a medium and the transition radiation
1336 emitted by charged particles when crossing the boundary between two materials.

1337 dE/dx measurements are provided by the last four layers of the ITS detector, i.e.
1338 the SDD and the SSD, thanks to their analog readout. [108] ITS provides particle
1339 identification in the low p_T region, up to 1GeV, and pions reconstructed in the
1340 standalone mode can be identified down to 100 MeV. Similar to ITS the TPC
1341 detector provides specific energy loss measurements. TPC can identify charged
1342 hadrons up to p_T 1 – 2GeV as well as light nuclei, He3 and He4.

1343 2.3.6 Electromagnetic Calorimeter

1344 Calorimeters are designed to measure the energy of particles. Electromagnetic
1345 calorimeters specialise in detecting particles that interact primarily through the
1346 electromagnetic interaction, namely photons and electrons. They are required in
1347 many neutral meson and direct photon analyses. In addition the energy informa-
1348 tion enhance jet measurements.

1349 ALICE has two electromagnetic calorimeters, the photon spectrometer (PHOS) [109]
1350 and the electromagnetic calorimeter (EMCal) [?]. PHOS is a homogeneous calorime-
1351 ter that consists of scintillating PbWO₄ crystals, which generate a bremsstrahlung
1352 shower and produce scintillation light. The energy of the particle determines the
1353 amount of light produced. To improve the charged particle rejection, PHOS in-
1354 cludes a charged particle veto detector (CPV) [?]. PHOS is built to have a very
1355 fine granularity, making it well suited for measuring direct photons and neutral
1356 mesons.

1357 EMCal is a sampling calorimeter. It consists of layers of lead and scintilla-
1358 tor tiles. The lead tiles produce the shower and scintillator tiles the light. The
1359 signal is then read with wavelength shifting fibres. The acceptance of EMCal in
1360 the azimuthal angle is 80 deg < ϕ < 187 deg. During long shutdown 1 in 2013-
1361 2015, EMCal was extended with the di-jet calorimeter (DCal) [110], giving an
1362 additional acceptance region of 260 deg < ϕ < 320 deg. This provides partial
1363 back-to-back coverage. In comparison to PHOS, EMCal has coarser granularity,
1364 but a significantly larger acceptance, making it suitable for jet physics.

1365 2.3.7 Forward detectors

1366 ALICE includes a few small and specialised detectors of importance. The event
1367 time is determined with very good precision (< 25 ns) by the T0 detector [?]. T0
1368 consists of two sets of Cherenkov counters that are mounted around the beam pipe
1369 on both sides of the interaction point. T0 gives the luminosity measurement in

1370 ALICE.

1371 Another small detector in the forward direction is the V0 detector [?]. This
1372 consists of two arrays of segmented scintillator counters located at $-3.7 < \eta <$
1373 -1.7 and $2.8 < \eta < 5.1$. V0 is used as a minimum bias trigger and for rejection
1374 of beam-gas background. Particle multiplicity in the forward direction can be
1375 related to the event centrality. Thus V0 is the main detector used in centrality
1376 determination in PbPb collisions.

1377 The multiplicity measurement of V0 is complimented by the forward multi-
1378 plicity detector (FMD) [?]. FMD includes five rings of silicon strip detectors that
1379 make up the FMD. FMD gives acceptance in the range $-3.4 < \eta < -1.7$ and
1380 $1.7 < \eta < 5.0$.

1381 During long shutdown 2 in 2019-2020, V0 and T0 will be replaced by the Fast
1382 Interaction Trigger (FIT) detector [?]. For historical reasons elements of FIT are
1383 also referred to as V0+ and T0+. FIT will allow centrality, event plane, luminosity
1384 and interaction time determination in the continuous readout mode, that ALICE
1385 will operate in after 2020.

1386 For photon multiplicity measurement ALICE has the photon multiplicity de-
1387 tector (PMD) [?]. PMD uses two planes of gas proportional counters with a
1388 cellular honeycomb structure. PMD gives the multiplicity and spatial distribution
1389 of photons in the region $2.3 < \eta < 3.7$.

1390 On top of the ALICE magnet there is an array of 60 large scintillators called
1391 the ALICE cosmic ray detector (ACORDE) [?]. ACORDE is used as a trigger
1392 for cosmic rays for calibration and alignment.

1393 The only hadronic calorimeters in ALICE are the zero degree calorimeters
1394 (ZDC) [?], which are located next to the beam pipe in the machine tunnel about
1395 116 m from the interaction point. There are two sets of calorimeters. One is
1396 made of tungsten, specialising in measuring neutrons, while the other, made of
1397 brass, is specialised in measuring protons. In heavy ion and especially in proton-
1398 lead collisions, ZDC gives information about the centrality of the event. ZDC is
1399 meant to detect spectators, i.e. parts of the colliding ions that do not take part
1400 in the interaction. If there are more spectators, the collisions is likely to be more
1401 peripheral.

1402 A new detector installed during the long shutdown 1 is the ALICE diffractive
1403 detector (AD) [?]. AD consists of two assemblies, one in each side of the interaction
1404 point, both made of two layers of scintillators. These assemblies are situated about
1405 17 m and 19.5 m away from the interaction points. The pseudorapidity coverage is
1406 $-6.96 < \eta < -4.92$ and $4.78 < \eta < 6.31$. AD greatly enhances ALICE's capability
1407 for diffractive physics measurements that require a large pseudorapidity gap.

1408 **2.3.8 Muon spectrometer**

1409 Outside the main magnet, ALICE has a spectrometer dedicated to measuring
1410 muons [?]. In heavy ion physics muons are mainly used to measure the production
1411 of the heavy quark resonances J/ψ , Ψ' , Υ , Υ' and Υ'' .

1412 The muon spectrometer consists of three parts, the absorber, the muon tracker
1413 and the muon trigger. The absorber is meant to remove the hadronic background
1414 as efficiently as possible. After the absorber there are ten plates of thin cathode
1415 strip tracking stations with high granularity, the muon tracker. After the muon
1416 tracker there is a layer of iron to filter out any remaining particles, other than
1417 muons. The muon trigger is located behind this layer. The trigger consists of four
1418 resistive plate chambers.

1419 **2.3.9 Trigger**

1420 High energy physics experiments need triggers to select interesting physics. Ex-
1421 periments such as CMS and ATLAS at CERN look for extremely rare events with
1422 up to 40 million events each second. Such amounts can't be recorded real-time as
1423 many detectors require some time for the readout, up to 1 ms/event in ALICE.
1424 Thus one uses triggers, i.e. a set of very fast hardware based decisions on which
1425 events are to be saved. Additionally one needs some confirmation that an event
1426 has even occurred.

1427 For ALICE the target event rates are 1 MHz for ppcollisions, 0.1-2 kHz for
1428 Pb–Pb collisions and 200 kHz for the 2013 p–Pb collisions.

1429 At ALICE the main system responsible for the trigger decisions is the AL-
1430 ICE Central Trigger Processor (CTP) [?]. The CTP generates three levels of
1431 hierarchical hardware triggers - Level 0, Level 1 and Level 2, (L0, L1 and L2 re-
1432 spectively) before an event is accepted and transmitted to the Data Acquisition
1433 system (DAQ). Afterwards additional software assessments are performed by the
1434 High Level Trigger (HLT).

1435 Triggers can roughly put into two classes, minimum bias triggers that make sure
1436 no empty events are recorded, and rare triggers that require specific signatures in
1437 ALICE detectors, such as large energy deposits in EMCal or two muons in the
1438 muon arm acceptance.

1439 **Minimum bias trigger**

1440 Several of the ALICE detectors are used to make the initial minimum bias trigger
1441 decisions. These include the SPD layers of ITS, V0 and T0. SPD can count the
1442 number of hits in the first two layers of ITS. Minimum bias ppcollisions typically
1443 require at least one hit in either SPD or V0A/V0C

1444 Similarly Pb–Pb triggers looked at both V0 and SPD

1445 EMCal trigger

1446 In addition to the minimum bias triggers, the most relevant trigger for this thesis
1447 is the EMCal trigger.

1448 ALICE EMCal provides two levels of trigger signal, L0 and L1, which allows
1449 triggering on either single shower deposits or integrated energy deposits in larger
1450 areas, i.e. jets.

1451 As inputs the trigger gets exclusive sets of 2×2 EMCal towers, to limit the
1452 number of channels that need to be processed. The L0 trigger then checks for
1453 energy deposits within a rolling window of 2×2 trigger channels (4×4 towers).
1454 For L0 this is done in units of (? \times ?) towers. A single bit OR decision of all
1455 individual L0 units is forwarded to the CTP as the EMCal L0 trigger decision.

1456 Areas of 4×4 towers most probably will contain only a single shower (or two
1457 adjacent showers coming from a single decayed π^0). Thus the trigger can be called
1458 the single shower trigger.

1459 The L0 information is additionally forwarded to the Level 1 trigger, which
1460 recomputes similar 2×2 channel decisions to produce the single shower trigger,
1461 but L1 can perform the calculation also on the borders between trigger units. In
1462 addition the L1 trigger can check for energy deposits inside a larger 16×16 channel
1463 (32×32 towers) window, which is considered to be the jet trigger.

1464 The L1 trigger can compare up to two thresholds for each single shower and
1465 jet trigger. There is a dedicated link in between the V0 detector and EMCal STU,
1466 which can provide centrality information, used to compute a dynamical threshold
1467 as a function of the V0 multiplicity.

1468 The trigger subsystem provides both the L0 and L1 decisions to the CTP and
1469 DAQ.

1470 3 Event and track selection

1471 The $\sqrt{s_{\text{NN}}} = 5.02$ TeV p–Pb ($1.3 \cdot 10^8$ events, $\mathcal{L}_{\text{int}} = 620 \text{ nb}^{-1}$) collisions were
1472 recorded in 2013 by the ALICE detector [111]. The details of the performance of
1473 the ALICE detector during LHC Run 1 (2009–2013) are presented in Ref. [112].

1474 The analysis uses charged tracks that are reconstructed with the Inner Track-
1475 ing System (ITS) [113] and the Time Projection Chamber (TPC) [114]. These
1476 detectors are located inside the large solenoidal magnet, that provides a homo-
1477 geneous magnetic field of 0.5 T. Tracks within a pseudorapidity range $|\eta| < 0.9$
1478 over the full azimuth can be reconstructed. The ITS is made up of the innermost
1479 Silicon Pixel Detector (SPD), the Silicon Drift Detector (SDD) and the outermost
1480 Silicon Strip Detector (SSD). Each of these consists of two layers. The TPC is a
1481 cylinder filled with gas. Gas is ionised along the path of charged particles. Liber-
1482 ated electrons drift towards the end plates of the cylinder where they are detected.
1483 Combining the information from the ITS and the TPC provides a resolution rang-
1484 ing from 1 to 10 % for charged particles with momenta from 0.15 to 100 GeV/c.
1485 For tracks without the ITS information, the momentum resolution is comparable
1486 to that of ITS+TPC tracks below transverse momentum $p_T = 10 \text{ GeV}/c$, but for
1487 higher momenta the resolution reaches 20 % at $p_T = 50 \text{ GeV}/c$ [112, 115].

1488 Neutral particles used in jet reconstruction are reconstructed by the Electro-
1489 magnetic Calorimeter (EMCAL) [116]. The EMCAL covers an area with a range
1490 of $|\eta| < 0.7$ in pseudorapidity and 100 deg in azimuth. EMCAL is complimented
1491 with the Dijet Calorimeter (DCal) [110] and Photon Spectrometer (PHOS) [109]
1492 that are situated opposite of the EMCAL in azimuth. PHOS covers 70 degrees
1493 in azimuth and $|\eta| < 0.12$. The DCal is technologically identical to EMCal. The
1494 DCal coverage spans over 67 degrees in azimuth, but in pseudorapidity the mid
1495 region is occupied by the PHOS. In between PHOS and DCal active volumes, there
1496 is a gap of 10 cm. DCal is fully back-to-back with EMCal.

1497 The combination of charged tracks with $p_T > 0.15 \text{ GeV}/c$ and neutral particles
1498 with $p_T > 0.30 \text{ GeV}/c$ is used to construct jets.

1499 The V0 detector [117] provides the information for event triggering. The V0
1500 detector consists of two scintillator hodoscopes that are located on either side of
1501 the interaction point along the beam direction. It covers the pseudorapidity region
1502 $-3.7 < \eta < -1.7$ (V0C) and $2.8 < \eta < 5.1$ (V0A). For the 2013 p–Pb collisions
1503 events are required to have signals in both V0A and V0C. This condition is used
1504 later offline to reduce the contamination of the data sample from beam-gas events
1505 by using the timing difference of the signal between the two stations [112].

1506 EMCAL is also used to provide the jet trigger used in triggered datasets. EM-
1507 CAL can be used to trigger on single shower deposits or energy deposits integrated
1508 over a larger area. Latter case is used for jet triggers. The EMCAL trigger defini-
1509 tion in the 2013 p–Pb collisions requires an energy deposit of either 10 GeV for the

1510 low threshold trigger or 20 GeV for the high threshold trigger in a 32×32 patch
 1511 size.

1512 In p–Pb collisions the tracks are selected following the hybrid approach [118]
 1513 which ensures a uniform distribution of tracks as a function of azimuthal angle
 1514 (φ). The momentum resolutions of the two classes of particles are comparable up
 1515 to $p_T \approx 10$ GeV/ c , but after that, tracks without ITS requirements have a worse
 1516 resolution [112, 115].

1517 3.1 statistics

1518 Number of jets in different datasets and with different jet finders is shown in table
 1519 2. Background statistics for number of background cones (number of jets minus
 1520 number of discarded cones) are shown in table 3. Ratio of background cones to
 1521 number of jets is shown in table 4. The likelihood of having to discard a jet from
 background calculation is about 1-2%.

Table 2: Number of found jets by dataset and jet p_T bin

| Jet p_T | 5-10 | 10-20 | 20-30 | 30-40 | 40-60 | 60-80 | 80-100 | 100-150 | 150-500 |
|---------------------|---------|--------|-------|-------|-------|-------|--------|---------|---------|
| MBFullR04 | 4969393 | 621753 | 32552 | 5584 | 1974 | 310 | 90 | 37 | 5 |
| MBFullR05 | 4750567 | 826598 | 42373 | 5543 | 1719 | 276 | 73 | 29 | 3 |
| MBChargedR04 | 3144538 | 673419 | 37783 | 4121 | 1009 | 148 | 36 | 12 | 1 |
| MBChargedR05 | 2229247 | 175763 | 7961 | 1270 | 410 | 61 | 12 | 3 | |
| TriggeredFullR04 | 187557 | 115927 | 78138 | 51317 | 39262 | 8621 | 2409 | 1167 | 171 |
| TriggeredFullR05 | 99991 | 77147 | 48612 | 34325 | 28104 | 6342 | 1726 | 794 | 104 |
| TriggeredChargedR04 | 37411 | 29945 | 18186 | 13148 | 11142 | 2517 | 675 | 326 | 44 |
| TriggeredChargedR05 | 433155 | 175031 | 54789 | 19776 | 10626 | 1983 | 457 | 194 | 15 |

1522

Table 3: Number of background cones used in perpendicular cone background calculation

| Jet p_T | 5-10 | 10-20 | 20-30 | 30-40 | 40-60 | 60-80 | 80-100 | 100-150 | 150-500 |
|---------------------|---------|--------|-------|-------|-------|-------|--------|---------|---------|
| MBFullR04 | 4947583 | 617895 | 32357 | 5548 | 1965 | 310 | 90 | 37 | 5 |
| MBFullR05 | 4710217 | 815461 | 41584 | 5439 | 1698 | 273 | 73 | 29 | 3 |
| MBChargedR04 | 3117495 | 661106 | 36739 | 4014 | 988 | 144 | 36 | 12 | 1 |
| MBChargedR05 | 2195286 | 172919 | 7860 | 1249 | 406 | 61 | 12 | 3 | |
| TriggeredFullR04 | 186574 | 115376 | 77949 | 51216 | 39196 | 8603 | 2405 | 1167 | 171 |
| TriggeredFullR05 | 99102 | 76462 | 48320 | 34216 | 28038 | 6334 | 1722 | 794 | 103 |
| TriggeredChargedR04 | 37160 | 29543 | 17988 | 13099 | 11129 | 2515 | 675 | 326 | 44 |
| TriggeredChargedR05 | 313421 | 140707 | 45229 | 16243 | 8709 | 1604 | 377 | 154 | 14 |

Table 4: Ratio of background cone number to number of jets

| | | | | | | | | | |
|---------------------|--------|--------|--------|--------|--------|---------|---------|---------|---------|
| MBFullR04 | 99.56% | 99.38% | 99.40% | 99.36% | 99.54% | 100.00% | 100.00% | 100.00% | 100.00% |
| MBFullR05 | 99.15% | 98.65% | 98.14% | 98.12% | 98.78% | 98.91% | 100.00% | 100.00% | 100.00% |
| MBChargedR04 | 99.14% | 98.17% | 97.24% | 97.40% | 97.92% | 97.30% | 100.00% | 100.00% | 100.00% |
| MBChargedR05 | 98.48% | 98.38% | 98.73% | 98.35% | 99.02% | 100.00% | 100.00% | 100.00% | 100.00% |
| TriggeredFullR04 | 99.48% | 99.52% | 99.76% | 99.80% | 99.83% | 99.79% | 99.83% | 100.00% | 100.00% |
| TriggeredFullR05 | 99.11% | 99.11% | 99.40% | 99.68% | 99.77% | 99.87% | 99.77% | 100.00% | 99.04% |
| TriggeredChargedR04 | 99.33% | 98.66% | 98.91% | 99.63% | 99.88% | 99.92% | 100.00% | 100.00% | 100.00% |
| TriggeredChargedR05 | 72.36% | 80.39% | 82.55% | 82.13% | 81.96% | 80.89% | 82.49% | 79.38% | 93.33% |

1523 4 Analysis method

1524 4.1 Jet Finding

1525 The analysis uses reconstructed jets as estimates of the original parton. Essentially
1526 when reconstructing jets, nearby tracks are combined into jets. Collisions between
1527 hadrons are never as clean as electron-electron collisions. Even for a proton-proton
1528 collision there are participant partons, that will produce a soft background in ad-
1529 dition to the hard scattering products. Jet reconstruction must deal with this soft
1530 background. The reconstruction is never perfect, one can have uncorrelated tracks
1531 that get included in the jet and some tracks originating from the parton are missed
1532 by the reconstruction. There are several methods to perform the reconstruction,
1533 all of which require some kind of size parameter, which cuts out jet participants
1534 too far from the jet axis. The tracks that are grouped into a jet are referred to as
1535 jet constituents.

1536 The analysis is performed by analysing jet constituents. In each collision event,
1537 the jets are reconstructed using FastJet [119] with the anti- k_T algorithm [120].
1538 Jets for $R=0.4$ are selected in $|\eta| < 0.25$ to satisfy the fiducial acceptance of the
1539 EMCal. In jet reconstruction both charged tracks with $p_T > 0.15 \text{ GeV}/c$ and
1540 neutral clusters with $p_T > 0.30 \text{ GeV}/c$ are considered. In the analysis, results are
1541 presented in terms of the jet transverse momentum $p_{T\text{jet}}$.

1542 4.1.1 Anti k_T algorithm

1543 Jets are reconstructed using the anti- k_T algorithm [120]. The algorithm works by
1544 trying to undo the splittings through combining protojets. The algorithm creates
1545 a list of protojets. At the beginning the list is populated by converting each track
1546 in the event into a protojet. Then the algorithm proceeds by combining these
1547 protojets.

1548 The algorithm calculates distance measures for each individual protojet and
1549 for each possible pair of protojets. For individual protojets this depends only on
1550 the transverse momentum of the track.

$$k_{T,i}^2 = p_{T,i}^{2p}$$

1551 For each pair of protojets the distance measure is calculated as

$$k_{T,(i,j)}^2 = \min(p_{T,i}^{2p}, p_{T,j}^{2p}) \frac{\Delta R_{i,j}^2}{D^2},$$

1552 where

$$R_{i,j} = (\phi_i - \phi_j)^2 + (y_i - y_j)^2$$

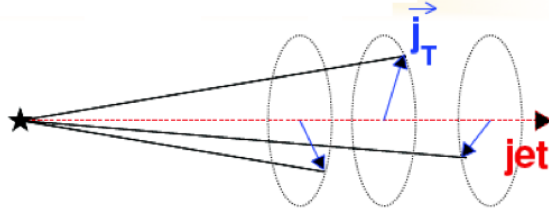


Figure 30: Illustration of \vec{j}_T . The jet fragmentation transverse momentum, \vec{j}_T , is defined as the transverse momentum component of the track momentum, \vec{p}_{track} , with respect to the jet momentum, \vec{p}_{jet} .

If $k_{T,i}$ is the smallest quantity then the protojet is a jet and it is removed from further consideration. If $k_{T,(i,j)}$ is the smallest quantity the two protojets are merged. This is iterated until no protojets are left.

The choice of the power p in the distance measure depends on the algorithm used

- $p = 1$: k_T algorithm
- $p = 0$: Cambridge Aachen algorithm
- $p = -1$: anti- k_T algorithm

With the choice $p = -1$ in anti- k_T algorithm, the softest splittings are undone first. One consequence of the power choice in the anti- k_T algorithm is that reconstructed jets have a shape close to circular.

4.2 j_T

The jet fragmentation transverse momentum, j_T , is defined as the component of the constituent particle momentum, \vec{p}_a , transverse to the jet momentum, \vec{p}_{jet} . The resulting \vec{j}_T is illustrated in Fig. 30. The length of the \vec{j}_T vector is

$$j_T = \frac{|\vec{p}_{\text{jet}} \times \vec{p}_{\text{track}}|}{|\vec{p}_{\text{jet}}|}. \quad (35)$$

It is commonly interpreted as a transverse kick with respect to the initial hard parton momentum that is given to a fragmenting particle during the fragmentation process, which is a measure of the momentum spread of the jet fragments [].

The reconstructed jet axis is used for j_T reference. Any charged track within a fixed cone with radius R is taken as a jet constituent, as opposed to using the

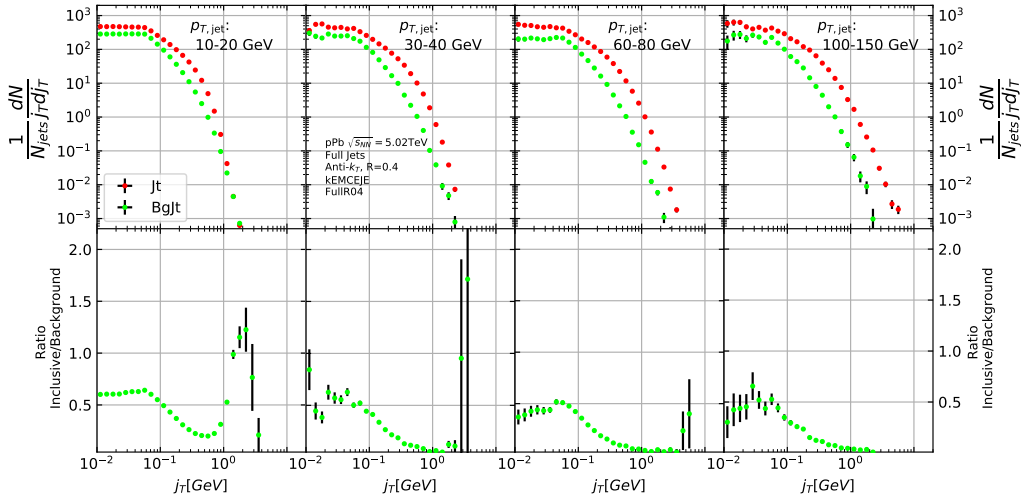


Figure 31: Inclusive j_T with background

1573 constituent list provided by the jet algorithm. Anti- k_T produces jets that are
 1574 very circular in shape. Thus this doesn't change the constituent list considerably.
 1575 Neutral tracks are used only in jet reconstruction.

1576 j_T results are shown as

$$\frac{1}{j_T} \frac{dN}{dj_T} \quad (36)$$

1577 distributions. The logic behind this is that j_T is inherently a two-dimensional
 1578 observable, comprised of j_{Tx} and j_{Ty} components. So the actual physical observable
 1579 would be

$$\frac{d^2N}{dj_{Tx} dj_{Ty}} \quad (37)$$

1580 Changing into polar coordinates with $j_{Tr} = j_T$ and θ gives

$$\frac{d^2N}{j_T dj_T d\theta}, \quad (38)$$

1581 where j_T over the azimuth θ should stay constant and it can be integrated over,
 1582 which gives

$$\frac{1}{2\pi} \frac{dN}{j_T dj_T}. \quad (39)$$

1583 Results of the raw inclusive j_T distribution in four $p_{T,jet}$ bins with background
 1584 are shown in figure 31. Background is further discussed in Sec. 4.4

1585 4.3 Unfolding

1586 Extend unfolding

1587 The raw inclusive j_T distributions are corrected for the detector inefficiency
1588 using the unfolding method. The response matrix for the unfolding is obtained
1589 from a PYTHIA [121] simulation.

Measured distributions are affected by two main factors; Limited acceptance -
The probability to observe a given event is less than one and limited resolution -
Quantity x cannot be determined exactly, but there is a measurement error. True
 $f(x)$ and measured $g(y)$ distributions are connected by a convolution integral.
Including statistical fluctuations this becomes

$$\hat{g}(y) = \int_a^b A(y, x) f(x) dx + \epsilon(y),$$

where A is the detector response obtained by (for example) Monte Carlo simulations and $\epsilon(y)$ is the term coming from statistical fluctuations. If x and y are discrete variables we have

$$\hat{g}_i = \sum_{j=1}^m A_{ij} f_j + \epsilon_i,$$

Or in matrix form

$$\hat{g} = Af + \epsilon$$

If the only detector effect is limited acceptance, A is a diagonal matrix. In a general discrete case the (naive) solution is obtained by the inverse matrix

$$\hat{f} = A^{-1}\hat{g}$$

1590 However this usually leads to oscillating solutions and determining the inverse
1591 matrix can be difficult.

1592 Two common methods to perform this inversion are Bayesian and SVD unfolding
1593 methods. Often the solution requires some additional *a priori* information.
1594 For example the solution should be smooth in most cases.

1595 4.3.1 Bayesian unfolding

The bayesian (iterative) method is based on the Bayes formula [].

$$P(C_i|E_j) = \frac{P(E_j|C_i) P_0(C_i)}{\sum_{l=1}^{n_C} P(E_j|C_l) P_0(C_l)},$$

1596 i.e. the probability of Cause ("truth") C_i given Effect ("observed") E_j is pro-
1597 portional to the probability of observing E_j given C_i (response matrix) and the
1598 truth distribution $P_0(C_i)$.

At first P_0 is given some starting distribution, either a uniform distribution or some guess of the final distribution. Taking into account the inefficiency this gives

$$\hat{n}(C_i) = \frac{1}{\epsilon_i} \sum_{j=1}^{n_E} n(E_j) P(C_i|E_j),$$

where

$$P(C_i|E_j) = \frac{P(E_j|C_i) P_0(C_i)}{\sum_{l=1}^{n_C} P(E_j|C_l) P_0(C_l)},$$

1599 and

$$\hat{n}(C_i) = \frac{1}{\epsilon_i} \sum_{j=1}^{n_E} n(E_j) P(C_i|E_j). \quad (40)$$

First $P(C_i|E_j)$ is calculated with the uniform distribution or best guess of the shape of the distribution. This is then used to calculate the new distribution $\hat{P}(C_i)$

$$\hat{N}_{true} = \sum_{i=1}^{n_C} \hat{n}(C_i), \hat{P}(C_i) = P(C_i|n(E)) = \frac{\hat{n}(C_i)}{\hat{N}_{true}}$$

1600 P_0 is then replaced with \hat{P} and the procedure is repeated until an acceptable
1601 solution is found.

1602 The bayesian procedure alongside with the SVD unfolding method are implemented in the RooUnfold package [122], which is used to perform the unfolding in
1603 practice. In RooUnfold the number of iterations is given beforehand. In practice
1604 this requires some trial and error. The number of iterations should be as low as
1605 possible, as the errors increase when going further in the iterations, but the number
1606 of iterations must be high enough so that the correct distribution is extracted.
1607

1608 Error propagation in the Bayesian procedure

1609 The measured distribution has some statistical uncertainty, this should be reflected
1610 in the unfolded distribution. Additionally the response matrix may have some
1611 uncertainty if the statistics used in the Monte Carlo simulation were limited.

1612 For errors originating from the measured distribution RooUnfold uses the error
1613 propagation matrix

$$\frac{\partial \hat{n}(C_i)}{\partial n(E_j)} = M_{ij} + \frac{\hat{n}(C_i)}{n_0(C_i)} \frac{\partial n_0(C_i)}{\partial n(E_j)} - \sum_{k=1}^{n_E} \sum_{l=1}^{n_C} \frac{n(E_k) \epsilon_l}{n_0(C_l)} M_{ik} M_{lk} \frac{\partial n_0(C_l)}{\partial n(E_j)}, \quad (41)$$

1614 where $\hat{n}(C_i)$ is the unfolded result from Eq. 40. This depends upon the matrix
1615 $\frac{\partial n_0(C_i)}{\partial n(E_j)}$, which is $\frac{\partial \hat{n}(C_i)}{\partial n(E_j)}$ from the previous iteration. In the first iteration, $\frac{\partial n_0(C_i)}{\partial n(E_j)} = 0$
1616 and $\frac{\partial \hat{n}(C_i)}{\partial n(E_j)} = M_{ij}$.

1617 The error propagation matrix V is used to obtain the covariance matrix on the
1618 unfolded distribution

$$V(\hat{n}(C_k), \hat{n}(C_l)) = \sum_{i,j=1}^{n_E} \frac{\partial \hat{n}(C_k)}{\partial n(E_i)} V(\hat{n}(E_i), \hat{n}(E_j)) \frac{\partial \hat{n}(C_l)}{\partial n(E_j)}, \quad (42)$$

1619 where $V(\hat{n}(E_i), \hat{n}(E_j))$ is the covariance matrix of the measurements. In
1620 counting experiments common in particle physics, each bin is independently Pois-
1621 son distributed, with

$$V(\hat{n}(E_i), \hat{n}(E_j)) = n(E_i) \delta_{ij} \quad (43)$$

1622 The error propagation matrix for the response matrix is

$$\begin{aligned} \frac{\partial \hat{n}(C_i)}{\partial P(E_j|C_k)} &= \frac{1}{\epsilon_i} \left(\frac{n_0(C_i) n(E_j)}{f_j} - \hat{n}(C_i) \right) \delta_{ik} - \frac{n_0(C_k) n(E_j)}{f_j} M_{ij} + \\ &\frac{\hat{n}(C_i)}{n_0(C_i)} \frac{\partial n_0(C_i)}{\partial P(E_j|C_k)} - \frac{\epsilon_i}{n_0(C_i)} \sum_{l=1}^{n_E} \sum_{r=1}^{n_C} n(E_l) M_{il} M_{rl} \frac{\partial n_0(C_r)}{\partial P(E_j|C_k)}, \end{aligned} \quad (44)$$

1623 where $\frac{\partial n_0(C_i)}{\partial P(E_j|C_k)}$ is the error propagation matrix from the previous iteration,
1624 $\frac{\hat{n}(C_i)}{\partial P(E_j|C_k)}$. From the first iteration, this is zero and the final two terms in Eq. 44
1625 disappear.

1626 The covariance matrix due to these errors is given by

$$V(\hat{n}(C_k), \hat{n}(C_l)) = \sum_{j,s=1}^{n_E} \sum_{i,r=1}^{n_C} \frac{\partial \hat{n}(C_k)}{\partial P(E_j|C_i)} V(P(E_j|C_i), P(E_s|C_r)) \frac{\partial \hat{n}(C_l)}{\partial P(E_s|C_r)}, \quad (45)$$

1627 where $V(P(E_j|C_i), P(E_s|C_r))$ can be taken as multinomial, Poisson or other
1628 distribution.

1629 4.3.2 Toy Monte Carlo

remove? A toy Monte Carlo simulation was performed to see the performance in an ideal case. Sample jet p_T values from observed p_T distribution. Starting from this p_T start creating tracks with

$$p_{\text{track}} = z_{\text{track}} p_{T,\text{jet}}$$

1630 where z_{track} is sampled from the observed z distribution. All tracks below 0.15GeV
1631 are discarded. Sampling is continued until the sum of the track transverse momenta

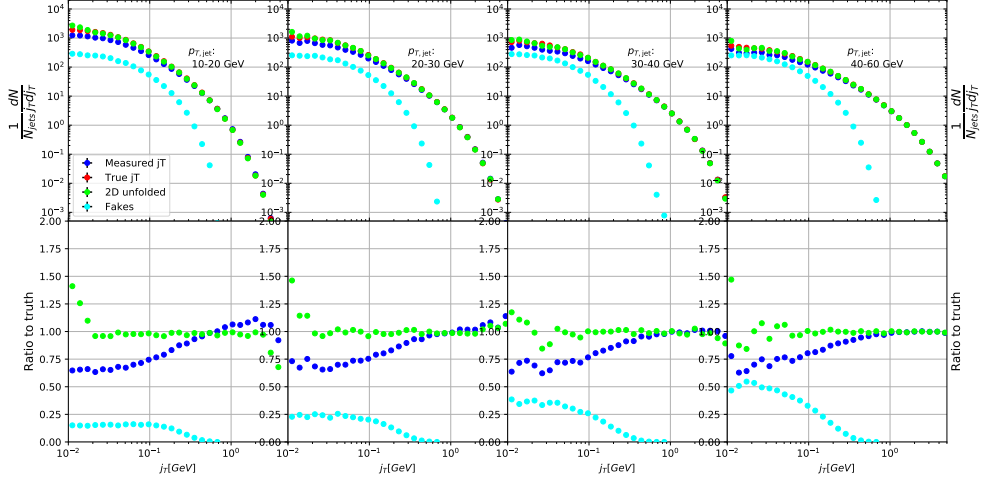


Figure 32: Results from unfolding in Toy Monte Carlo

1632 exceeds the jet transverse momentum. Jet is then defined as the sum of the track
 1633 momenta.

1634 Simultaneously a p_T dependant observation efficiency is applied to the tracks
 1635 and a separate observed jet is calculated using only the observed tracks. Addi-
 1636 tionally a set of fake tracks is added to the observed jet. Tracks are always either
 1637 observed or not at the true momentum. No smearing is added to the observed
 1638 momentum.

Afterwards the tracks are looped over for j_T calculation. For observed tracks we calculate j_T with respect to both the true jet axis and the observed jet. 2D Response matrix is filled with

$$(j_{T,\text{obs}}, p_{T,\text{jet},\text{obs}}, j_{T,\text{true}}, p_{T,\text{jet},\text{true}})$$

1639 In practice this is done with a set of 3D histograms, where $p_{T,\text{jet},\text{true}}$ determines
 1640 the histogram index and the remaining three values the bin in the 3D histogram.

1641 After creating the response matrices, an identical procedure is carried out the
 1642 create testing data. Now instead of filling response matrices, 2D histograms are
 1643 filled with $(j_{T,\text{obs}}, p_{T,\text{jet},\text{obs}})$ and $(j_{T,\text{true}}, p_{T,\text{jet},\text{true}})$

1644 The observed distributions are unfolded using RooUnfold's 2D Bayesian (iter-
 1645 ative) algorithm. Results are shown in figure 32.

1646 4.3.3 Pythia Response matrices

1647 A PYTHIA6 simulation was carried out to determine the response matrices. [Details](#)
 1648 of the simulation

Table 5: j_T and p_T ranges used in unfolding. The same ranges are used for detector and truth level.

| | j_T | $p_{T\text{jet}}$ |
|-----|-------|-------------------|
| Min | 0.01 | 5 |
| Max | 20 | 500 |

1649 Response matrices are filled through correlation between MC detector and
 1650 particle level jets and tracks.

1651 The ranges of both j_T and $p_{T\text{jet}}$ extend the ranges in end results. These are
 1652 shown in Tab. 5. The ranges are the same in detector and particle level.

1653 When calculating j_T for MC particles the code checks whether a corresponding
 1654 detector level track exists and if that track had a j_T value. Additionally the code
 1655 checks for detector level tracks that don't have corresponding particle level track
 1656 or that track does not have j_T value.

1657 Possible cases:

- We find a corresponding track with a j_T value, response matrix is filled normally with $(j_T^{obs}, p_T^{obs}, j_T^{true}, p_T^{true})$
- We don't find a corresponding track. Record (j_T^{true}, p_T^{true}) as a miss
- We find a corresponding track, but it didn't have j_T value. Most likely because it was not part of a jet. Similary record (j_T^{true}, p_T^{true}) as a miss
- For detector level tracks that have no correspondence in particle level set the code records (j_T^{obs}, p_T^{obs}) as a fake

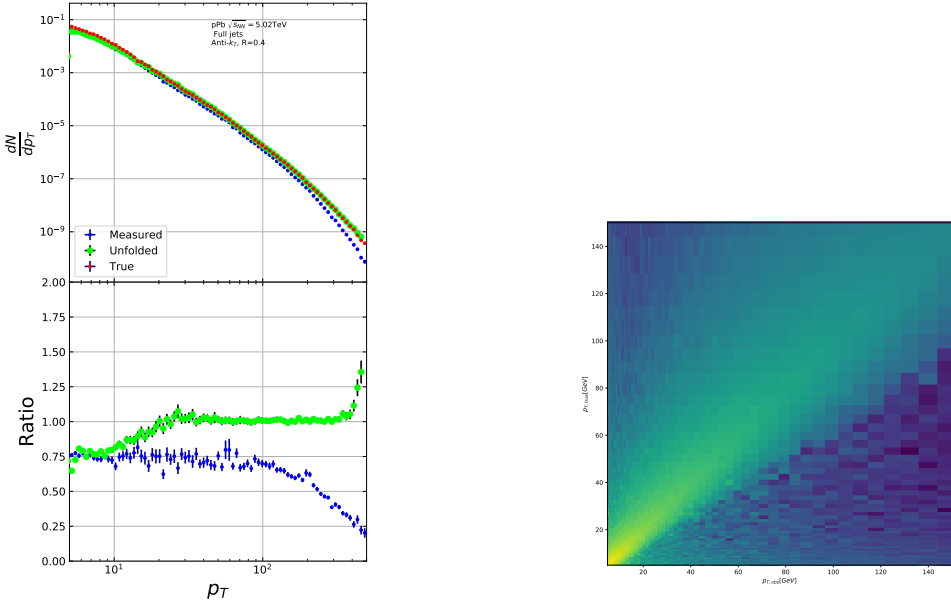
1665 In the analysis code the response matrix is made of an array of 3 dimensional
 1666 histograms, with $(j_{T,obs}, p_{T,obs}, j_{T,true})$ as axes. The histogram index gives the $p_{T,true}$
 1667 value.

1668 4.3.4 Unfolding algorithm

1669 As a primary method unfolding is performed with an iterative (bayesian) algorithm
 1670 using the RooUnfold [122] package. The number of iterations used is 4.

1671 4.3.5 Unfolding closure test

1672 Pythia set is divided in 2 halves. First is used to fill the response matrices, as well
 1673 as record missed and fake tracks. Second half is used to test the effectiveness of
 1674 the unfolding method. Jet p_T distributions are shown in figure 33a and response
 1675 matrix are shown in figure 33b.



(a) Unfolded jet p_T distribution in PYTHIA closure test (b) Jet p_T response matrix from unfolding closure test

Figure 33: Jet p_T in unfolding closure test

Response matrices within single jet p_T bins are shown in figure 34. Results from the closure test are shown in figure 35. In the lowest jet p_T bins unfolding fails to recover the true distribution. The lowest jet p_T bins are dominated by combinatorial jets and thus the true detector response is likely not retrieved.

Above jet p_T 30-40 GeV the distribution is recovered well in the mid j_T region. At $j_T < 0.1$ there is clear discrepancy. The final results are shown only for $j_T > 0.1$. Additionally there is some discrepancy at very high j_T . This is taken into account in the unfolding systematics. (TODO: Show this)

4.4 Background

When calculating j_T distribution for jet constituents there is a contribution from underlying event (UE), i.e. tracks that just happen to be close to the jet axis. To find the signal coming from the actual jet we need to subtract the background (UE) contribution. On a jet-by-jet basis this is impossible, so one must estimate the background contribution in the inclusive distribution. A schematic view of the background contribution is shown in Fig. 36.

We have two methods for background estimation. In the first we look at the direction perpendicular to the jet. This is assumed to be the region least likely to

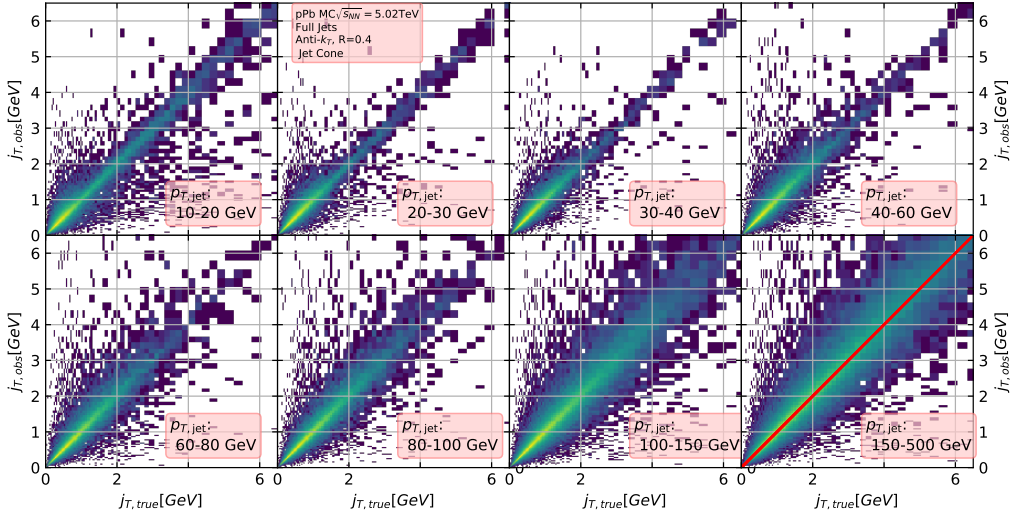


Figure 34: j_T Response matrices in single jet p_T bins

1693 contain jet contributions. In the second method we randomly assign the tracks of
 1694 event new ϕ and η values. The result is guaranteed to be uncorrelated.

1695 4.4.1 Perpendicular cone background

1696 As a primary method to estimate the background we look at regions of the detector
 1697 where there are no tracks from jets, but only uncorrelated tracks from the under-
 1698 lying event. The underlying event is thus estimated by looking at an imaginary
 1699 jet cone perpendicular to the observed jet axis ($\frac{\pi}{2}$ Rotation in ϕ).

1700 After calculating the j_T values for tracks in the jet, we rotate the jet axis by
 1701 $\frac{\pi}{2}$ in positive ϕ direction. We check that there are no other jets closer than $2R$ to
 1702 the rotated axis. If there are then background calculation is skipped for this jet.
 1703 Probability of this happening is 1-2% depending on the jet p_T bin.

1704 If we don't find other jets in the vicinity we move on to estimate the background.
 1705 We find all tracks within a cone of radius R around the rotated axis and calculate
 1706 j_T of these tracks with respect to the rotated axis. Auto-correlations are added to
 1707 match effect to jet. (see 4.4.3)

1708 4.4.2 Random background

1709 In the random background method we look at all tracks in the event, except for
 1710 tracks close to jets found by the jet algorithm. We randomly assign new η and ϕ
 1711 values to all tracks using uniform distributions with $|\eta| < 1.0$. p_T values are kept
 1712 the same. To increase statistics there is a possibility to create a number of random

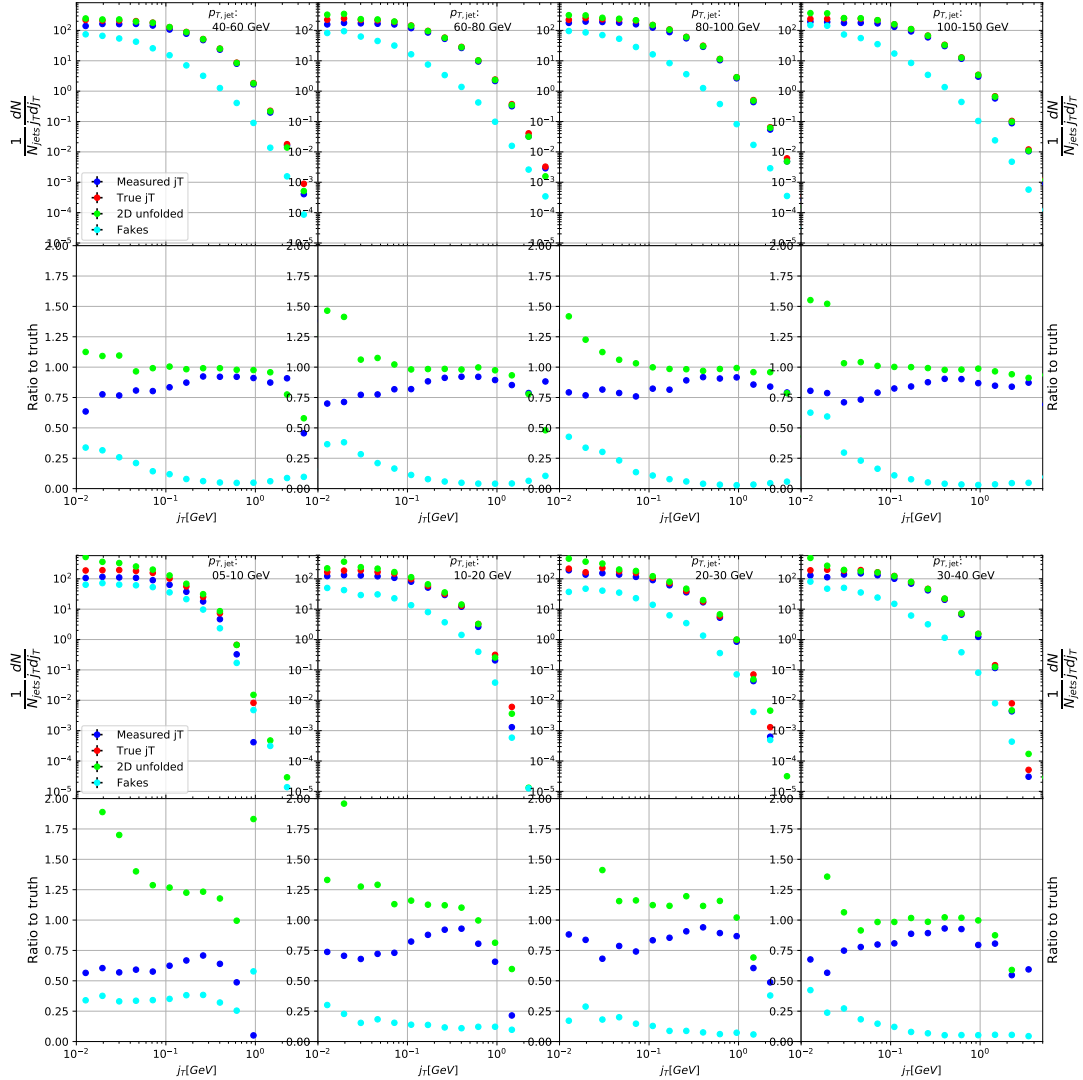


Figure 35: Pythia closure test results. Fake tracks include also tracks that do exist in the true dataset, but for one reason or another were not given j_T values. j_T is only calculated for tracks that are associated with jets

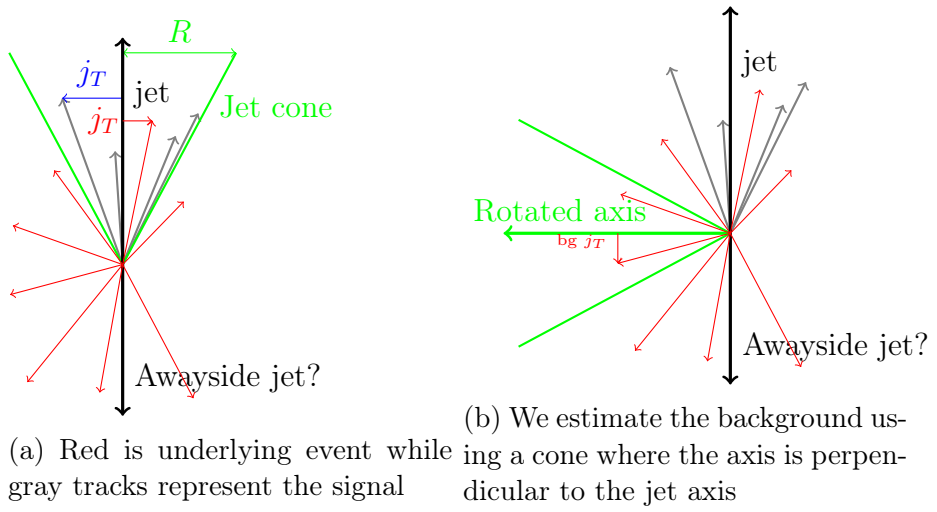


Figure 36: Background estimation

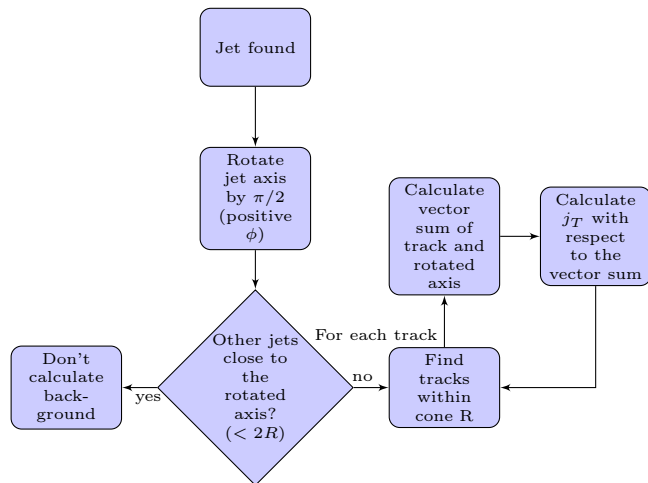


Figure 37: Flowchart representation of the perpendicular cone background procedure

1713 tracks for each actual track. In the analysis we do this 10 times for each track.
1714 Again the track p_T value is kept the same.

1715 We create a random jet cone from uniform η and ϕ distributions. Here $|\eta| <$
1716 0.25. Now we calculate j_T of the random tracks with respect to the random cone
1717 axis. Auto-correlations are added before calculating j_T (see 4.4.3)

1718 4.4.3 Auto-correlations

1719 Jet axis is simply a vector sum of all its constituents. Thus having an additional
1720 track in the jet from the underlying event moves the jet axis towards this track.
1721 Since the axis is now closer to the track, it has a smaller j_T value. Assuming a
1722 1 GeV background track at the edge of a $R = 0.4$ the j_T value would be 0.5 GeV.
1723 If this is added to a 5 GeV jet, the j_T value becomes 0.33 GeV. In a 50 GeV jet it
1724 would be 0.39 GeV. **CHECK** This is a region where the inclusive j_T distribution is
1725 dominated by background. The distribution is also steeply falling. Overestimating
1726 the background can lead to a situation where the background estimation exceeds
1727 the inclusive distribution.

1728 To take this effect into account we can't use a fixed axis for background, but
1729 it has to behave like a jet would when additional tracks are added. Thus before
1730 calculating j_T values we make a vector sum of the track and the axis used for back-
1731 ground, which is either the perpendicular cone axis or the random axis depending
1732 on the background method. In each case the momentum of this background axis
1733 is assumed to be the same as the jet which initiated the background estimation.

1734 In pPb data there is on average about one underlying event track in a $R = 0.4$
1735 cone. If there would be more, one should consider taking the vector sum of all
1736 tracks inside the cone. As there is usually only one track and if there are more it's
1737 unlikely that more than one has high momentum, taking the vector sum track-by-
1738 track should be enough.

1739 4.4.4 Background methods

1740 Comparison between perpendicular cone and random background in figure 38. The
1741 advantage of the random background method is the added amount of statistics as
1742 the procedure can be repeated several times for each event. However, it seems that,
1743 especially in the highest $p_{T\text{jet}}$ bins there is some jet contribution left at the high
1744 end. One should note that the results from perpendicular cone background show no
1745 observable change between $p_{T\text{jet}}$ bins. It is a good indication that the background
1746 is actually dominated by the underlying event over the entire j_T region.

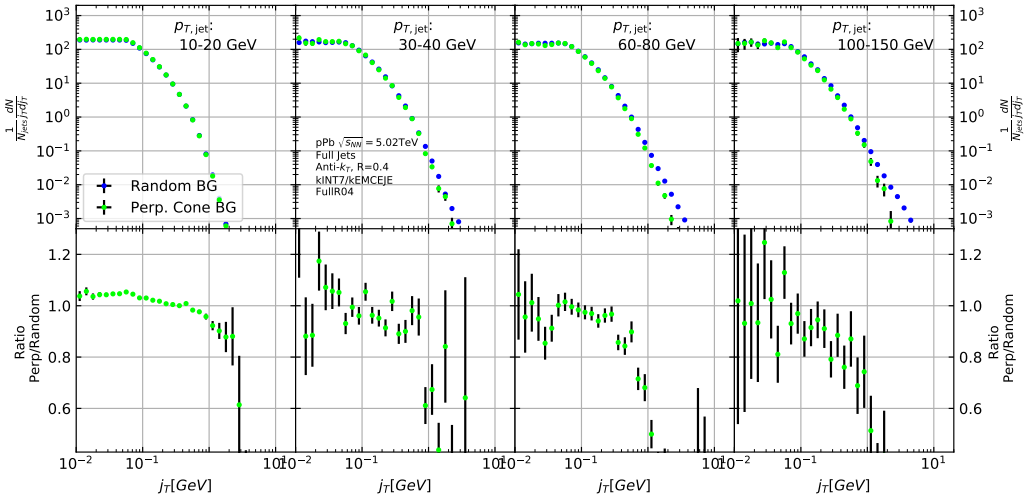


Figure 38: j_T background with two different methods

1747 4.5 Fitting

1748 The resulting signal distribution are fitted with a 2 component function shown in
 1749 Eq. 46. Gaussian distribution is used for low j_T and an inverse gamma function
 1750 is used for high j_T . The gaussian is taken to have the center at $j_T = 0$. In total
 1751 this gives 5 parameters. The fitting procedure was inspired by the dihadron j_T
 1752 analysis by ALICE [2]. The complete fitting function is

$$\frac{1}{N_{\text{jets}} j_T \text{d}j_T} \frac{\text{d}N}{\text{d}j_T} = \frac{B_2}{B_1 \sqrt{2\pi}} e^{-\frac{j_T^2}{2B_1^2}} + \frac{B_3 B_5^{B_4}}{\Gamma(B_4)} \frac{e^{-\frac{B_5}{j_T}}}{j_T^{B_4+1}}. \quad (46)$$

1753 To achieve stable results the fitting is performed in two steps. First each
 1754 component is fitted separately. Gaussian component is fitted to the low end in j_T .
 1755 Inverse gamma component is fitted to j_T above 1 GeV/c. After getting the results
 1756 from the individual fits they are combined into a single function with initial values
 1757 from the individual results and an additional fit is performed. Fitting only the
 1758 gaussian component to the entire distribution produces approximately the same
 1759 result as the gaussian component in the two-component model.

1760 After getting the fit function $\sqrt{\langle j_T^2 \rangle}$ (RMS) and yield values are extracted
 1761 separately from each component. The narrow component RMS is

$$\sqrt{\langle j_T^2 \rangle} = \sqrt{2} B_1,$$

1762 and the wide component RMS value is calculated as

$$\sqrt{\langle j_T^2 \rangle} = \frac{B_5}{\sqrt{(B_4 - 2)(B_4 - 3)}},$$

₁₇₆₃ where it is required that $B_4 > 3$.

₁₇₆₄ The statistical errors can be calculated with the general error propagation
₁₇₆₅ formulas. As a result one gets errors for the narrow component RMS

$$\delta \sqrt{\langle j_T^2 \rangle} = \sqrt{2} \delta B_1 \quad (47)$$

₁₇₆₆ and for the wide component RMS

$$\delta \sqrt{\langle j_T^2 \rangle} = \sqrt{\left(\frac{(5 - 2B_4) B_5 \delta B_4}{(2(B_4 - 2)(B_4 - 3))^{\frac{3}{2}}} \right)^2 + \left(\frac{\delta B_5}{\sqrt{(B_4 - 2)(B_4 - 3)}} \right)^2} \quad (48)$$

1767 **5 Systematic errors**

1768 **Extend Systematics** The systematic uncertainties in this analysis come from the
1769 background estimation, the unfolding procedure and the cuts used to select the
1770 tracks. Tracking uncertainties are estimated from variations of the track selection
1771 cuts defined in Sec. ???. The resulting variations in RMS are shown in Table
1772 7. The uncertainties from unfolding and background subtraction are of the same
1773 magnitude.

1774 The systematics in background estimation were studied using an alternative
1775 method to extract the background, mainly the random background method. The
1776 resulting uncertainty is below 5% for the wide component RMS and below 9% for
1777 the narrow component RMS.

1778 The systematic uncertainty that arises from the unfolding procedure is esti-
1779 mated by performing the unfolding with two separate methods. Data corrected
1780 by the iterative unfolding method are used as the results and the SVD unfolding
1781 method is employed to estimate the uncertainty. In a PYTHIA closure test the
1782 true distribution was in general found to be between the unfolded distributions
1783 from the iterative and SVD method. The difference between the methods when
1784 unfolding data should give a reasonable estimate of the unfolding uncertainty. The
1785 resulting uncertainty is below 8% for both wide and narrow component RMS.

1786 The different source of the systematic uncertainty are considered as uncorre-
1787 lated and the values of each source are summed in quadrature. The resulting
1788 uncertainty is 9 % for the wide component RMS and 12 % for the narrow compo-
1789 nent RMS.

Table 6: Summary of systematic errors

| Systematic | Wide RMS | Narrow RMS |
|------------|----------|------------|
| Background | 5 % | 9 % |
| Unfolding | 8 % | 8 % |
| Tracking | ? % | ? % |
| Total | 9 % | 12% |

1790 **5.1 Background**

1791 Fits are performed on both perpendicular cone and random background signals.
1792 Difference between them is taken as the systematic error. The fits for individ-
1793 ual bins from the random background method are shown in figure 39. Resulting
1794 differences between the methods for different components are shown in figure 40.

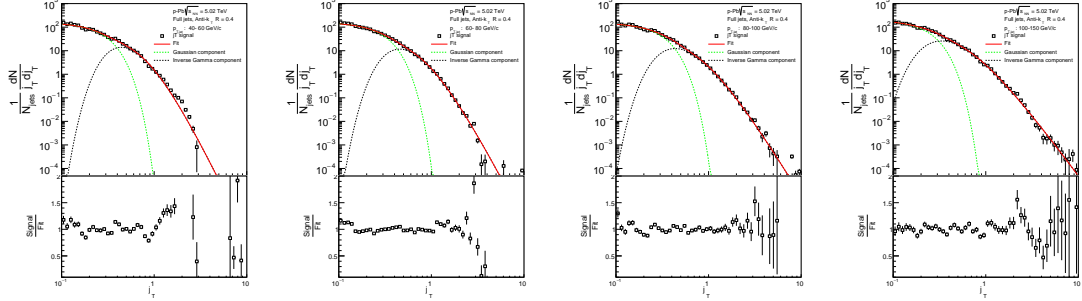


Figure 39: j_T signal with random background subtraction fits in different jet p_T bins

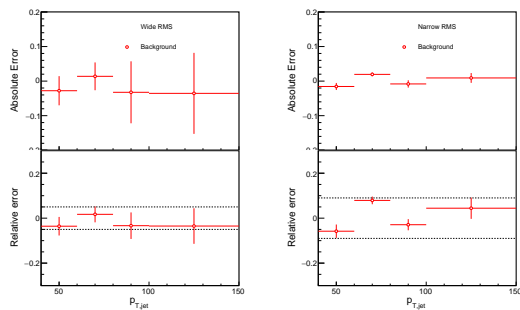


Figure 40: Differences between perpendicular cone and random background subtraction in the resulting RMS values.

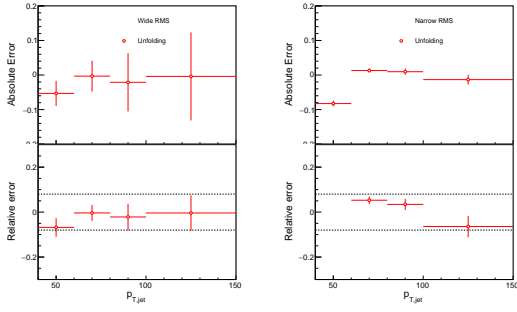


Figure 41: Differences between Bayesian and SVD unfolding in the resulting RMS values

1795 5.2 Unfolding

1796 Unfolding is performed using both SVD and Bayesian unfolding. Difference be-
 1797 tween the methods is taken as the systematic error. Since SVD unfolding does
 1798 not have a 2 dimensional options, the unfolding is done bin by bin. The resulting
 1799 distributions after SVD unfolding and background subtraction with the perpen-
 1800 dicular cone method are shown in fig ???. Resulting differences between the methods
 1801 for different components are shown in figure 41.

1802 5.2.1 Effect of number of iterations

1803 The iterative unfolding algorithm permits the change of number of iterations.
 1804 The unfolding was carried out using different numbers of iterations. The results
 1805 from these different cases are shown in Fig. 42. The results are compared to the
 1806 default unfolding algorithm with 4 iterations. The difference in results between
 1807 the different cases is mostly less than 2.5%.

1808 5.2.2 Effect of different prior

1809 The iterative algorithm requires a prior estimate of the shape of the distribution.
 1810 As a default prior the truth (particle level) distribution is used. To test the effect
 1811 of changing the prior we instead use the unfolded j_T distribution as prior. The
 1812 results are compared to the unfolding algorithm with the default prior. This is
 1813 shown in Fig. 43 The difference in results between the different cases is mostly less
 1814 than 2.5%.

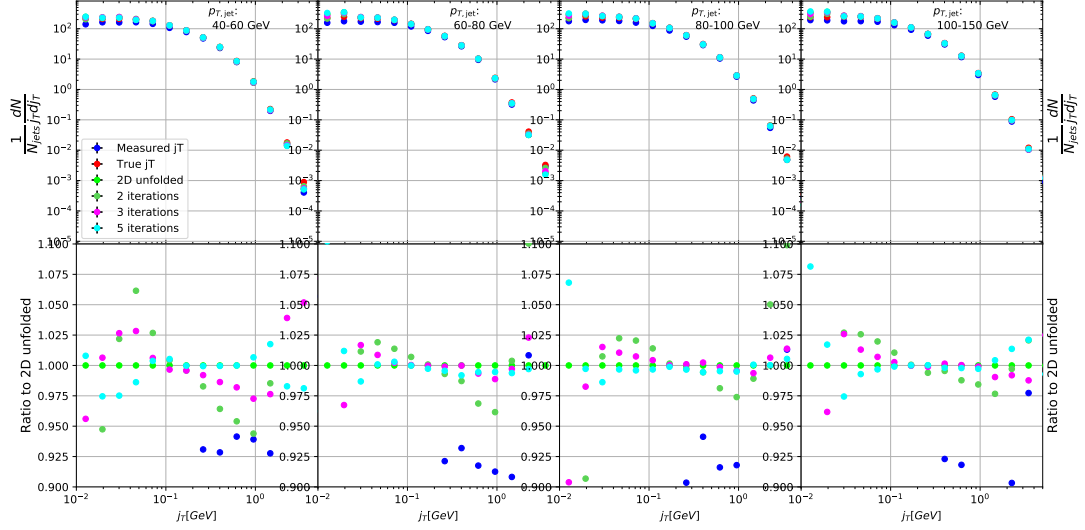


Figure 42: Unfolding with different number of iterations

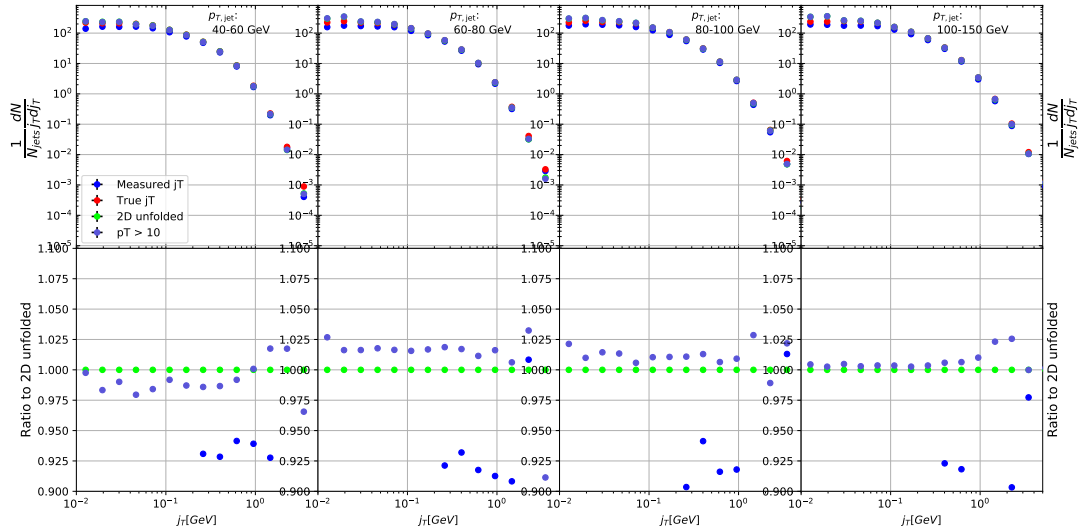


Figure 43: Effect of changing minimum jet p_T used in unfolding from 5 to 10 GeV

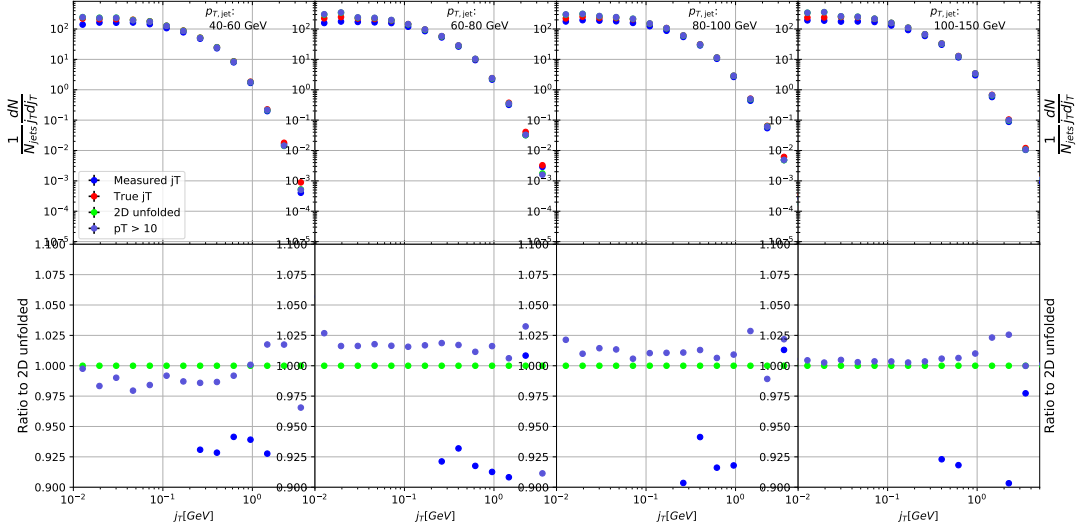


Figure 44: Effect of changing minimum jet p_T used in unfolding from 5 to 10 GeV

1815 5.2.3 Effect of p_T truncation

1816 As an additional check the unfolding is carried out with different $p_{T\text{jet}}$ truncation
 1817 values. By default the full range of $p_{T\text{jet}} > 5\text{GeV}$ is used. As an option the we test
 1818 the unfolding by only using the response matrix for $p_{T\text{jet}} > 10\text{GeV}$. The results of
 1819 this test are shown in Fig. 44

1820 5.3 Tracking

1821 Systematic effects originating from uncertainty in the tracking efficiency are es-
 1822 timated through a PYTHIA simulation, where an artificial inefficiency of 3% is
 1823 introduced. i.e. 3 % of tracks are randomly removed from each event.

1824 5.4 EMCAL

1825 The analysis uses EMCAL clusters only in the reconstruction of jets. Thus the
 1826 only way uncertainty in EMCAL performance can affect the results is through
 1827 modification of jet momentum or axis.

1828 Uncertainty related to the EMCAL energy scale was estimated by scaling clus-
 1829 ter energies up and down by 2 % in a PYTHIA particle level simulation. Similarly
 1830 the jet momentum was scaled by $\pm 2\%$ when determining the jet p_T bin. In the
 1831 analysis EMCAL is used only in jet reconstruction, not for calculating j_T . The
 1832 only ways EMCAL uncertainty can affect the analysis are changes in jet energy

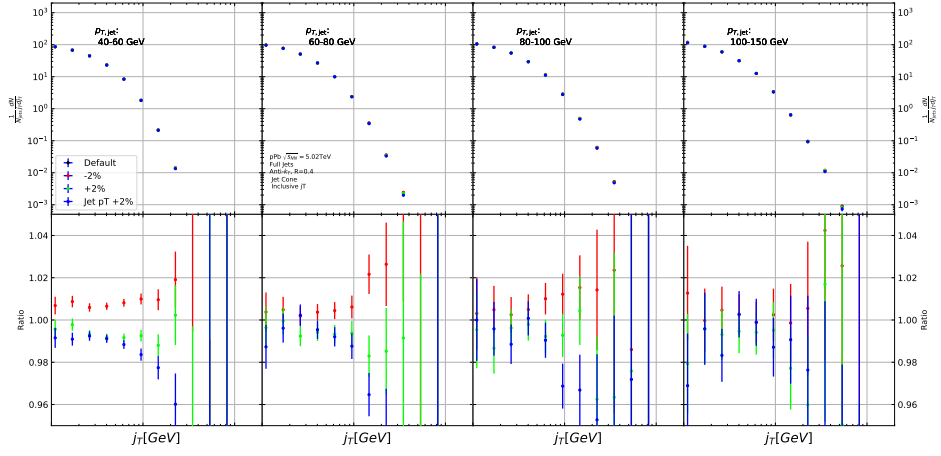


Figure 45: Results from PYTHIA simulations with Cluster energies scale up/down by 2 %. Additionally jet momenta were scaled by 2 % when determining the jet p_T bin.

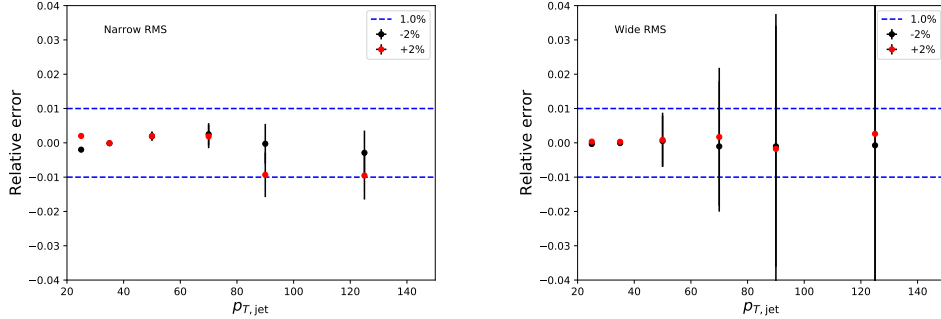


Figure 46: Relative systematic errors resulting from cluster energy uncertainty.

and jet axis. Jet axis shouldn't significantly change, so the main contribution should be changes in jet p_T bin.

The results are shown in Fig. 45. The resulting systematic uncertainties are shown in Fig. 46. The uncertainty is taken to be 1%.

5.5 Summary

There is no tracking and no unfolding uncertainty in the Monte Carlo simulations.

1839 5.6 Comparison between A and C side

1840 In 2013 there were issues with tracking. To rule out effects on j_T distributions a
1841 study was performed comparing j_T distributions between A and C side. 1842 Which
1843 is lead going side and which is proton going No systematic differences were ob-
1844 served. Figure 49 shows the comparison between inclusive distributions between
the different sides, both for minimum bias and EMCAL triggered datasets.

1845 5.7 Subtracted signal

1846 Results in figure 48. Comparison between signals with different backgrounds in
1847 figure 49

1848 5.8 Combining systematics

1849 Resulting systematic errors are shown in table 7. Systematic errors are combined
bin-by-bin in quadrature to get the total systematic errors.

Table 7: Summary of systematic errors

| Systematic | Wide RMS | Narrow RMS |
|------------|----------|------------|
| Background | 5 % | 9 % |
| Unfolding | 8 % | 8 % |
| Tracking | % | % |
| EMCAL | % | % |
| Total | 9 % | 12% |

1850

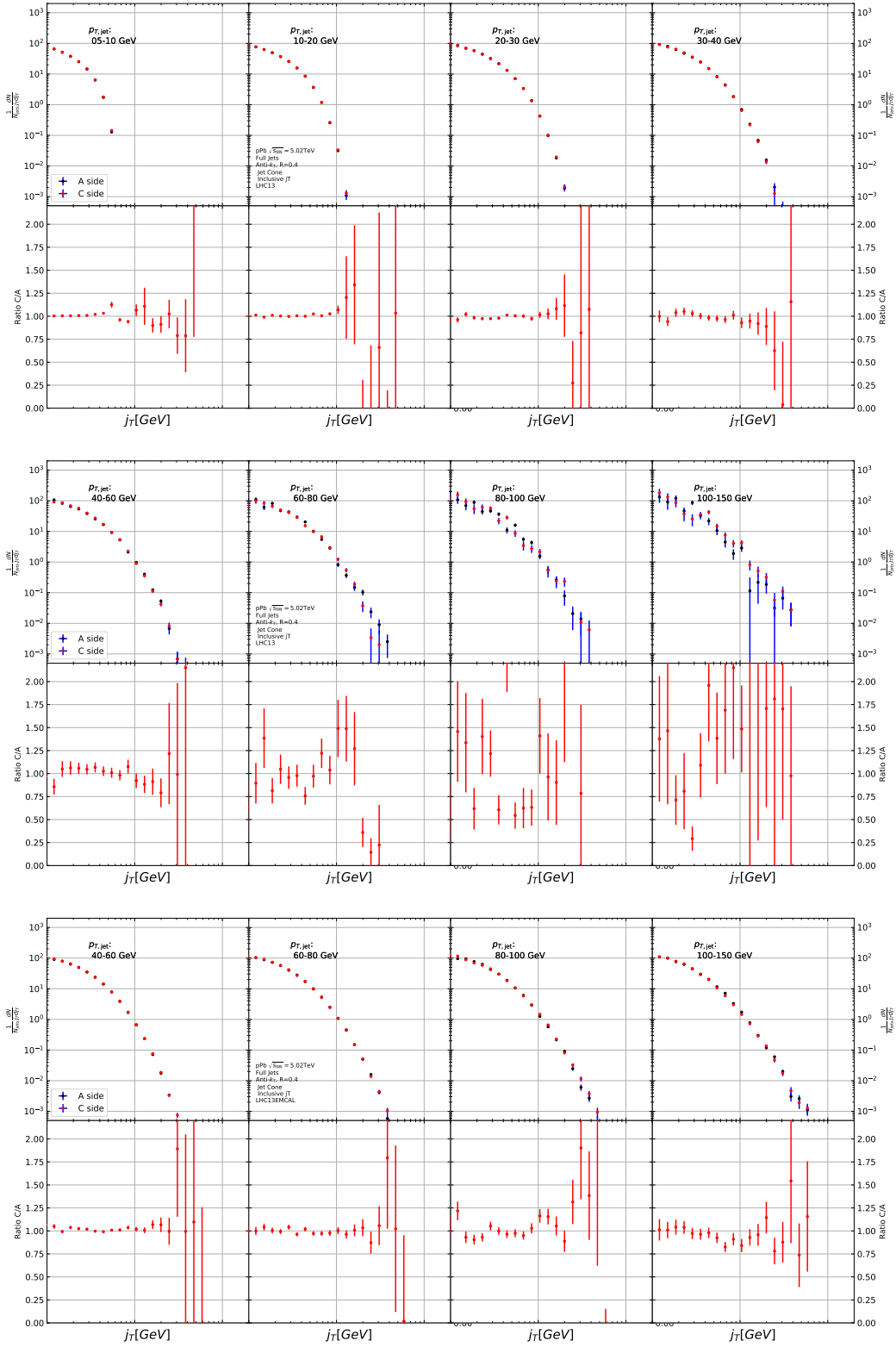


Figure 47: Comparison of inclusive j_{T8} distributions between A and C side for minimum bias and EMCAL triggered data.

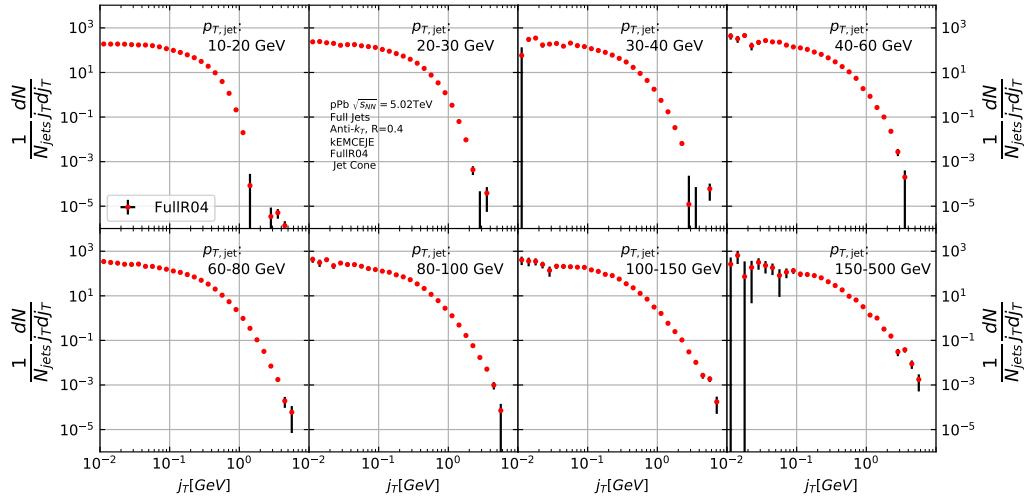


Figure 48: j_T signal with background subtracted

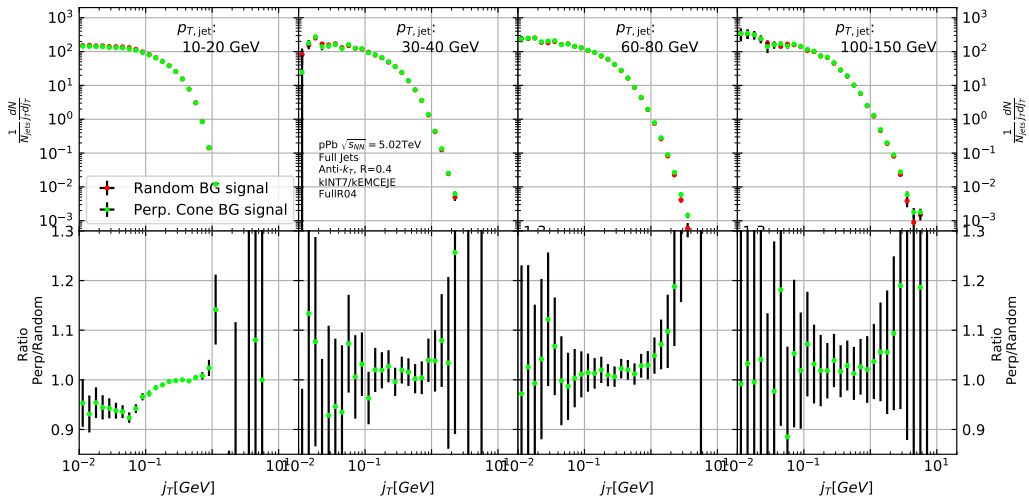


Figure 49: Comparison of the effect of background method on j_T signal.

1851 6 Results

1852 6.1 Fitting

1853 Fits of j_T distributions in different jet p_T bins with $p_T > 40\text{GeV}$ are shown in figure
 1854 50. Additional jet p_T bins are shown in appendix ???. In lowest jet p_T bins the
 1855 jets are mainly combinatorial which makes background subtraction and unfolding
 1856 difficult and thus the signal can't be trusted.

1857 The fits describe the data well. There is some fluctuation of the order of 10 %
 1858 around the fit function. At hight j_T the statistical errors in the signal are large.

1859 6.1.1 RMS values from fitted distributions

1860 RMS results with systematic errors are shown separately in figure 51. Figure 52
 1861 shows RMS values for both components combined. The figure also includes results
 1862 from a PYTHIA simulation.

1863 6.2 High multiplicity

1864 The analysis was repeated taking only events with high multiplicity. Three dif-
 1865 ferent multiplicity cuts were used; 10%, 1% and 0.1%. We used ZDC(TODO)
 1866 as a centrality estimator. As argued in section ?? the zero-degree energy deposit
 1867 should provide a centrality estimator with minimal bias from jets production. Re-
 1868 sulting j_T distributions are shown Fig. 53. As the statistics are limited in the high
 1869 multiplicity runs, it was hard to achieve stable fits to the distributions, thus the
 1870 RMS values are not shown.

1871 From the figure one can observe no systematic modification when tighter mul-
 1872 tiplicity cuts are introduced.

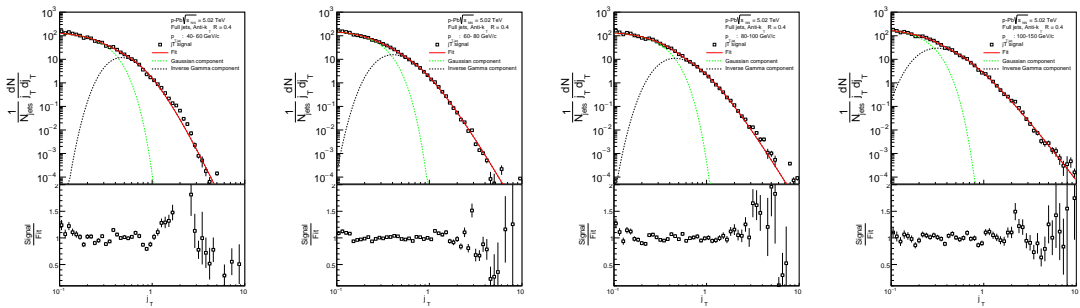


Figure 50: j_T signal fits in different jet p_T bins

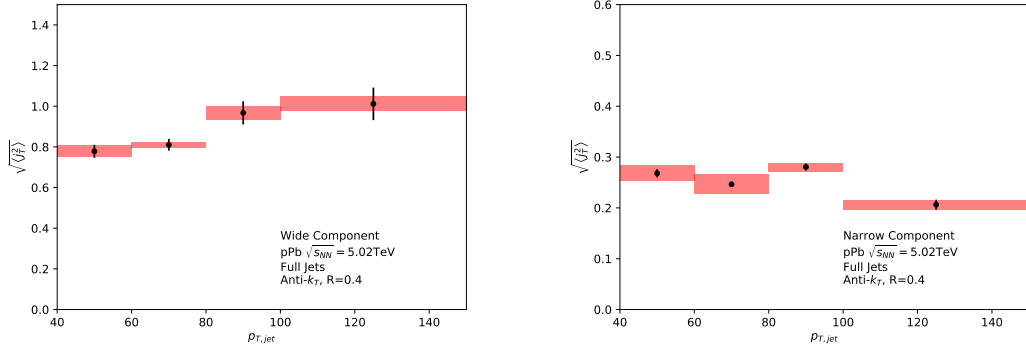


Figure 51: RMS values extracted from the fits for the gaussian (narrow) and inverse gamma (wide) components

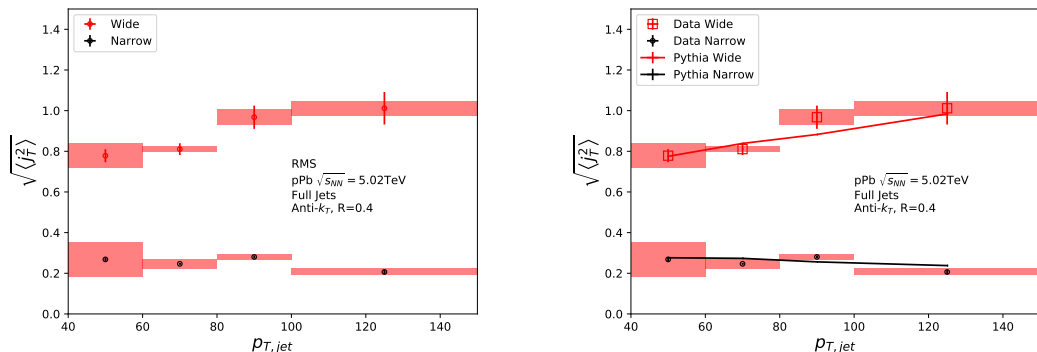


Figure 52: RMS values extracted from the fits for the gaussian (narrow) and inverse gamma (wide) components

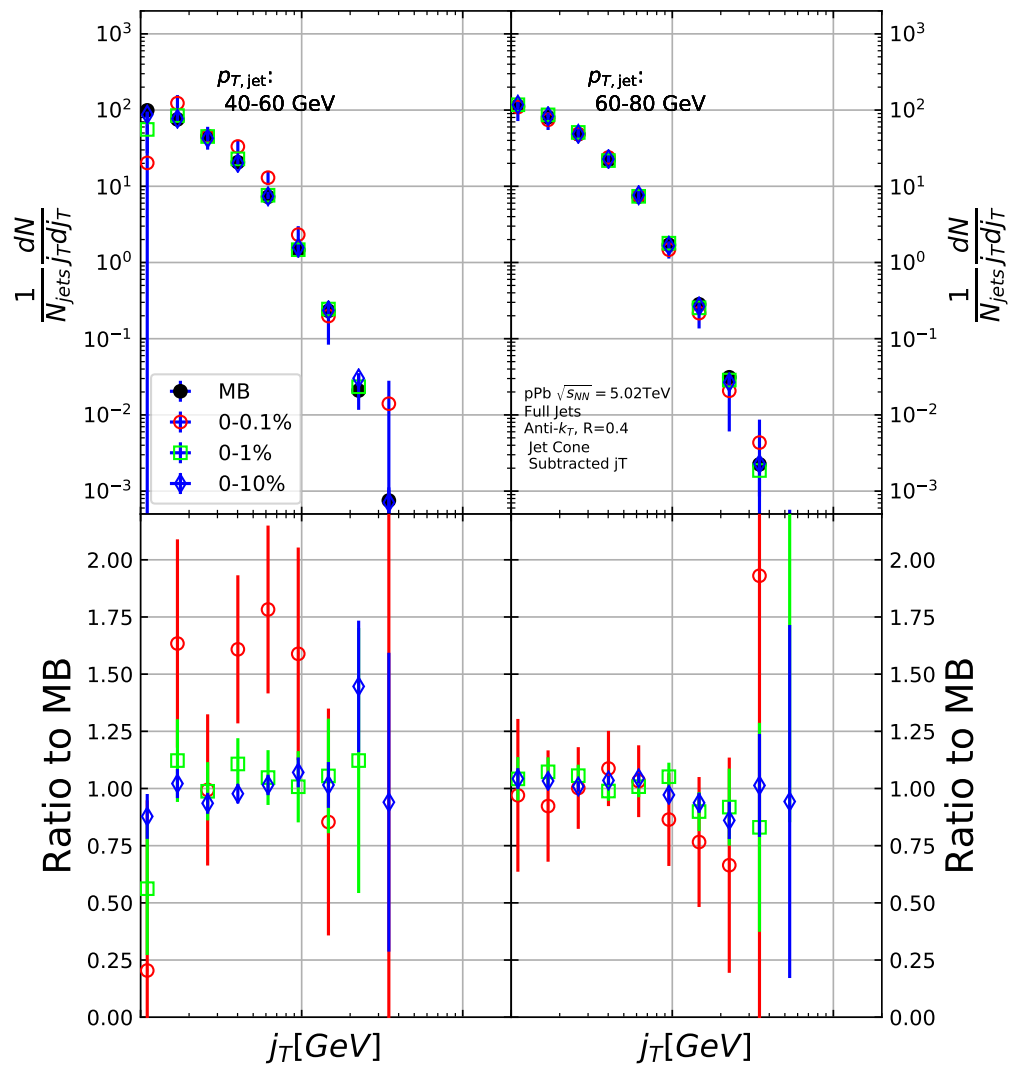


Figure 53: j_T distributions for high multiplicity p–Pb events

¹⁸⁷³ 7 Discussion

¹⁸⁷⁴ [123, 124]

¹⁸⁷⁵ 7.1 Dihadron j_T

¹⁸⁷⁶ The jet fragmentation transverse momentum j_T has been studied previously at
¹⁸⁷⁷ ALICE with dihadron correlations [2]. The study took the leading hadron in
¹⁸⁷⁸ each event and calculated j_T for any near-side tracks with respect to the leading
¹⁸⁷⁹ hadron. Thus there is no kinematical limit to j_T from the jet cone. In the analysis
¹⁸⁸⁰ the background shape is estimated using pairs with large $\Delta\eta$. The normalisation of
¹⁸⁸¹ the background is done when fitting the j_T distribution. The inclusive and signal
¹⁸⁸² distributions from the analysis are shown in Fig. 54. The inclusive distribution is
¹⁸⁸³ fitted with a three component function,

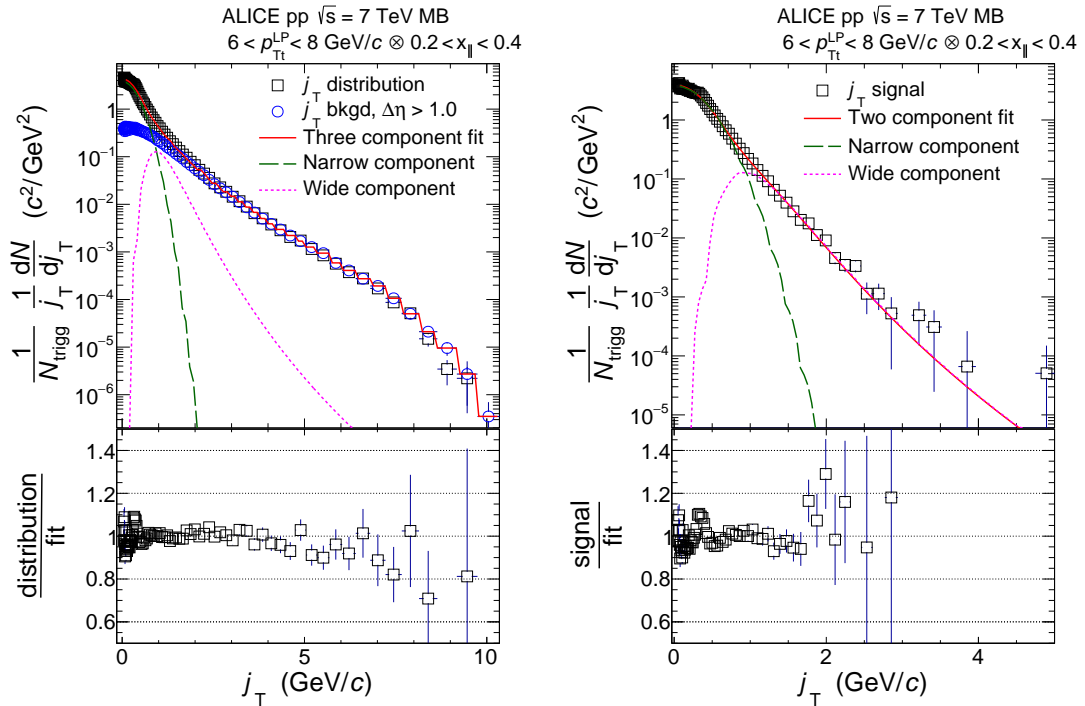


Figure 54: *Left:* Measured j_T distribution including a three-component fit. The three components describe the background (circular symbols), hadronization (long dashed line), and showering (short dashed line). *Right:* The same j_T distribution but with background subtracted.

¹⁸⁸⁴ The analysis was the first to introduce this factorisation of j_T into components.

At $j_T \approx 0.4\text{GeV}$ there is a small bump in the distribution to fit ratio. This was attributed to cases where the trigger particle decayed after hadronisation. As it is difficult to correct for, this bump is included in the systematic errors of the results.

The RMS results from the fitting in both pp and p–Pb collisions are shown in Fig. 55. Qualitatively the results are similar to jet j_T results. The RMS value of the wide component has an increasing trend with respect to p_{Tt}/p_{Tjet} , while the RMS value of the narrow component stays constant. Both components are well described by PYTHIA simulations. As seen in the figures there is no difference between pp and p–Pb results in the dihadron analysis.

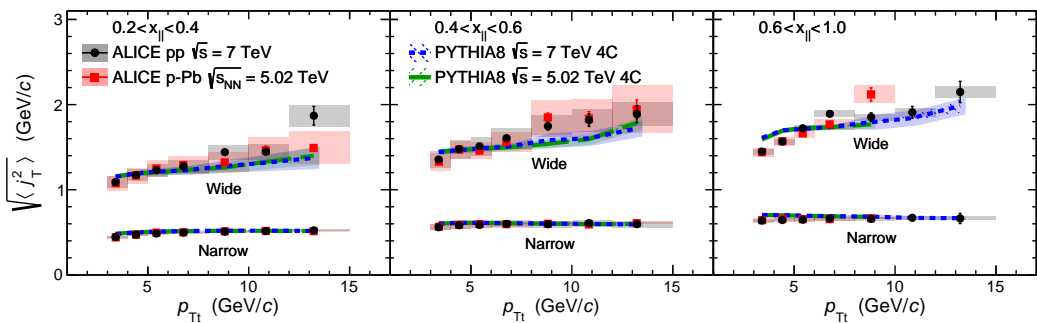


Figure 55: RMS values of the narrow and wide j_T components in the dihadron correlation analysis. Results from pp collisions at $\sqrt{s} = 7\text{ TeV}$ (circular symbols) and from p–Pb collisions at $\sqrt{s_{NN}} = 5.02\text{ TeV}$ (square symbols) are compared to PYTHIA 8 tune 4C simulations at $\sqrt{s} = 7\text{ TeV}$ (short dashed line) and at $\sqrt{s} = 5.02\text{ TeV}$ (long dashed line). Different panels correspond to different x_{\parallel} bins with $0.2 < x_{\parallel} < 0.4$ on the left, $0.4 < x_{\parallel} < 0.6$ in the middle, and $0.6 < x_{\parallel} < 1.0$ on the right. The statistical errors are represented by bars and the systematic errors by boxes. [2]

7.2 Comparing to dihadron and jet j_T results

Comparison to RMS values in dihadron analysis [?] are shown in figure 56 Dihadron results from [?]. For comparison the dihadron trigger p_T bins are converted to jet p_T bins and vice versa. Bin-by-bin comparison is still not possible, but dihadron analysis gives systematically larger RMS values. This could be caused by several kinematical factors. In jet j_T analysis the jet cone limits possible j_T values and thus the width and RMS of the j_T distributions. The effect of this limitation can be studied by changing the cone size as is described in section 7.2.1.

Comparison to j_T results from dihadron analysis [?] is shown in figure ???. Trigger p_T bins used in dihadron analysis are converted to jet p_T bins using ob-

1905 served average jet p_T values in leading track momentum bins. Similarly jet p_T bins
 1906 are converted to $p_{T,\text{trigger}}$ bins using average leading track p_T values in $p_{T,\text{jet}}$ bins.

1907 The trends are similar in dihadron and jet j_T results. Wide component RMS
 1908 values tend to increase with increasing $p_{T,\text{trigger}}/p_{T,\text{jet}}$. Narrow component RMS
 1909 increases slightly in dihadron analysis but not in jet j_T , WHY? (Depends on x_{\parallel}
 1910 bin in dihadron)

1911 In general dihadron j_T gives wider distributions with larger RMS values. In
 1912 jet analysis the cone size limits width and thus the RMS values. The effect of this
 1913 limitation can be studied by changing the cone size as is described in section 7.2.1.

1914 Additionally the leading track is an imperfect estimate of the jet/original par-
 1915 ton. Because the leading track in general is at an angle compared to the jet axis,
 1916 the resulting j_T values are different. In practice the jet axis found by the jet finding
 1917 algorithm tends to minimize the average j_T of jet constituents. Thus the yield
 1918 at high j_T is limited and the RMS values are smaller. The effect of having the
 1919 leading hadron as reference instead of the jet axis is discussed in section 7.2.2

1920 Lastly the results from the dihadron analysis are done in $p_{T,\text{trigger}}$ bins. This
 1921 favours hard jets, i.e. jets where the leading hadron carries a large momentum
 1922 fraction and the jet multiplicity is small. In $p_{T,\text{jet}}$ bins jets are more likely to be
 1923 soft, i.e. small leading momentum fraction and high multiplicity jets.

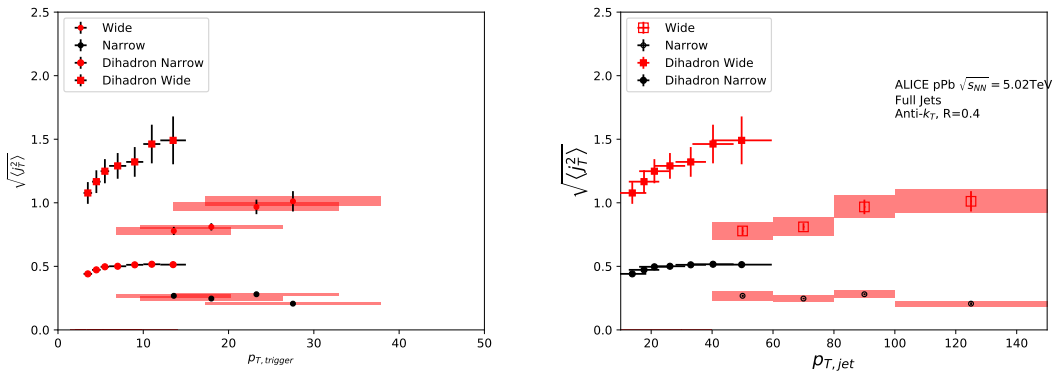


Figure 56: Jet j_T results are compared to results obtained in the dihadron analysis. Dihadron trigger p_T bins are converted to jet p_T bins using observed mean $p_{T,\text{jet}}$ values in $p_{T,\text{trigger}}$ bins. Dihadron results are for $0.2 < x_{\parallel} < 0.4$

1924 7.2.1 Different R parameters

1925 The size of the jet cone gives a limit for j_T . For a track with a fixed momentum p
 1926 this is a hard limit. This is conveniently seen as j_T can be given in terms of cone
 1927 size R and momentum p in the small angle approximation limit as

$$j_T \approx p \cdot R \quad (49)$$

Thus for tracks with $p_{T\text{track}} < p_{T0}$, $j_T < p_{T0} \times R$.

In practice the effect of cone sizes on j_T distribution is studied in a PYTHIA simulation.

Results of the individual distributions and resulting RMS values from this simulation are shown in Fig. 57 and Fig. 58 respectively. Increasing the cone size of jets gives more room for high j_T tracks. This is seen in the individual j_T distributions as increased high j_t production. At low j_T there is no change.

When looking at RMS values from wide component we see an increase/decrease of about 10% when going from $R = 0.4$ to $R = 0.5/R = 0.3$.

The message from narrow component RMS values is less clear. At low jet p_T the behaviour is similar, but at high p_T the order is reversed.

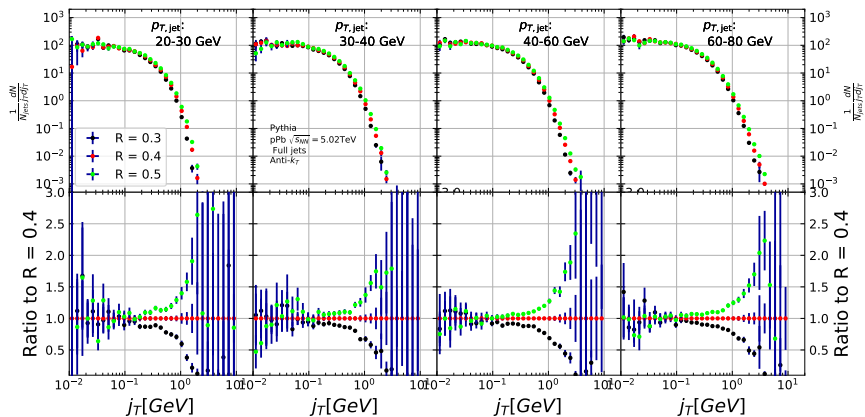


Figure 57: Effect of changing R parameter in jet finding on j_T distributions

1937

1938 7.2.2 Leading tracks versus jet

1939 The leading track is an imperfect estimate of the jet/original parton. Because the
1940 leading track in general is at an angle compared to the jet axis, the resulting j_T
1941 values are different. In practice the jet axis found by the jet finding algorithm
1942 tends to minimize the average j_T of jet constituents. Thus the yield at high j_T is
1943 limited and the RMS values are smaller.

1944 A PYTHIA study was performed where j_T was calculated with respect to the
1945 leading track momentum, instead of the jet axis. The results are shown in Fig. 59.
1946 The resulting j_T distributions are significantly wider than j_T distributions from
1947 the typical method. The effect seems to be larger than the effect seen in comparing
1948 different R values.

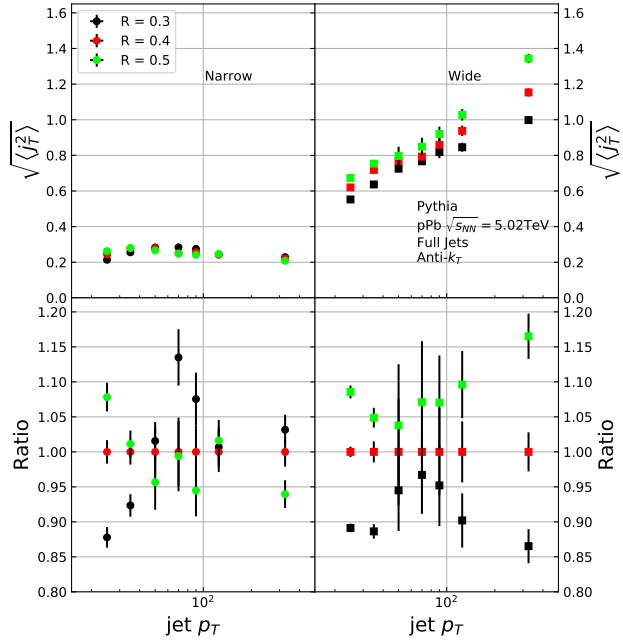


Figure 58: Effect of changing R parameter in jet finding on narrow and wide component RMS values. Wide component RMS values increase with increasing cone size.

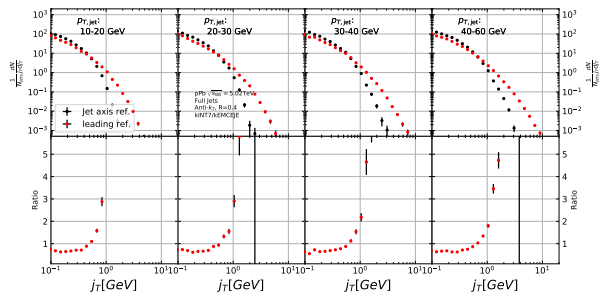


Figure 59: Results of calculating j_T with respect to the jet axis or the leading hadron. The assumption is that because the leading hadron is an imperfect estimate of the jet axis, low j_T tracks should on average be shifted to higher j_T

1949 8 Summary

1950 In this work two distinct j_T components were extracted for narrow and wide contributions using jet reconstruction. RMS values for both components were obtained.
1951 The width of the wide component is found to increase for increasing $p_{T\text{jet}}$. This
1952 is in part explained by the changing kinematical limits when going to higher $p_{T\text{jet}}$
1953 which allows higher $p_{T\text{track}}$. Additionally the larger phase space allows stronger
1954 parton splitting. The results are qualitatively compatible with previous studies
1955 that studied j_T using two-particle correlations.
1956

¹⁹⁵⁷ References

- ¹⁹⁵⁸ [1] ALICE, J. Adam *et al.*, Phys. Rev. **C91**, 064905 (2015), 1412.6828.
- ¹⁹⁵⁹ [2] <https://alice-publications.web.cern.ch/node/3655>, 2018.
- ¹⁹⁶⁰ [3] PHENIX Collaboration, K. Adcox *et al.*, Nucl.Phys. **A757**, 184 (2005), nucl-ex/0410003.
- ¹⁹⁶² [4] STAR Collaboration, J. Adams *et al.*, Nucl.Phys. **A757**, 102 (2005), nucl-ex/0501009.
- ¹⁹⁶⁴ [5] J.-Y. Ollitrault, Phys. Rev. D **46**, 229 (1992).
- ¹⁹⁶⁵ [6] U. Heinz and P. Kolb, Nucl. Phys. **A702**, 269 (2002).
- ¹⁹⁶⁶ [7] E. Shuryak, Prog. Part. Nucl. Phys. **62**, 48 (2009).
- ¹⁹⁶⁷ [8] ATLAS Collaboration, J. Jia, Nucl.Phys.A904-905 **2013**, 421c (2013), 1209.4232.
- ¹⁹⁶⁹ [9] R. A. Lacey *et al.*, (2012), 1207.1886.
- ¹⁹⁷⁰ [10] R. Bjorklund, W. Crandall, B. J. Moyer, and H. York, Phys. Review **77**, 213 (1950).
- ¹⁹⁷² [11] W. Heisenberg, Zeitschrift für Physik **77**, 1 (1932).
- ¹⁹⁷³ [12] M. Gell-Mann, Phys. Rev. **125**, 1067 (1962).
- ¹⁹⁷⁴ [13] M. Gell-Mann, Phys. Lett. **8**, 214 (1964).
- ¹⁹⁷⁵ [14] O. Greenberg, Phys. Rev. Lett. **13**, 598 (1964).
- ¹⁹⁷⁶ [15] Crystal Ball Collaboration, D. Williams *et al.*, Phys.Rev. **D38**, 1365 (1988).
- ¹⁹⁷⁷ [16] W. Krolikowski, Nuovo Cim. **A27**, 194 (1975).
- ¹⁹⁷⁸ [17] D. J. Gross and F. Wilczek, Physical Review Letters **30**, 1343 (1973).
- ¹⁹⁷⁹ [18] H. D. Politzer, Physical Review Letters **30**, 1346 (1973).
- ¹⁹⁸⁰ [19] D. J. Gross and F. Wilczek, Physical Review D **8**, 3633 (1973).
- ¹⁹⁸¹ [20] D. J. Gross and F. Wilczek, Physical Review D **9**, 980 (1974).
- ¹⁹⁸² [21] H. Georgi and H. D. Politzer, Physical Review D **9**, 416 (1974).

- ₁₉₈₃ [22] H. Fritzsch, M. Gell-Mann, and H. Leutwyler, Physics Letters B **47**, 365 (1973).
- ₁₉₈₅ [23] I. Flegel and P. Söding, CERN courier (2004).
- ₁₉₈₆ [24] R. Brandelik *et al.*, Physics Letters B **86**, 243 (1979).
- ₁₉₈₇ [25] J. K. L. MacDonald, Phys. Rev. **43**, 830 (1933).
- ₁₉₈₈ [26] C. Berger *et al.*, Physics Letters B **86**, 418 (1979).
- ₁₉₈₉ [27] J. Collins and M. Perry, Phys. rev. Lett. **34**, 1353 (1975).
- ₁₉₉₀ [28] E. Shuryak, Phys. Reps. **61**, 71 (1980).
- ₁₉₉₁ [29] K. Rajagopal, SLAC Beam Line **31-2**, 9 (2001).
- ₁₉₉₂ [30] P. Kovtun, D. Son, and A. Starinets, Phys.Rev.Lett. **94**, 111601 (2005), hep-th/0405231.
- ₁₉₉₄ [31] R. A. Lacey *et al.*, Phys. Rev. Lett. **98**, 092301 (2007).
- ₁₉₉₅ [32] E. Lofgren, *ACCELERATOR DIVISION ANNUAL REPORTS, 1 JULY 1972 12/31/1974* (, 1975).
- ₁₉₉₇ [33] D. S. Barton, Heavy ion program at bnl: Ags, rhic, in *Proc. 1987 Particle Accelerator Conference, Washington, D.C., March, 1987*, 1987.
- ₁₉₉₉ [34] I. Vitev and M. Gyulassy, Phys.Rev.Lett. **89**, 252301 (2002), hep-ph/0209161.
- ₂₀₀₁ [35] S. Choi and K. S. Lee, Phys. Rev. C **84**, 064905 (2011).
- ₂₀₀₂ [36] A. Kovalenko *et al.*, Status of the nuclotron, in *Proceedings of EPAC Vol. 94*, pp. 161–164, 1994.
- ₂₀₀₄ [37] NA61/SHINE, K. Grebieszkow, PoS **CPOD2013**, 004 (2013).
- ₂₀₀₅ [38] BRAHMS Collaboration, I. Arsene *et al.*, Nucl.Phys. **A757**, 1 (2005), nucl-ex/0410020.
- ₂₀₀₇ [39] B. Back *et al.*, Nucl.Phys. **A757**, 28 (2005), nucl-ex/0410022.
- ₂₀₀₈ [40] S. A. Voloshin, A. M. Poskanzer, and R. Snellings, (2008), 0809.2949.
- ₂₀₀₉ [41] S. A. Voloshin, A. M. Poskanzer, A. Tang, and G. Wang, Phys.Lett. **B659**, 537 (2008), 0708.0800.

- 2011 [42] H. Holopainen, H. Niemi, and K. J. Eskola, Phys.Rev. **C83**, 034901 (2011), 1007.0368.
- 2012
- 2013 [43] ALICE Collaboration, Phys. Rev. C **88**, 044909 (2013).
- 2014 [44] M. L. Miller, K. Reygers, S. J. Sanders, and P. Steinberg, Ann.Rev.Nucl.Part.Sci. **57**, 205 (2007), nucl-ex/0701025.
- 2015
- 2016 [45] R. Glauber, Lectures in theoretical physics, 1959.
- 2017 [46] W. Czyż and L. Maximon, Annals of Physics **52**, 59 (1969).
- 2018 [47] A. Białas, M. Bleszyński, and W. Czyż, Nuclear Physics B **111**, 461 (1976).
- 2019 [48] PHENIX Collaboration, S. Afanasiev *et al.*, Phys.Rev. **C80**, 054907 (2009), 0903.4886.
- 2020
- 2021 [49] J.-Y. Ollitrault, Eur.J.Phys. **29**, 275 (2008), 0708.2433.
- 2022 [50] P. Romatschke, Int.J.Mod.Phys. **E19**, 1 (2010), 0902.3663.
- 2023 [51] L. LD, Izv. Akad. Nauk Ser. Fiz. **17**, 51 (1953).
- 2024 [52] H. Song, S. Bass, and U. W. Heinz, (2013), 1311.0157.
- 2025 [53] H. Niemi, G. Denicol, P. Huovinen, E. Molnar, and D. Rischke, Phys.Rev. **C86**, 014909 (2012), 1203.2452.
- 2026
- 2027 [54] K. A. *et al.* [ALICE Collaboration], Phys. Rev. Lett **106** (2011), 032301.
- 2028 [55] J.-Y. Ollitrault, Phys.Rev. D **48**, 1132 (1993), hep-ph/9303247.
- 2029 [56] P. Danielewicz and G. Odyniec, Physics Letters B **157**, 146 (1985).
- 2030 [57] P. Danielewicz and M. Gyulassy, Physics Letters B **129**, 283 (1983).
- 2031 [58] T. Abbott *et al.*, Phys. Rev. Lett. **70**, 1393 (1993).
- 2032 [59] S. Voloshin and Y. Zhang, Z.Phys. **C70**, 665 (1996), hep-ph/9407282.
- 2033 [60] E877 Collaboration, J. Barrette *et al.*, Phys.Rev.Lett. **73**, 2532 (1994), hep-ex/9405003.
- 2034
- 2035 [61] CMS Collaboration, S. Chatrchyan *et al.*, Phys.Rev.Lett. **109**, 022301 (2012), 1204.1850.
- 2036

- 2037 [62] Y. I. Azimov, Y. L. Dokshitzer, V. A. Khoze, and S. I. Trovan, Zeitschrift
 2038 für Physik C Particles and Fields **27**, 65 (1985).
- 2039 [63] B. Andersson, G. Gustafson, G. Ingelman, and T. Sjöstrand, Physics Reports
 2040 **97**, 31 (1983).
- 2041 [64] A. Buckley *et al.*, Phys. Rept. **504**, 145 (2011), 1101.2599.
- 2042 [65] M. Bahr *et al.*, Eur. Phys. J. **C58**, 639 (2008), 0803.0883.
- 2043 [66] ALICE Collaboration, K. Aamodt *et al.*, Phys.Lett. **B696**, 30 (2011),
 2044 1012.1004.
- 2045 [67] WA98 Collaboration, M. Aggarwal *et al.*, Eur.Phys.J. **C23**, 225 (2002),
 2046 nucl-ex/0108006.
- 2047 [68] D. G. d'Enterria, Phys.Lett. **B596**, 32 (2004), nucl-ex/0403055.
- 2048 [69] PHENIX Collaboration, A. Adare *et al.*, Phys.Rev.Lett. **101**, 232301 (2008),
 2049 0801.4020.
- 2050 [70] STAR Collaboration, J. Adams *et al.*, Phys.Rev.Lett. **91**, 172302 (2003),
 2051 nucl-ex/0305015.
- 2052 [71] A. Dainese, C. Loizides, and G. Paic, Eur.Phys.J. **C38**, 461 (2005), hep-
 2053 ph/0406201.
- 2054 [72] I. Vitev, J.Phys. **G30**, S791 (2004), hep-ph/0403089.
- 2055 [73] C. A. Salgado and U. A. Wiedemann, Phys.Rev. **D68**, 014008 (2003), hep-
 2056 ph/0302184.
- 2057 [74] N. Armesto, A. Dainese, C. A. Salgado, and U. A. Wiedemann, Phys.Rev.
 2058 **D71**, 054027 (2005), hep-ph/0501225.
- 2059 [75] T. Renk, H. Holopainen, R. Paatelainen, and K. J. Eskola, Phys.Rev. **C84**,
 2060 014906 (2011), 1103.5308.
- 2061 [76] CMS Collaboration, S. Chatrchyan *et al.*, Eur.Phys.J. **C72**, 1945 (2012),
 2062 1202.2554.
- 2063 [77] PHENIX Collaboration, S. Afanasiev *et al.*, Phys. Rev. C **80**, 054907 (2009).
- 2064 [78] ALICE Collaboration, K. Aamodt *et al.*, Phys.Rev.Lett. **108**, 092301 (2012),
 2065 1110.0121.

- 2066 [79] R. Baier, Y. L. Dokshitzer, A. H. Mueller, S. Peigne, and D. Schiff, Nucl.
 2067 Phys. **B484**, 265 (1997), hep-ph/9608322.
- 2068 [80] W. H. H. Bethe and, Proc.Roy.Soc.Lond. **A146** (1934).
- 2069 [81] L. D. Landau and I. Pomeranchuk, Dokl. Akad. Nauk Ser. Fiz. **92**, 535
 2070 (1953).
- 2071 [82] A. B. Migdal, Phys. Rev. **103**, 1811 (1956).
- 2072 [83] P. Bosted *et al.*, Quantum-mechanical suppression of bremsstrahlung*, 1993.
- 2073 [84] A. Majumder and M. Van Leeuwen, Prog.Part.Nucl.Phys. **A66**, 41 (2011),
 2074 1002.2206.
- 2075 [85] F. Dominguez, C. Marquet, A. Mueller, B. Wu, and B.-W. Xiao, Nucl.Phys.
 2076 **A811**, 197 (2008), 0803.3234.
- 2077 [86] M. Gyulassy, P. Levai, and I. Vitev, Nucl.Phys. **B571**, 197 (2000), hep-
 2078 ph/9907461.
- 2079 [87] U. A. Wiedemann, Nucl.Phys. **B588**, 303 (2000), hep-ph/0005129.
- 2080 [88] P. B. Arnold, G. D. Moore, and L. G. Yaffe, JHEP **0112**, 009 (2001), hep-
 2081 ph/0111107.
- 2082 [89] X.-N. Wang and X.-f. Guo, Nucl.Phys. **A696**, 788 (2001), hep-ph/0102230.
- 2083 [90] T. Sjostrand, S. Mrenna, and P. Z. Skands, Comput.Phys.Commun. **178**,
 2084 852 (2008), 0710.3820.
- 2085 [91] I. Lokhtin and A. Snigirev, Eur.Phys.J. **C45**, 211 (2006), hep-ph/0506189.
- 2086 [92] N. Armesto, L. Cunqueiro, and C. A. Salgado, Nucl.Phys. **A830**, 271C
 2087 (2009), 0907.4706.
- 2088 [93] K. Zapp, G. Ingelman, J. Rathsman, J. Stachel, and U. A. Wiedemann,
 2089 Eur.Phys.J. **C60**, 617 (2009), 0804.3568.
- 2090 [94] T. Renk, Phys.Rev. **C79**, 054906 (2009), 0901.2818.
- 2091 [95] A. Kurkela and U. A. Wiedemann, Phys. Lett. **B740**, 172 (2015), 1407.0293.
- 2092 [96] J. L. Nagle and W. A. Zajc, Ann. Rev. Nucl. Part. Sci. **68**, 211 (2018),
 2093 1801.03477.
- 2094 [97] E735, T. Alexopoulos *et al.*, Phys. Rev. **D48**, 984 (1993).

- 2095 [98] MiniMax, T. C. Brooks *et al.*, Phys. Rev. **D61**, 032003 (2000), hep-ex/9906026.
- 2097 [99] C. Shen, Z. Qiu, and U. Heinz, Phys. Rev. **C92**, 014901 (2015), 1502.04636.
- 2098 [100] PHENIX, A. Adare *et al.*, Phys. Rev. **C94**, 064901 (2016), 1509.07758.
- 2099 [101] C. A. Salgado and J. P. Wessels, Ann. Rev. Nucl. Part. Sci. **66**, 449 (2016).
- 2100 [102] M. Gyulassy, I. Vitev, X.-N. Wang, and B.-W. Zhang, p. 123 (2003), nucl-th/0302077.
- 2102 [103] E. Norbeck, K. Šafařík, and P. A. Steinberg, Annual Review of Nuclear and Particle Science **64**, 383 (2014), <https://doi.org/10.1146/annurev-nucl-102912-144532>.
- 2105 [104] A. Accardi, F. Arleo, W. K. Brooks, D. D'Enterria, and V. Muccifora, Riv. Nuovo Cim. **32**, 439 (2010), 0907.3534.
- 2107 [105] 2019.
- 2108 [106] T. ALICE Collaboration *et al.*, Journal of Instrumentation **3**, S08002 (2008).
- 2109 [107] The ALICE Collaboration, Report No. CERN-LHCC-2013-020. ALICE-TDR-016, 2013 (unpublished).
- 2111 [108] for the ALICE, C. Zampolli, Particle Identification with the ALICE detector at the LHC, in *Proceedings, PLHC2012: Physics at the LHC 2012 (PLHC2012): Vancouver, BC, Canada, June 4-9, 2012*, 2012, 1209.5637.
- 2114 [109] ALICE, G. Dellacasa *et al.*, (1999).
- 2115 [110] J. Allen *et al.*, Report No. CERN-LHCC-2010-011. ALICE-TDR-14-add-1, 2010 (unpublished).
- 2117 [111] ALICE, K. Aamodt *et al.*, JINST **3**, S08002 (2008).
- 2118 [112] ALICE, B. B. Abelev *et al.*, Int. J. Mod. Phys. **A29**, 1430044 (2014), 1402.4476.
- 2120 [113] ALICE, K. Aamodt *et al.*, JINST **5**, P03003 (2010), 1001.0502.
- 2121 [114] J. Alme *et al.*, Nucl. Instrum. Meth. **A622**, 316 (2010), 1001.1950.
- 2122 [115] ALICE, B. Abelev *et al.*, JHEP **03**, 053 (2012), 1201.2423.
- 2123 [116] ALICE, P. Cortese *et al.*, (2008).

- 2124 [117] ALICE Collaboration, *Technical Design Report on Forward Detectors: FMD, T0 and V0*, 2004.
2125
- 2126 [118] ALICE, B. Abelev *et al.*, Phys. Lett. **B719**, 29 (2013), 1212.2001.
- 2127 [119] M. Cacciari, G. P. Salam, and G. Soyez, Eur. Phys. J. **C72**, 1896 (2012), 1111.6097.
2128
- 2129 [120] M. Cacciari, G. P. Salam, and G. Soyez, JHEP **04**, 063 (2008), 0802.1189.
- 2130 [121] T. Sjöstrand, S. Mrenna, and P. Z. Skands, Comput. Phys. Commun. **178**, 852 (2008), 0710.3820.
2131
- 2132 [122] Roounfold: Root unfolding framework, <http://hepunx.rl.ac.uk/~adye/software/unfold/RooUnfold.html>, 2013.
2133
- 2134 [123] CMS, S. Chatrchyan *et al.*, Phys. Rev. **D90**, 072006 (2014), 1406.0324.
2135
- [124] M. Dasgupta, L. Magnea, and G. P. Salam, JHEP **02**, 055 (2008), 0712.3014.